IN VITRO AND IN SILICO TOOLS FOR STUDYING HETEROTYPIC GAP JUNCTION CHANNEL PROPERTIES

by

Abhijit Mondal

A dissertation submitted to the faculty of
The University of Utah
in partial fulfillment of the requirements for the degree of

Doctor of Philosophy

Department of Bioengineering

The University of Utah

May 2017

The University of Utah Graduate School

STATEMENT OF DISSERTATION APPROVAL

The dissertation of **Abhijit Mondal**

has been approved by the following supervisory committee members:

Alonso P. Moreno	, Chair	**2/14/2017** Date Approved
Frank B. Sachse	, Member	**2/15/2017** Date Approved
Robert Hitchcock	, Member	**2/14/2017** Date Approved
Richard D. Rabbitt	, Member	**2/15/2017** Date Approved
Florian Solzbacher	, Member	**2/14/2017** Date Approved

and by **David D. Grainger** , Chair/Dean of

the Department/College/School of **Bioengineering**

and by David B. Kieda, Dean of The Graduate School.

ABSTRACT

This body of work aimed at creating new tools for heterotypic gap junction channels for better understanding their role and permeability mechanisms in healthy and diseased tissue. Gap junctions play a vital role in the tissue of many organ systems of the body. They are responsible for maintaining conduction in the heart and their transformations and damage are associated with cardiac failure events. A lot is still not known about their formation and function at the junctional level. Scientists studying gap junction are presented with many experimental challenges and rely on tools and protocols that are cumbersome to execute and have high failing rate. While the amino acid sequence and topology across the cell membrane of all connexins is known, the molecular structure and charge density distribution is only known for connexin 26, out of the 21 connexin isoforms in the human body. This makes it almost impossible to utilize existing molecular dynamic models for studying the form and function of other connexins through computational means. Scientists have to rely mostly on *in vitro* and *in vivo* experiments in studying gap junctions and making predictions on mechanism, role and function in physiological and pathophysiological conditions.

We have developed and tested new *in vitro* and *in silico* tools for studying gap junctions at the tissue and single channel level, respectively. The novel *in vitro* tool was a microelectrode array on a thin flexible porous substrate called PerFlexMEA. The PerFlexMEA was developed using microfabrication processes. We investigated its capability of maintaining a bilayered tissue architecture of two different cell types while

allowing controlled lateral coupling between the two cell layers through substrate micropores, mimicking cardiac tissue distribution of myocytes and fibroblasts. Dye diffusion and confocal imaging was utilized in demonstrating this capability. Furthermore, we conducted electrophysiological experiments and demonstrated a drop in conduction velocity of cardiomyocytes on controlled lateral coupling with nonmyocytes.

The *in silico* tool developed was a simplified Brownian dynamics model of a gap junction pore. The model was developed to investigate the significance of gap junction pore shape in creating asymmetric fluxes of large molecules in heterotypic gap junction pores that have been widely recorded from *in vitro* experiments. We demonstrated the ability of an inactive heterotypic pore in generating flux asymmetry, revealed the mechanism involved and the factors requisite for such asymmetry to occur. Flux asymmetry recorded in simulations with our hypothesized pore shape matched the corresponding *in vitro* data. We further investigated and established the roles of different pore sections of the heterotypic pore, particle size and charge on flux asymmetry. The original hypothesized pore shape was further optimized to maximize flux asymmetry.

We believe this work contributes toward expanding the field of gap junction within the available experimental and computational limits. The PerFlexMEA has the potential to be a potent tool for electrophysiological studies in fibrotic and arrhythmic cardiac tissues. Our *in silico* studies have revealed a new physiological mechanism that needs to be further investigated *in vitro*.

This thesis is dedicated to

my grandmother Smt. Biva Roy (1935-2015)

and my uncle Shri. Achinto Kumar Mondal (1942-2011)

TABLE OF CONTENTS

LIST OF FIGURES

Figures

LIST OF TABLES

Tables

ACKNOWLEDGEMENTS

I would like to express my sincere and deepest gratitude to my advisor Dr. Alonso P. Moreno for his guidance, insights, support and patience throughout my research, training and time in graduate school. I thank Dr. Frank B. Sachse for his advice, support and role in my training and completing my research. I also thank my other committee members Drs. Hitchcock, Solzbacher and Rabbit for their inputs and comments during my research. I thank Brian Baker and the Nanofab staff for all their help and guidance at the Nanofab facility. Thanks to faculty, staff and students at Nora Eccles Harrison Cardiovascular Research and Training Institute for their assistance and support in conducting my research. I thank my sister Dr. Kalyani Mondal and brother-in-law Dr. Arindam Mandal for their advice and support. I thank my friends Amruta Narumanchi, Mukund Raj, Drs. Abhigya Mookherjee, Vimal Swarup, Raheel Samuel, Amirali Abdullah, Sagar Godambe, Vivek Garg and Priyanka Garg at the U for their friendship and making my stay here fun-filled and pleasant. Finally I would like to thank my parents, family and friends settled around the world for their love, encouragement and moral support throughout my training at graduate school.

CHAPTER 1

INTRODUCTION

1.1 Introduction

Heart disease is the leading cause of deaths in the United States accounting for 1 in every 4 deaths [1]. A majority of these are due to failure of the conduction system in the heart. Gap junctions play a vital role in maintaining this conduction, while also enabling the transport of other metabolic molecules. Cardiac disease results in the transformation in architecture, form and functional properties of gap junctions. Hence, it is important to study gap junctions, their different forms and properties to better understand the mechanisms involved during such conditions. In this chapter, we discuss gap junctions, their role in heart diseases, the tools available for studying them and some of their key limitations with focus on heterotypic gap junctions.

1.2 Gap junctions and structural issues

Gap junctions are specialized membrane structures formed by arrays of channels formed between the membranes of two adjacent cells placed 2-4 nm apart [2]. They act as conduits and connect the cytoplasm of coupled cells allowing exchange of ions and other biological molecules up to ~1000 Da [3]–[16]. Each cell membrane contributes a half pore structure to its end of the channel, called a hemichannel (or connexon) arranged co-axially

in series to form a complete full gap junction channel. Each hemichannel is made of six subunits called connexins (Cx) and arranged to form a cylinder-like pore. Hemichannels made of the same Cx isoforms are called homomeric and those made of multiple Cx isoforms are called heteromeric. Gap junction channels formed of homomeric hemichannels are called homotypic channels and those formed out of different homomeric hemichannels are known as heterotypic channels. Twenty-one different connexin isoforms have been identified in humans [17]. Channels composed of particular hemichannel isoforms exhibit unique properties in unitary conductance, permeability, selectivity, voltage sensitivities and reaction to modulation agents. These properties are mainly associated with the Cx molecular structure. In general, Cx contains 4 transmembrane domains (M1 to M4), 2 extracellular loops (E1 and E2), 1 cytoplasmic loop (CL) and a carboxyl-tail (CT) and amino-tail (NT). The transmembrane domains (M1 to M4) constitute the walls of the pore. E1 and E2 help in cell-cell recognition and the docking process [18]. CL and CT are most susceptible to posttranslational modifications (like phosphorylation). Imaging techniques like electron microscopy [19]–[21], x-ray diffraction [22]–[24], nuclear magnetic resonance spectroscopy [25]–[27] and atomic force microscopy [28], [29] have been utilized for mapping the molecular structure of gap junctions formed out of different Cx isoforms, but the actual molecular structure and charge distribution of complete gap junction pores is only available for Cx26 [24], [30]. Hence, scientist have relied on *in vitro* studies and found distinct properties of unitary conductance, permeability and selectivity, voltage sensitivities and reaction to modulation agents. The biophysical mechanisms of many of these properties have not been clearly established yet. Heterotypic pores present a further challenge, as they are harder to detect. Cx combinations

are selective in formation of heterotypic channels [31], [32]. Heterotypic channel properties were extensively studied *in vitro* [33]–[44] where some heterotypic channels showed different permeability properties from their original hemichannels which could pose significant physiological consequences through change of permeability properties in healthy and diseased tissues. In the past decade, heterotypic junctions have been associated with diseased tissues *in vivo* [45]–[48] and there is a greater need to study these channel types.

1.3 Cardiomyopathy and heterotypic Cx43-Cx45 gap junctions

The heart is known to express Cx40, Cx43, Cx45 and Cx30.2 with Cx43 predominant in ventricular tissue [7], [49], where they serve as conduits for ion-flow in myocytes for ventricular conduction. Myocardial tissue constitutes myocytes and nonmyocytes, with fibroblasts dominating in number among nonmyocytes. While myocytes occupy the majority of the volume, fibroblasts are 20-40 times smaller in size and vary in number by up to 70% more than myocytes in some cases [50]. Fibroblasts are of mesenchymal origin and flat-spindle shaped in *in vitro* cultures. They are found everywhere in the body, but vary in morphology depending on organ tissue type. They produce a variety of extracellular matrix proteins – primarily collagen type I and III, forming the connective tissue that is vital to the structural integrity of the heart. While being non-excitable, fibroblasts possess a number of ion channels, some of which are voltage dependent [51]–[53]. In healthy heart tissue, they are supposed to couple to each other through homo- and heterotypic gap junctions, primarily made of Cx43 and Cx45 [54]. While myocytes and fibroblasts are part of healthy cardiac tissue, myofibroblasts appear

only following cardiac injury [55]. Myofibroblasts are larger than fibroblasts with ruffled membranes and a very active endoplasmic reticulum. Myofibroblasts possess morphological and biochemical characteristics that are between smooth muscle cells and fibroblasts [56]. Like fibroblasts, they too are not excitable and can intercalate themselves between myocytes and produce conduction barriers. Myofibroblasts contain proteins for Cx43 and Cx45 [57], and have been reported to couple with neonatal myocytes *in vitro*. Most heart failure events are followed by some sort of myocardial remodeling or fibrosis where the body tries to heal the damaged regions by excessive production of fibroblasts/myofibroblasts and extracellular matrix (ECM) [58], [59]. There is also a significant change in the expression of Cx types, where Cx43 expression decreases and Cx45 expression increases [60]. Such rise in multiple Cx expressions increases the probability of heterotypic junction formation. Electrotonic coupling of myocytes and nonmyocytes has been demonstrated in *in vitro* cell cultures [54], [61], [62]. While such coupling was demonstrated *in vivo* [63], [64], it was the recent studies by Quinn et al. [65] that confirmed such electrotonic coupling to exist *in vivo*, putting a new argument to the debate and discussion [66]–[72] on the need for improved studies of heterotypic coupling from junctional to tissue level.

1.4 Currents tools for studying heterotypic gap junction properties

Current approaches for studying heterotypic gap junction properties and their effect can be broadly classified into *in vitro* and *in silico* tools. Each of these can be further characterized based on scale of the model ranging from single channel, cellular to tissue level.

1.4.1 *In vitro* tools

1.4.1.1 Permeability of dye and endogenous molecules

A simple tool for permeability studies is through dye transfer. The basic idea is to load one of the cells (donor) in coupled cells (pair or multiple cells) with a fluorescent dye and record dye transfer into the adjacent cells (receiver). The successful transfer of dye confirms the formation of gap junction, though no dye transfer might just indicate impermeability to the selected dye. Until now, no dye has been shown to be Cx specific, though varying permeability properties have been reported. Based on these predictions on pore sizes, charge preference and molecular selectivity can be made. Dyes can be loaded through different approaches:

(1) Microinjection [73]–[75]: A membrane impermeable fluorescent tracer is injected into the donor cell using a micropipette. Diffusion of the tracer in the receiver cells is noted.

(2) Scrape loading [76], [77]: Monolayers of receiver cells are scraped along a line. The scraped line is loaded with a fluorescent dye that is gap junction permeable and membrane impermeable. The diffusion of the gap junction permeable dye into the cell monolayer indicates gap junction communication.

(3) Gap-FRAP (Fluorescence Recovery after Photobleaching) [78]–[80]: It is a scaled up FRAP method, where cell monolayer is loaded with a uniform concentration of the fluorescent tracer. A cell containing the tracer is selected and photobleached. Functional gap junctions are detected if fluorescence begins to appear in the bleached cells.

(4) Preloading or parachute assay [81], [82]: This involves staining the receiver cells with a lipophilic dye and loading the donor cells with a gap junction permeable tracer. Donor

cells are dropped into the cultured monolayer of receiver cells. Presence of gap junction permeable tracer in the receiver cells indicates functional gap junctions. Since only the receiver cells have lipophilic dye, they can be easily distinguished from the donor cells.

(5) LAMP (Local Activation of Molecular Fluorescent Probe) [83], [84]: The cells are loaded with a caged and cell permeable photo-activatable fluorophore. A labeled donor cell is locally uncaged through UV exposure, which activates the fluorophore. The transfer of this photo-activated fluorophore to adjacent cells confirms gap junction coupling.

(6) Radio-labeled nucleotides [85]–[87]: This method enables studying the transfer of endogenous molecules through fluorescent detection of indirect metabolic effect. The donor cells are cultured with the radiolabeled precursor like uridine, and then co-cultured with the unlabeled receiver cells. If the radiolabeled nucleotides synthesized within the donor cells are transferred to the receiver cell, its cytoplasm gets autoradiographically labeled through ribonucleic acid (RNA) incorporation.

(7) Intercellular calcium waves [88], [89]: This is usually studied at multiple-cell level and gives a measure of the propagation of increased calcium levels from cell to cell through gap junctions known as the intercellular calcium wave (ICW). Fluorescent calcium indicators like fura-2 [90] and fluo-3 [91] are used. ICW is considered an indirect measure of the gap junction efficacy and permeability of calcium ions and IP_3 molecules.

1.4.1.2 Conductance measurements at cellular junctions

Junctional conductance measurements reflect on the permeability of small ions of sodium (Na^+), potassium (K^+), chloride (Cl^-), involved in the flow of charge in conductive tissues. Double whole cell voltage clamp is the most widely used technique for conductance measurements [92]. In this method, two pipettes with microelectrodes impale into the two coupled cells across the gap junction plaque. The cells are voltage clamped and the transjunctional voltage/current can be controlled using the microelectrodes. Dyes can also be diffused through either of the pipettes while simultaneously controlling the transjunctional current. This technique enables recording permeability as well as unitary conductance of the junction.

1.4.1.3 Conduction measurement in tissues using extracellular microelectrodes

These measurements have relevance for determining the efficacies of electrical signal propagation at the tissue level. Such studies involve the use of microelectrodes and multielectrode arrays (MEA) [54], [61], [93]–[97] that record extracellular potentials at different points in the culture or tissue. Since the main conduit of conduction in cardiac and neuronal tissues is gap junction, the effect of different parameters on their function can be indirectly studied.

Any *in vitro* technique involving microelectrode pipettes is invasive and ends up breaking down the cells during the experiment. Such experiments have to be executed within a short duration (few minutes) of time, hence having a high failing rate. Furthermore, invasive electrodes might change the physiological conditions in the cell.

Dye transfer experiments with microinjection, scrap loading, parachute assays and radio nucleotide transfer provide low temporal resolution and are mostly useful for studying the magnitude of coupling. Gap-FRAP, LAMP, ICW and dual whole cell voltage clamp experiments provide better temporal resolution, allowing fluxes of large molecules amongst different junction-types to be studied. Dye diffusion under dual whole cell voltage clamp provides the highest temporal and voltage sensitivity. Since it enables measurement of unitary conductance, flux per channel can also be calculated. This is by far the most accurate method available for quantifying permeability among different gap junction types. It is also the most difficult experiment to set up and has a high failing rate. Among techniques for tissue level studies, MEAs provide a simpler noninvasive approach for studying conduction properties in chronic studies with neonatal ventricular myocytes, heart musculature, neuronal cultures and brain tissue.

1.4.2 *In silico* tools

Computational modeling provides an alternative approach for studying gap junctions. Models were developed at the tissue and molecular level, though they depend on known physiological parameters from experimental studies.

(1) Tissue level conduction models [98]–[102]: Most of these models study cardiac tissue conduction. The cell and gap junctional parameters used in these models are from tissue imaging and existing experimental data of junctional conductance of involved Cxs.

(2) Single channel molecular modeling [103], [104]: Molecular and Brownian dynamics models have been implemented for studying permeability or selectivity properties of Cx26 hemichannels and junctions. These models require molecular structural details

and pore charge distribution, which are currently only available for Cx26 [24], [30].

1.5 Introduction to this dissertation

In this body of work, we have addressed some of the limitations in methods and approaches for studying heterotypic gap junction properties at the tissue and single channel level. Our studies presented using the developed tools focus on heterotypic channels formed by Cx43 and Cx45. The *in vitro* tool reflects the physiological and pathological situation involving Cx43-Cx45 heterotypic gap junctions in cardiac tissue and the *in silico* tool facilitates the understanding of permeability properties across those heterotypic junctions. We have broadly utilized current techniques of dye diffusion through microinjection, parachute assays and double whole cell voltage clamping for validating or shaping the new tools we present in this body of work.

In Chapter 2, we present a new *in vitro* device to address limitations of existing fibrotic tissue models where we are able create and record from myocyte-nonmyocyte co-cultures with controlled heterocellular communication. We developed this device utilizing microfabrication technology [105] at the state of the art Nanofab facility. Chapter 3 presents a simplified Brownian dynamic model for gap junction pores. We took a nonconventional approach to investigate the role of pore shape in creating asymmetric fluxes in heterotypic gap junction channels. The entire model was developed using MATLAB and was run on computational facilities at CVRTI and College of Engineering. Chapter 4 presents results from computational studies using our model focused on establishing the roles of pore shape, particle size and charge on generating flux asymmetry in heterotypic gap junction pores. Finally in Chapter 5, we present our conclusions and

future prospects and ideas.

1.6 References

[1] "Centers for Disease Control and Prevention, www.cdc.gov." [Online]. Available: www.cdc.gov. [Accessed: 01-Oct-2014].

[2] R. Bruzzone, T. W. White, and D. L. Paul, "Connections with connexins: the molecular basis of direct intercellular signaling," in *EJB Reviews 1996*, Berlin, Heidelberg: Springer Berlin Heidelberg, 1996, pp. 135–161.

[3] W. A. Ayad, D. Locke, I. V. Koreen, and A. L. Harris, "Heteromeric, but not homomeric, connexin channels are selectively permeable to inositol phosphates," *J. Biol. Chem.*, vol. 281, no. 24, pp. 16727–16739, 2006.

[4] P. Bedner, H. Niessen, B. Odermatt, K. Willecke, and H. Harz, "A method to determine the relative cAMP permeability of connexin channels," *Exp. Cell Res.*, vol. 291, no. 1, pp. 25–35, 2003.

[5] P. Bedner, H. Niessen, B. Odermatt, M. Kretz, K. Willecke, and H. Harz, "Selective permeability of different connexin channels to the second messenger cyclic AMP," *J. Biol. Chem.*, vol. 281, no. 10, pp. 6673–6681, 2006.

[6] E. C. Beyer *et al.*, "Heteromeric mixing of connexins: compatibility of partners and functional consequences," *Cell Commun. Adhes.*, vol. 8, no. FEBRUARY, pp. 199–204, 2001.

[7] F. F. Bukauskas *et al.*, "Properties of mouse connexin 30.2 and human connexin 31.9 hemichannels: implications for atrioventricular conduction in the heart," *Proc. Natl. Acad. Sci. U. S. A.*, vol. 103, no. 25, pp. 9726–9731, 2006.

[8] G. S. Goldberg, P. D. Lampe, and B. J. Nicholson, "Selective transfer of endogenous metabolites through gap junctions composed of different connexins.," *Nat. Cell Biol.*, vol. 1, no. 7, pp. 457–459, 1999.

[9] A. L. Harris, "Connexin channel permeability to cytoplasmic molecules," *Prog. Biophys. Mol. Biol.*, vol. 94, no. 1–2, pp. 120–143, 2007.

[10] D. Locke *et al.*, "Altered permeability and modulatory character of connexin channels during mammary gland development," *Exp. Cell Res.*, vol. 298, no. 2, pp. 643–660, 2004.

[11] A. D. Martinez, V. Hayrapetyan, A. P. Moreno, and E. C. Beyer, "Connexin43 and Connexin45 Form Heteromeric Gap Junction Channels in Which Individual Components Determine Permeability and Regulation," *Circulation*, vol. 90, no. 10,

pp. 1100–1107, 2002.

[12] H. Niessen, H. Harz, P. Bedner, K. Krämer, and K. Willecke, “Selective permeability of different connexin channels to the second messenger inositol 1,4,5-trisphosphate.,” *J. Cell Sci.*, vol. 113 (Pt 8, no. 8, pp. 1365–72, Apr. 2000.

[13] V. Valiunas *et al.*, “Connexin-specific cell-to-cell transfer of short interfering RNA by gap junctions,” *J. Physiol.*, vol. 568, no. 2, pp. 459–468, 2005.

[14] R. D. Veenstra, H. Z. Wang, E. C. Beyer, and P. R. Brink, “Selective dye and ionic permeability of gap junction channels formed by connexin45,” *Circ. Res.*, vol. 75, no. 3, pp. 483–90, 1994.

[15] R. D. Veenstra, “Determining ionic permeabilities of gap junction channels,” in *Methods Mol Biol*, vol. 154, Springer, 2001, pp. 293–311.

[16] V. Verselis, R. White, D. Spray, and M. Bennett, “Gap junctional conductance and permeability are linearly related,” *Science (80-.).*, vol. 234, no. 4775, 1986.

[17] S. Goran and K. Willecke, “Gap junctions and the connexin protein family,” *Cardiovasc. Res.*, vol. 62, no. 2, pp. 228–232, 2004.

[18] V. Krutovskikh and H. Yamasaki, “Connexin gene mutations in human genetic diseases.,” *Mutat. Res.*, vol. 462, no. 2–3, pp. 197–207, 2000.

[19] V. M. Unger, N. M. Kumar, N. B. Gilula, and M. Yeager, “Three-dimensional structure of a recombinant gap junction membrane channel,” *Science*, vol. 283, no. 5405, pp. 1176–1180, 1999.

[20] V. M. Unger, N. M. Kumar, N. B. Gilula, and M. Yeager, “Projection structure of a gap junction membrane channel at 7 A resolution.,” *Nat. Struct. Biol.*, vol. 4, no. 1, pp. 39–43, Jan. 1997.

[21] S. J. Fleishman, V. M. Unger, M. Yeager, and N. Ben-Tal, “A Cα Model for the Transmembrane α Helices of Gap Junction Intercellular Channels,” *Mol. Cell*, vol. 15, no. 6, pp. 879–888, 2004.

[22] P. N. Unwin and P. D. Ennis, “Calcium-mediated changes in gap junction structure: evidence from the low angle X-ray pattern.,” *J. Cell Biol.*, vol. 97, no. 5, 1983.

[23] T. T. Tibbitts, D. L. Caspar, W. C. Phillips, and D. A. Goodenough, “Diffraction diagnosis of protein folding in gap junction connexons.,” *Biophys. J.*, vol. 57, no. 5, pp. 1025–36, May 1990.

[24] S. Maeda *et al.*, “Structure of the connexin 26 gap junction channel at 3.5 A resolution,” *Nature*, vol. 458, no. 7238, pp. 597–602, Apr. 2009.

[25] P. L. Sorgen, H. S. Duffy, P. Sahoo, W. Coombs, M. Delmar, and D. C. Spray,

"Structural changes in the carboxyl terminus of the gap junction protein connexin43 indicates signaling between binding domains for c-Src and zonula occludens-1," *J. Biol. Chem.*, vol. 279, no. 52, pp. 54695–54701, Dec. 2004.

[26] P. L. Sorgen, H. S. Duffy, D. C. Spray, and M. Delmar, "pH-dependent dimerization of the carboxyl terminal domain of Cx43.," *Biophys. J.*, vol. 87, no. 1, pp. 574–581, 2004.

[27] H. S. Duffy *et al.*, "pH-dependent intramolecular binding and structure involving Cx43 cytoplasmic domains," *J. Biol. Chem.*, vol. 277, no. 39, pp. 36706–36714, Sep. 2002.

[28] D. J. Müller, G. M. Hand, A. Engel, and G. E. Sosinsky, "Conformational changes in surface structures of isolated connexin 26 gap junctions.," *EMBO J.*, vol. 21, no. 14, pp. 3598–3607, Jul. 2002.

[29] F. Liu, F. T. Arce, S. Ramachandran, and R. Lal, "Nanomechanics of hemichannel conformations: Connexin flexibility underlying channel opening and closing," *J. Biol. Chem.*, vol. 281, no. 32, pp. 23207–23217, Aug. 2006.

[30] B. C. Bennett *et al.*, "An electrostatic mechanism for Ca(2+)-mediated regulation of gap junction channels," *Nat Commun*, vol. 7, p. 8770, 2016.

[31] E. C. Beyer, "Are these connexins compatible and does it matter?," *Channels*, vol. 9, no. 2, pp. 1–2, 2015.

[32] D. Bai and A. H. Wang, "Extracellular domains play different roles in gap junction formation and docking compatibility.," *Biochem. J.*, vol. 458, pp. 1–10, 2014.

[33] G. T. Cottrell and J. M. Burt, "Heterotypic gap junction channel formation between heteromeric and homomeric Cx40 and Cx43 connexons.," *Am. J. Physiol. Cell Physiol.*, vol. 281, no. 5, pp. C1559-67, 2001.

[34] D. S. He, J. X. Jiang, S. M. Taffet, and J. M. Burt, "Formation of heteromeric gap junction channels by connexins 40 and 43 in vascular smooth muscle cells.," *Proc. Natl. Acad. Sci. U. S. A.*, vol. 96, no. 11, pp. 6495–6500, 1999.

[35] A. Jassim, H. Aoyama, W. G. Ye, H. Chen, and D. Bai, "Engineered Cx40 variants increased docking and function of heterotypic Cx40/Cx43 gap junction channels," *J. Mol. Cell. Cardiol.*, vol. 90, pp. 11–20, 2016.

[36] L. M. Magnotti, D. A. Goodenough, and D. L. Paul, "Functional heterotypic interactions between astrocyte and oligodendrocyte connexins," *Glia*, vol. 59, no. 1, pp. 26–34, 2011.

[37] J. L. Orthmann-Murphy, M. Freidin, E. Fischer, S. S. Scherer, and C. K. Abrams, "Two Distinct Heterotypic Channels Mediate Gap Junction Coupling between Astrocyte and Oligodendrocyte Connexins," *J. Neurosci.*, vol. 27, no. 51, pp.

13949–13957, 2007.

[38] M. Rackauskas, M. M. Kreuzberg, M. Pranevicius, K. Willecke, V. K. Verselis, and F. F. Bukauskas, “Gating properties of heterotypic gap junction channels formed of connexins 40, 43, and 45.,” *Biophys. J.*, vol. 92, no. March, pp. 1952–1965, 2007.

[39] V. Valiunas, R. Weingart, and P. R. Brink, “Formation of Heterotypic Gap Junction Channels by Connexins 40 and 43,” *Circ. Res.*, vol. 86, no. Cx, pp. e42–e49, 2000.

[40] S. W. Yum *et al.*, “Human connexin26 and connexin30 form functional heteromeric and heterotypic channels,” *Am. J. Physiol. - Cell Physiol.*, vol. 293, no. 3, 2007.

[41] A. P. Moreno, “Biophysical properties of homomeric and heteromultimeric channels formed by cardiac connexins,” *Cardiovasc. Res.*, vol. 62, pp. 276–286, 2004.

[42] A. D. Martinez, V. Hayrapetyan, A. P. Moreno, and E. C. Beyer, “Connexin43 and Connexin45 Form Heteromeric Gap Junction Channels in Which Individual Components Determine Permeability and Regulation,” *Circulation*, pp. 1100–1107, 2002.

[43] S. Elenes, A. D. Martínez, M. Delmar, E. C. Beyer, and A. P. Moreno, “Heterotypic docking of Cx43 and Cx45 connexons blocks fast voltage gating of Cx43,” *Biophys. J.*, vol. 81, no. 3, pp. 1406–1418, 2001.

[44] S. R. Robinson, E. C. Hampson, M. N. Munro, and D. I. Vaney, “Unidirectional coupling of gap junctions between neuroglia.,” *Science*, vol. 262, no. 5136, pp. 1072–4, 1993.

[45] M. S. Kim, G. B. Gloor, and D. Bai, “The distribution and functional properties of Pelizaeus-Merzbacher-like disease-linked Cx47 mutations on Cx47/Cx47 homotypic and Cx47/Cx43 heterotypic gap junctions.,” *Biochem. J.*, vol. 452, pp. 249–58, 2013.

[46] M. M. Kreuzberg, K. Willecke, and F. F. Bukauskas, “Connexin-Mediated Cardiac Impulse Propagation: Connexin 30.2 Slows Atrioventricular Conduction in Mouse Heart,” *Trends Cardiovasc. Med.*, vol. 16, no. 8, pp. 266–272, 2006.

[47] J. Zhang, S. S. Scherer, and S. W. Yum, “Dominant Cx26 mutants associated with hearing loss have dominant-negative effects on wild type Cx26,” *Mol. Cell. Neurosci.*, vol. 47, no. 2, pp. 71–78, 2011.

[48] F. Rouan *et al.*, “Trans-Dominant Inhibition of Connexin-43 By Mutant Connexin-26: Implications for Dominant Connexin Disorders Affecting Epidermal Differentiation.,” *J. Cell Sci.*, vol. 114, no. 11, pp. 2105–2113, 2001.

[49] E. C. Beyer, L. M. Davis, J. E. Saffitz, and R. D. Veenstra, “Cardiac intercellular communication: consequences of connexin distribution and diversity.,” *Brazilian J. Med. Biol. Res. = Rev. Bras. Pesqui. medicas e Biol.*, vol. 28, no. 4, pp. 415–25,

Apr. 1995.

[50] H. W. Vliegen, A. Van Der Laarse, C. J. Cornelisse, and F. Eulderink, “Myocardial changes in pressure overload-induced left ventricular hypertrophy: A study on tissue composition, polyploidization and multinucleation,” *Eur. Hear. J.*, vol. 12, no. 4, pp. 488–494, Apr. 1991.

[51] G.-R. Li, H.-Y. Sun, J.-B. Chen, Y. Zhou, H.-F. Tse, and C.-P. Lau, “Characterization of multiple ion channels in cultured human cardiac fibroblasts.,” *PLoS One*, vol. 4, no. 10, p. e7307, Jan. 2009.

[52] L. Chilton *et al.*, “K+ currents regulate the resting membrane potential, proliferation, and contractile responses in ventricular fibroblasts and myofibroblasts.,” *Am. J. Physiol. Heart Circ. Physiol.*, vol. 288, no. 6, pp. H2931-9, Jun. 2005.

[53] K. B. Walsh and J. Zhang, “Neonatal rat cardiac fibroblasts express three types of voltage-gated K+ channels: regulation of a transient outward current by protein kinase C.,” *Am. J. Physiol. Heart Circ. Physiol.*, vol. 294, no. 2, pp. H1010-7, Feb. 2008.

[54] G. Gaudesius, M. Miragoli, S. P. Thomas, and S. Rohr, “Coupling of cardiac electrical activity over extended distances by fibroblasts of cardiac origin.,” *Circ. Res.*, vol. 93, no. 5, pp. 421–8, Sep. 2003.

[55] W. a LaFramboise *et al.*, “Cardiac fibroblasts influence cardiomyocyte phenotype in vitro.,” *Am. J. Physiol. Cell Physiol.*, vol. 292, no. 5, pp. C1799-808, May 2007.

[56] V. V. Petrov, R. H. Fagard, and P. J. Lijnen, “Stimulation of Collagen Production by Transforming Growth Factor-beta1 During Differentiation of Cardiac Fibroblasts to Myofibroblasts,” *Hypertension*, vol. 39, no. 2, pp. 258–263, Feb. 2002.

[57] S. Rohr, “Myofibroblasts in diseased hearts: New players in cardiac arrhythmias?,” *Hear. Rhythm*, vol. 6, no. 6, pp. 848–856, Jun. 2009.

[58] B. Burstein and S. Nattel, “Atrial fibrosis: mechanisms and clinical relevance in atrial fibrillation.,” *J. Am. Coll. Cardiol.*, vol. 51, no. 8, pp. 802–9, Feb. 2008.

[59] K. T. Weber, “Fibrosis and hypertensive heart disease.,” *Curr. Opin. Cardiol.*, vol. 15, no. 4, pp. 264–72, Jul. 2000.

[60] K. A. Yamada, J. G. Rogers, R. Sundset, T. H. Steinberg, and J. E. Saffitz, “Up-Regulation of Connexin45 in Heart Failure,” *J. Cardiovasc. Electrophysiol.*, vol. 14, no. 11, pp. 1205–1212, 2003.

[61] K. Goshima, “Formation of nexuses and electrotonic transmission between myocardial and FL cells in monolayer culture.,” *Exp. Cell Res.*, vol. 63, no. 1, pp. 124–130, Nov. 1970.

[62] L. Chilton, W. R. Giles, and G. L. Smith, “Evidence of intercellular coupling between co-cultured adult rabbit ventricular myocytes and myofibroblasts.,” *J. Physiol.*, vol. 583, no. Pt 1, pp. 225–36, Aug. 2007.

[63] P. Camelliti, C. R. Green, I. LeGrice, and P. Kohl, “Fibroblast network in rabbit sinoatrial node: structural and functional identification of homogeneous and heterogeneous cell coupling.,” *Circ. Res.*, vol. 94, no. 6, pp. 828–35, Apr. 2004.

[64] A. M. De Mazière, A. C. Van Ginneken, R. Wilders, H. J. Jongsma, and L. N. Bouman, “Spatial and functional relationship between myocytes and fibroblasts in the rabbit sinoatrial node.,” *J. Mol. Cell. Cardiol.*, vol. 24, no. 6, pp. 567–578, 1992.

[65] T. A. Quinn *et al.*, “Electrotonic coupling of excitable and nonexcitable cells in the heart revealed by optogenetics.,” *Proc. Natl. Acad. Sci. U. S. A.*, p. 1611184114-, 2016.

[66] P. Camelliti, C. R. Green, and P. Kohl, “Structural and functional coupling of cardiac myocytes and fibroblasts.,” *Adv. Cardiol.*, vol. 42, pp. 132–149, Jan. 2006.

[67] C. Vasquez, N. Benamer, and G. Morley, “The cardiac fibroblast: functional and electrophysiological considerations in healthy and diseased hearts,” *J. Cardiovasc. …*, vol. 57, no. 4, pp. 380–388, 2011.

[68] P. Kohl and P. Camelliti, “Cardiac myocyte-nonmyocyte electrotonic coupling: implications for ventricular arrhythmogenesis.,” *Heart Rhythm*, vol. 4, no. 2, pp. 233–5, Feb. 2007.

[69] P. Kohl, P. Camelliti, F. L. Burton, and G. L. Smith, “Electrical coupling of fibroblasts and myocytes: relevance for cardiac propagation.,” *J. Electrocardiol.*, vol. 38, no. 4 Suppl, pp. 45–50, Oct. 2005.

[70] P. Kohl and R. G. Gourdie, “Fibroblast-myocyte electrotonic coupling: Does it occur in native cardiac tissue?,” *J. Mol. Cell. Cardiol.*, Jan. 2014.

[71] P. Kohl and P. Camelliti, “Fibroblast–myocyte connections in the heart,” *Hear. Rhythm*, vol. 9, no. 3, pp. 461–464, 2012.

[72] H. Duffy, “Fibroblasts, myofibroblasts, and fibrosis: fact, fiction, and the future,” *J. Cardiovasc. Pharmacol.*, vol. 57, no. 4, pp. 373–375, 2011.

[73] P. Meda, “Probing the Function of Connexin Channels in Primary Tissues,” *Methods*, vol. 20, no. 2, pp. 232–244, 2000.

[74] M. H. Juul, E. Rivedal, T. Stokke, and T. Sanner, “Quantitative Determination of Gap Junction Intercellular Communication Using Flow Cytometric Measurement of Fluorescent Dye Transfer,” *Cell Commun. Adhes.*, vol. 7, no. 6, pp. 501–512, Jan. 2000.

[75] Y. Kanno and W. R. Loewenstein, “Intercellular Diffusion,” *Science (80-.).*, vol. 143, no. 3609, 1964.

[76] H. Opsahl and E. Rivedal, “Quantitative Determination of Gap Junction Intercellular Communication by Scrape Loading and Image Analysis,” *Cell Commun. Adhes.*, vol. 7, no. 5, pp. 367–375, Jan. 2000.

[77] M. H. el-Fouly, J. E. Trosko, and C. C. Chang, “Scrape-loading and dye transfer. A rapid and simple technique to study gap junctional intercellular communication.,” *Exp. Cell Res.*, vol. 168, no. 2, pp. 422–30, 1987.

[78] M. H. Wade, J. E. Trosko, and M. Schindler, “A fluorescence photobleaching assay of gap junction-mediated communication between human cells.,” *Science*, vol. 232, no. 4749, pp. 525–8, 1986.

[79] J. Lippincott-Schwartz, E. Snapp, and A. Kenworthy, “Studying protein dynamics in living cells,” *Nat. Rev. Mol. Cell Biol.*, vol. 2, no. 6, pp. 444–456, Jun. 2001.

[80] E. A. J. Reits and J. J. Neefjes, “From fixed to FRAP: measuring protein mobility and activity in living cells.,” *Nat. Cell Biol.*, vol. 3, no. 6, pp. E145–E147, Jun. 2001.

[81] K. Ziambaras, F. Lecanda, T. H. Steinberg, and R. Civitelli, “Cyclic Stretch Enhances Gap Junctional Communication Between Osteoblastic Cells,” *J. Bone Miner. Res.*, vol. 13, no. 2, pp. 218–228, Feb. 1998.

[82] G. S. Goldberg, J. F. Bechberger, and C. C. G. Naus, “A pre-loading method of evaluating gap junctional communication by fluorescent dye transfer,” *Biotechniques*, vol. 18, no. 3, pp. 490–497, Mar. 1995.

[83] K. Dakin, Y. Zhao, and W.-H. Li, “LAMP, a new imaging assay of gap junctional communication unveils that Ca2+ influx inhibits cell coupling,” *Nat. Methods*, vol. 2, no. 1, pp. 55–62, Jan. 2005.

[84] D. C. Spray, “Illuminating gap junctions,” *Nat. Methods*, vol. 2, no. 1, pp. 12–14, Jan. 2005.

[85] S. J. Cruikshank, M. Hopperstad, M. Younger, B. W. Connors, D. C. Spray, and M. Srinivas, “Potent block of Cx36 and Cx50 gap junction channels by mefloquine,” *Proc Natl Acad Sci U S A*, vol. 101, no. 33, pp. 12364–12369, Aug. 2004.

[86] D. M. Larson and J. D. Sheridan, “Junctional transfer in cultured vascular endothelium: II. Dye and nucleotide transfer,” *J. Membr. Biol.*, vol. 83, no. 1–2, pp. 157–167, Feb. 1985.

[87] A. C. Charles, C. C. Naus, D. Zhu, G. M. Kidder, E. R. Dirksen, and M. J. Sanderson, “Intercellular Calcium Signaling via Gap Junction in glioma cells,” *J. Cell Biol.*, vol. 118, no. july, pp. 195–201, 1992.

[88] J. Sneyd, B. T. Wetton, A. C. Charles, and M. J. Sanderson, “Intercellular calcium waves mediated by diffusion of inositol trisphosphate: a two-dimensional model.,” *Am. J. Physiol.*, vol. 268, no. 6 Pt 1, pp. C1537-45, 1995.

[89] J. Sneyd, A. C. Charles, and M. J. Sanderson, “A model for the propagation of intercellular calcium waves,” *Am. J. Physiol. - Cell Physiol.*, vol. 266, no. 1, 1994.

[90] G. Grynkiewicz, M. Poenie, and R. Y. Tsien, “A new generation of Ca2+ indicators with greatly improved fluorescence properties,” *Journal of Biological Chemistry*, vol. 260, no. 6. American Society for Biochemistry and Molecular Biology, pp. 3440–3450, 25-Mar-1985.

[91] A. Minta, J. P. Y. Kao, and R. Y. Tsien, “Fluorescent indicators for cytosolic calcium based on rhodamine and fluorescein chromophores,” *J. Biol. Chem.*, vol. 264, no. 14, pp. 8171–8178, May 1989.

[92] C. del Corsso *et al.*, “Transfection of mammalian cells with connexins and measurement of voltage sensitivity of their gap junctions,” *Nat. Protoc.*, vol. 1, no. 4, pp. 1799–809, Jan. 2006.

[93] M. Miragoli, G. Gaudesius, and S. Rohr, “Electrotonic modulation of cardiac impulse conduction by myofibroblasts.,” *Circ. Res.*, vol. 98, no. 6, pp. 801–10, Mar. 2006.

[94] S. Zlochiver, V. Muñoz, K. L. Vikstrom, S. M. Taffet, O. Berenfeld, and J. Jalife, “Electrotonic myofibroblast-to-myocyte coupling increases propensity to reentrant arrhythmias in two-dimensional cardiac monolayers.,” *Biophys. J.*, vol. 95, no. 9, pp. 4469–80, Nov. 2008.

[95] M. Miragoli, N. Salvarani, and S. Rohr, “Myofibroblasts induce ectopic activity in cardiac tissue.,” *Circ. Res.*, vol. 101, no. 8, pp. 755–8, Oct. 2007.

[96] J. P. Fahrenbach, R. Mejia-Alvarez, and K. Banach, “The relevance of non-excitable cells for cardiac pacemaker function.,” *J. Physiol.*, vol. 585, no. Pt 2, pp. 565–78, Dec. 2007.

[97] K. Goshima, “Synchronized beating of and electrotonic transmission between myocardial cells mediated by heterotypic strain cells in monolayer culture.,” *Exp. Cell Res.*, vol. 58, no. 2, pp. 420–426, 1969.

[98] B. C. Schwab *et al.*, “Quantitative analysis of cardiac tissue including fibroblasts using three-dimensional confocal microscopy and image reconstruction: towards a basis for electrophysiological modeling.,” *IEEE Trans. Med. Imaging*, vol. 32, no. 5, pp. 862–72, May 2013.

[99] F. B. Sachse, A. P. Moreno, G. Seemann, and J. A. Abildskov, “A model of electrical conduction in cardiac tissue including fibroblasts.,” *Ann. Biomed. Eng.*, vol. 37, no. 5, pp. 874–89, May 2009.

[100] Y. Xie, A. Garfinkel, P. Camelliti, P. Kohl, J. Weiss, and Z. Qu, "Effects of fibroblast-myocyte coupling on cardiac conduction and vulnerability to reentry: a computational study," *Hear. Rhythm*, vol. 6, no. 11, pp. 1641–1649, 2009.

[101] M. M. Maleckar, J. L. Greenstein, W. R. Giles, and N. a Trayanova, "Electrotonic coupling between human atrial myocytes and fibroblasts alters myocyte excitability and repolarization.," *Biophys. J.*, vol. 97, no. 8, pp. 2179–90, Oct. 2009.

[102] P. Zhang, J. Su, and U. Mende, "Cross talk between cardiac myocytes and fibroblasts: from multiscale investigative approaches to mechanisms and functional consequences.," *Am. J. Physiol. Heart Circ. Physiol.*, vol. 303, no. 12, pp. H1385-96, Dec. 2012.

[103] T. Kwon, A. L. Harris, A. Rossi, and T. A. Bargiello, "Molecular dynamics simulations of the Cx26 hemichannel: evaluation of structural models with Brownian dynamics," *J. Gen. Physiol.*, vol. 138, no. 5, pp. 475–93, 2011.

[104] F. Zonta, D. Buratto, C. Cassini, M. Bortolozzi, and F. Mammano, "Molecular dynamics simulations highlight structural and functional alterations in deafness related M34T mutation of connexin 26," *Front. Physiol.*, vol. 5, p. 85, Mar. 2014.

[105] M. J. Madou, *Fundamentals of Microfabrication: The Science of Miniaturization, Second Edition*. CRC Press, 2002.

CHAPTER 2

PERFLEXMEA: A THIN MICROPOROUS MICROELECTRODE ARRAY FOR *IN VITRO* CARDIAC ELECTROPHYSIOLOGY STUDIES ON HETERO-CELLULAR BILAYERS WITH CONTROLLED GAP JUNCTION COMMUNICATION

Mondal A, Baker B, Harvey IR, Moreno AP. PerFlexMEA: a thin microporous microelectrode array for *in vitro* cardiac electrophysiological studies on hetero-cellular bilayers with controlled gap junction communication. *Lab Chip* 2015, 15, 2037-2048.

Lab on a Chip

PAPER

View Article Online
View Journal | View Issue

Cite this: *Lab Chip*, 2015, 15, 2037

PerFlexMEA: a thin microporous microelectrode array for *in vitro* cardiac electrophysiological studies on hetero-cellular bilayers with controlled gap junction communication

A. Mondal,*[ac] B. Baker,[b] I. R. Harvey[b] and A. P. Moreno*[ac]

Received 14th October 2014,
Accepted 7th March 2015

DOI: 10.1039/c4lc01212g

www.rsc.org/loc

The new microelectrode array device presented is called PerFlexMEA and it enables controlled coupling between myocytes and nonmyocytes used in cardiovascular conduction studies. The device consists of an 8 μm thin parylene microporous membrane with a 4 × 5 microelectrode array patterned on one side. Myocytes and nonmyocytes can be plated on either side of the parylene membrane to create a tissue bilayer. The 3–3.5 μm diameter pores allow inter-layer dye and electrical coupling without transmembrane cell migration. Cell migration was found to vary with cell-type and micropore diameter. Pore density can be varied based on desired coupling ratio. The flexible parylene membrane is packaged between two rigid thermoplastic layers, such that the microelectrode array region is exposed, while the rest of the device remains insulated. The packaged PerFlexMEA fits in a 60 mm culture dish. Recording experiments are performed by simply plugging it into a commercially available multielectrode amplifier system. Recorded signals were processed and analysed using scripts generated in MATLAB. Our experimental results provide evidence of the reliability of this device, as conduction velocity was observed to decrease after inducing lateral hetero-cellular controlled coupling between myocytes and HeLa cells expressing connexin 43.

Introduction

Heart disease is the leading cause of deaths in the United States with the expected annual incidences of sudden cardiac deaths ranging from 180 000–250 000 per year.[1,2] An overwhelming majority of these cases are a result of conduction failures in the heart tissue.[3,4] Most cardiac failure events are followed by myocardial remodelling involving fibrosis, where fibroblasts/myofibroblasts and extracellular matrix (ECM) accumulate rapidly near the scar regions attempting tissue healing.[5,6] While in healthy cardiac tissue, conduction occurs only through the myocytes, in the diseased state fibroblasts have been observed to electrically couple with myocytes *in vivo*[7,8] and *in vitro*.[9–11] Furthermore, fibroblasts have also been observed to differentiate into myofibroblasts,[12] which can slow electric conduction too after coupling with myocytes.[13] Such electrotonic coupling between myocytes and nonmyocytes (fibroblasts and myofibroblasts) can have significant electrophysiological effects on the heart, including conduction abnormalities and conduction failure. While electrophysiological properties of myocyte–nonmyocyte electrotonic coupling have been studied in cell pairs,[14,15] studies on conduction effects have also been performed in monolayers,[9,10,16–20] some 3D tissue constructs,[21,22] and computational models.[23–26] Computational models are able to control and mimic tissue architecture and coupling properties for electrophysiological studies, but experimental models provide little or no control. Some *in vitro* models involve adding nonmyocytes on myocyte monolayers,[13,17,27–30] and others involve organizing myocytes and nonmyocytes through patterning microstructures and/or ECM on substrates.[31–33] The former approach is not architecturally accurate as nonmyocytes migrate and can become intercalated or lateral to the conduction pathway. The latter approach provides greater architectural accuracy, but allows no control over the extent of myocyte–nonmyocyte coupling and limits electrophysiological studies in linear or curvilinear tissue preparations. Furthermore, in the latter approaches, experiment protocols are fairly sophisticated and require considerable amount of pre-plating work for each experiment.

To address these shortcomings of current experimental models designed for studying electrophysiological effects of myocyte–nonmyocyte interactions, we looked into available

[a] *Nora Eccles Harrison Cardiovascular Research & Training Institute, University of Utah, 95 South 2000 East, Salt Lake City, UT 84112-5000, USA. E-mail: abhijit.mondal@utah.edu, moreno@cvrti.utah.edu*
[b] *Utah Nanofab, University of Utah, 36 S. Wasatch Drive, SMBB Rm 2500, Salt Lake City, UT 84112, USA*
[c] *Department of Bioengineering, University of Utah, 20 South 2030 East, BPRB Rm. 108, Salt Lake City, UT 84112-9458, USA*

manufacturing methods of micro-featured materials and tissue culture techniques. Various biomaterials have been utilized for culturing and developing tissues for modelling and studying different diseased states. Substrate porosity is a significant physical feature for tissue growth, function and maintenance in *in vitro* experiments as it facilitates nutrient perfusion, intercellular communication and limits cell migration.[34–39] Physical intercellular communication without cell migration has been observed with commercially available[40] ~10 μm thin polycarbonate substrates with 3–5 μm diameter pores.[41] While membrane thickness and pore density can regulate the amount of gap junction formed, pore size restricts cell migration; this way, micropores in the range of 3 to 5 μm constitute an important geometric feature in allowing inter-layer communication while preventing transmembrane cell migration[42] (during this manuscript, "transmembrane" will refer to migration events across the thin microporous membrane). Thus, by controlling membrane thickness and pore density, the amount of intercellular communication between two cell layers can be regulated. Monitoring the effects of such regulated communication in excitable cells can be studied by a variety of methods like microscopy, radioactive tracing, cell fractionation techniques, cell imaging and biochemical methods. Most of these methods are complicated and require sophisticated equipment and dyes. Non-invasive extracellular recording using microelectrode arrays (MEA) constitutes a simpler way of recording electrophysiological activity from excitable tissues including cell culture[43–46] and tissue slices,[47–49] and offers multiple advantages: first, they allow simultaneous recording from multiple sites rather than from individual cells. Second, they enable simultaneous recording from a large number of sites. To date, detection from as many as 4096 sites have been reported.[44] Third, the micro-environment for these MEA devices is easier to control in cell cultures and tissue slices *in vitro*, allowing continuous recordings for several days.

Our approach has been to integrate the MEA concept with a biocompatible thin microporous membrane where myocytes and nonmyocytes can be plated on either side of the membrane. The micropore size prevents transmembrane migration while pore-density will control the amount of allowable inter-layer coupling. The MEA embedded on one side of the membrane facilitates recording field potentials from the myocyte layer.

In this paper we present a device called "Perforated Flexible MEA" (PerFlexMEA). The device enables co-culturing myocytes and nonmyocytes in a bilayer such that there is controlled inter-layer coupling without cell migration between the two layers. This is accomplished through a thin microporous parylene membrane sandwiched between the two cell layers. A 4 × 5 MEA embedded on the myocyte side records its conduction activity with and without inter-layer coupling. The electrode array and insulator were patterned using lithography and etching. Gold, a commonly used electrode material in flexible MEA devices,[50–54] was selected as the electrode material due to its high conductivity, chemical inertness and ease of deposition and patterning. Parylene, a biocompatible insulator,[55–57] was also used to insulate the metal leads. Dye coupling (representing large molecular coupling between cells) and cell migration experiments were conducted where HeLa cells expressing connexin 43 (HeLaCx43)[58] were selected as nonmyocytes over cardiac fibroblasts, as the latter presents a high migration rate even through Ø3–3.5 μm pores which disrupts the desired tissue architecture and control over myocyte–nonmyocyte coupling. Inter-layer coupling was demonstrated between HeLaCx43 cells and effects of myocytes–nonmyocyte coupling on conduction velocity were determined. Our current results suggest that the PerFlexMEA can become the standard platform for studying the electrophysiological effects of myocytes–nonmyocyte coupling in upcoming research.

Material and methods

Device design and material selection

Our overall design goal was to create a device that controls intercellular coupling between two cell layers (myocytes and nonmyocytes) while being able to monitor the electrophysiological activity of one of them (myocytes). To achieve this, our structural design consists of placing a microporous membrane between the two cell layers. Micropore density controls the amount of dye and electrical communication between the two cell layers: myocyte and nonmyocyte layers, while preventing any transmembrane cell migration. The embedded MEA on the myocyte-plated side of the membrane records the field potentials, which can be further processed for calculating conduction velocity. Fig. 1A illustrates our basic experimental setup.

PerFlexMEA design. The PerFlexMEA was designed to fulfil the functional objectives of co-culturing two cell types while permitting the formation of gap junction between them and recording the electrical activity of the preparation, taking into consideration the constraints in dimensions, accessible materials and fabrication methods. Based on the experimental structure shown in Fig. 1A, we designed the PerFlexMEA (Fig. 1B) with three functional regions: (a) cell culture zone, (b) insulated leads and (c) contact pads. Parylene was chosen as the membrane material due to its wide use as a biocompatible material[55–57,59] and inertness to microfabrication solvents and chemicals. The cell culture zone is maintained wet in media during culture and recording experiments and has two main functional features: a 20 (4 × 5) recording microelectrode array and micropores. The cells are cultured on either side of the ~8 μm thick membrane with the electrogenic cells (MYO) on the MEA side. The 4 × 5 array of Ø30 μm round planar electrodes, spaced 500 μm apart create a recording area of 1.5 mm × 2 mm. Gold leads (50 μm wide) connect the recording electrodes to the 1 mm × 1 mm square contact pads. Gold was selected as the material for the recording electrodes, leads and contact pads due to its high flexibility, good adhesion to parylene, high electrical conductivity and biocompatibility. The leads are insulated from the

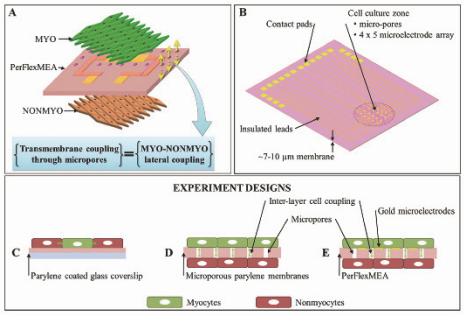

Fig. 1 Experiment and device design. (A) Basic experiment design. A thin micro-porous membrane is sandwiched between the myocyte and nonmyocyte layer to control myocyte–nonmyocyte coupling while recording myocyte extracellular field potentials. (B) PerFlexMEA membrane design. All microfeatures are patterned on the thin Parylene membrane. The cell culture zone is maintained wet while the contact pads are maintained dry. Insulated leads connect the recording electrodes in the cell culture zone to the contact pads. The Ø5 mm cell culture zone includes a 4 × 5 microelectrode array and Ø3–3.5 μm pores arranged in 20 μm square-side pitch. (C–E) Experiment designs for functional characterization of the PerFlexMEA. (C) Cells cultured on parylene coated coverslips for biocompatibility and as controls of coupling experiments. (D) Myocytes and nonmyocytes cultured on either side of a micro-porous parylene membrane for inter-layer coupling and transmembrane migration experiments. (E) Myocytes and nonmyocytes cultured on either side of the PerFlexMEA for electrophysiological experiments.

top to avoid recording additional signals from them. The contact pads are used to interface the PerFlexMEA with the amplifier system. Thin connecting cables are soldered with silver conductive epoxy (MG chemicals, CAT #: 8331-14G) to the contact pads. The contact pads and the leads are sealed with PDMS (Dow Corning Corp., Midland, MI) to keep them dry.

Experiment designs for PerFlexMEA functional characterization

Functional requirements of this device consists of four aspects:

1. Cell culture and function on parylene: parylene is not a standard cell culture substrate. Hence, biocompatibility of myocytes and nonmyocytes needed to be tested.

2. Prevention of transmembrane cell migration: to control the amount of coupling and maintain tissue architecture, it is imperative that the cells do not migrate through the pores.

3. Inter-layer cell coupling: inter-layer coupling in the newly developed microporous parylene membrane needed to be tested.

4. Field potential recording and conduction velocity calculation: all microelectrodes should be able to record field potentials for conduction studies.

To test the above mentioned requirements, two more testing parts were fabricated. Parylene coated glass coverslips (Fig. 1C) for biocompatibility and control coupling experiments, and microporous parylene membranes (without MEA; Fig. 1D) for testing transmembrane cell migration and inter-layer coupling in myocyte–nonmyocyte bilayers.

Cell coupling and migration experiments with microporous parylene membranes. For cell coupling experiments we used a dual dye system. Myocytes were stained with Calcein AM (Molecular Probes, cat # C3100MP) which is membrane permeable. Inside the cell, esterases cleave the AM portion to form Calcein, a cell-membrane impermeable molecule capable of moving within the cytoplasm and diffusing across gap junctions. The nonmyocyte cell layer was stained with DiI (Molecular Probes, cat #D282), a lipophilic dye that stays in cell membranes. The presence of Calcein in DiI stained cells indicated cell-to-cell coupling. Both cell types were plated on parylene coated cover slips (controls) and microporous parylene membranes (membrane pore diameters: 3–3.5 μm, 5–6 μm and 7–7.5 μm) as shown in Fig. 1C and D respectively.

In bilayer preparations, any stained cells appearing on the opposite side of plating indicate cell migration through pores. Migration experiments were also performed after plating monolayers of one cell type on one side of the microporous membrane.

Electrophysiological experiments with PerFlexMEA for effects of controlled cell-coupling. As shown in Fig. 1E, myocytes were plated on the microelectrode array side of the PerFlexMEA. Electrophysiological recordings were conducted before and after plating nonmyocytes (HeLaCx43).

Device fabrication and assembly

The PerFlexMEA, microporous parylene membranes and parylene coated coverslips were fabricated at the University of Utah Nanofab facility. The recording devices were packaged at the Connexin lab, CVRTI.

PerFlexMEA fabrication and packaging. Fig. 2 summarizes the fabrication steps involved to create a PerFlexMEA. Since lithography requires a rigid substrate for transferring the pattern using a mask, parylene had to be first deposited onto a rigid substrate. Once we have deposited and patterned all the layers, the parylene membrane can be exfoliated and used. We start with a clean 4 inch glass wafer (Fig. 2A) and spin coat a ~10 μm thick AZ9260 layer on it (Fig. 2B). The wafer is thoroughly baked (130 °C for 45 min) to remove all solvent from the photoresist layer. This prevents the formation of bumps on the parylene surface due to trapped solvent vapours caused by further wafer baking in lithography. Parylene is deposited on this AZ9260 layer using a low pressure chemical vapour deposition process (LPCVD) to form a ~8 μm thick membrane (Fig. 2C). This is our base membrane. The parylene surface is mildly etched with oxygen plasma before sputtering 120 nm of gold (Fig. 2E–F). A pre-sputter oxygen plasma etch promotes gold adhesion (Fig. 2D). The gold layer is patterned (Fig. 2G) to form recording electrodes, leads and contact pads through lithography and wet etching

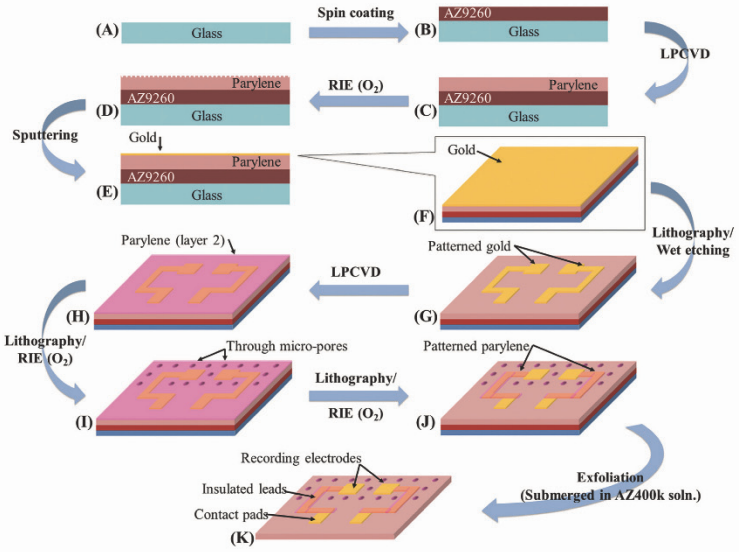

Fig. 2 PerFlexMEA fabrication process. (A) Clean 4" glass wafer for creating a flat parylene membrane. (B) Spin-coating 8–10 μm layer of AZ9260 on glass as sacrificial layer. (C) Parylene deposition by LPCVD. (D) Reactive ion etching of parylene surface coarsening the parylene surface for metal adhesion. (E) Conductor layer (gold) deposition by sputtering. (F) View of the top surface coated with gold. (G) Patterning of metal layers by lithography and wet etching (in yellow). (H) Parylene coat (layer 2; in translucent pink) covering the patterned metal layer. (I) Creating Ø3–3.5 μm through micropores by lithography and RIE. Chromium was used for patterning the micropores. (J) Parylene patterning. After patterning, leads are insulated by parylene from the top, whereas the electrodes and contact pads are left exposed. (K) Exfoliation of membrane from glass wafer.

(KI/I_2 solution). Next a ~0.6 μm of parylene layer is deposited (Fig. 2H). While this parylene layer is primarily deposited to be patterned later as lead insulators, it also protects the gold layer from the sacrificial chrome layer used for patterning the micropores in the upcoming steps. Next a ~40 nm chrome layer is deposited by sputtering. The chrome layer is used for patterning all the Ø3–3.5 μm micropores. The pore pattern is transferred onto the chrome layer using lithography and wet etching (CR-14 etchant). The micropores are patterned onto the parylene membrane by reactive ion etching (RIE) in oxygen (Fig. 2I). Once the micropores are etched, the chrome layer is stripped using CR-14 etchant. Insulation on the leads is then patterned using lithography and oxygen plasma etching (Fig. 2J). Once the leads are patterned, the devices are ready to be exfoliated from the glass wafer. The wafer containing the devices is submerged in AZ400k. AZ400k dissolves the photoresist (AZ9260) under each device starting from the edges. Once all of AZ9260 is dissolved, the PerFlexMEA membranes float (Fig. 2K). Each device is carefully picked up using tweezers and washed thoroughly in DI water. Once washed, the PerFlexMEAs are stored in 70% ethanol (EtOH) to keep them sterile for cell culture.

To interface the PerFlexMEA with the amplifier systems, the PerFlexMEA is packaged such that the cell-culture zone can be maintained wet, while the remaining regions dry. Also, both the top and bottom sides of the PerFlexMEA need to be accessible for cell plating. The PerFlexMEA membrane is simply sandwiched between two thin PCTFE plates with through Ø5 mm holes aligned co-axially at the cell culture zone. The top PCTFE plate only covers the front half of the PerFlexMEA, leaving the contact pads exposed. Wires from a 20 pin connector are soldered to the contact pads using conductive silver-epoxy. The remaining half of the top side was moulded with PDMS to seal the contact pads. Fig. 3A shows a packaged PerFlexMEA device.

Microporous parylene membrane fabrication and packaging. The microporous parylene membranes are fabricated using parylene deposition (Fig. 2A–D), pore patterning (Fig. 2H–I) and exfoliation steps (Fig. 2K) of the PerFlexMEA fabrication process. The microporous parylene membranes are also stored in 70% EtOH.

The membranes were packaged by sandwiching it between two nylon M5 washers with the cell membrane culture zone aligned coaxially to the washers. The washers were glued to the membrane using silicone adhesive. The use of silicone adhesive allows the microporous parylene membrane to be manually extracted from the assembly later for confocal imaging. The full assembly was thoroughly washed in DI rinse and sterilized using 70% EtOH before cell culture.

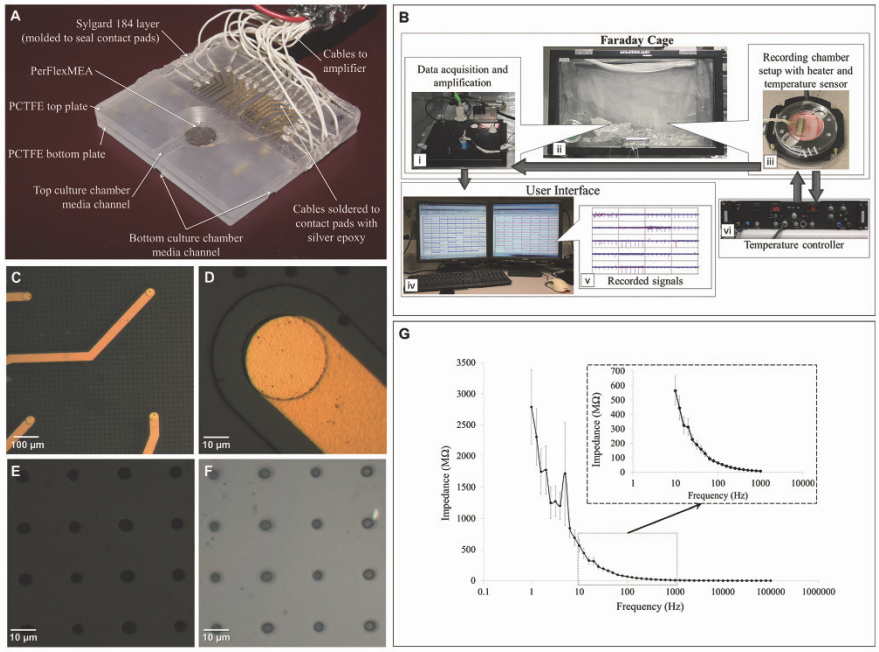

Fig. 3 PerFlexMEA packaging, interface and characterization. (A) Packaging. The PerFlexMEA is sandwiched between the top and bottom PCTFE plates. Cables to amplifiers, leads and contact pads are covered with PDMS. (B) Electrophysiological recording setup. (i) Data acquisition and amplification system. (ii) Faraday cage. (iii) Packaged PerFlexMEA with cell preparation in micro-incubator. (iv) MCRack user interface. (v) Recorded signals. (vi) Micro-incubator temperature controller. (C–F) Microscopic images of PerFlexMEA cell culture zone features. While (C–E) were imaged from the MEA side of the device, (F) was imaged from the nonMEA side. (C) Four Ø30 µm microelectrodes with their respective parylene insulated leads. The black dots around the microelectrodes and leads are micropores. (D) A single recording gold microelectrode with parylene insulation covering its lead. (E) The micropores imaged from the MEA side of the PerFlexMEA vary from Ø3.3–4.5 µm. (F) Micropores imaged on the nonMEA side of the PerFlexMEA vary from Ø2.5–3.5 µm. (G) Electrode impedance as a function of frequency (1 Hz to 100 kHz). Average values of electrode impedances are shown. Standard error bars are also indicated (n = 80).

Parylene coated coverslips fabrication. Commercially available Ø12 mm glass coverslips were coated with ~0.6 µm thick parylene using LPCVD process.

Microelectrode impedance measurement. A Gamry reference 600 potentiostat (Gamry Instruments Inc., Warminster, PA) was used for measuring single electrode impedances for a frequency range between 1 Hz and 100 kHz. The electrode impedances were measured in 1× PBS solution.

Cell sources, culture and experiments

Rat neonatal ventricular cell isolation for *in vitro* experiments. This isolation protocol follows the guidelines of Worthington Biochemical Corporation (Lakewood, NJ, 08701). All animal handling protocols followed the University of Utah IACUC regulations. In short, all neonatal rat pups (2 days old) are anesthetized (isoflurane vapours) and their skin sterilized with 70% EtOH. Pups are immediately decapitated and their hearts excised. Atria and non-ventricular tissue are removed. All tissue is minced and left in CMF-Trypsin solution for 18 hours at 4 °C. Tissue is later brought to 37 °C; tissue fragments are placed in a conical tube with collagenase in Leibovitz L-15 media and shaken slowly for 45 min at 37 °C. The tissue is triturated with a pipette for 10 times, strained with L-15 media. Tissue residue is left 20 min for further enzymatic action. After slow centrifugation (50 × g) the pelleted cells are re-suspended in DMEM-CM and transferred into a 60 mm petri dish, which is then incubated (37 °C, 6% CO_2, moisture) for 45 minutes until fibroblast adhesion is observed (using 20× microscope). The myocyte-rich media is removed and pelleted by low speed centrifugation. Myocytes are re-suspended in 300 µM BrdU DMEM solution (BrdU controls fibroblast growth) and plated on the appropriate recording substrates.

Cell culture zone preparation and cell plating. The alcohol-sterilized PerFlexMEAs are dried and the cell culture

zone is submerged in 10 μL mL^{-1} solution of fibronectin for 2 hours. Fibronectin promotes cell adhesion to the membrane surface. To hydrate the membrane pores, PerFlexMEAs are submerged in a 60 mm petri dish with PBS and vacuumed in a glass sealed chamber for 15 min. Air, if not removed from the pores, hinders cell functioning and prevents gap junction formation across the membrane. PBS is replaced with 300 μM BrdU DMEM-CM with horse serum before cell plating [DMEM solution: HyQ DMEM/High Glucose (Hyclone# SH30243.01), 10% FBS Fetal Bovine Serum (Hyclone# SH 30070.03), 1% Pen Strep [10000 ui Penicilin, 10 000 μg ml^{-1} Streptomycin, 25 μg ml^{-1} Amphotericin B] (Cellgro# 30-004-Cl), 1% L-glutamine 200 mM (Cellgro# 25-005-Cl) and 1% non-essential-amino acids (Sigma# M7145)]. 300 μM BRDU is added to our culturing media (DMEM) to restrict fibroblast growth. 50 000 neonatal rat myocytes were plated on the MEA side of the PerFlexMEA on day 0 of each experiment. HeLaCx43 cells were plated on the other side of the microporous cell culture zone on day 5. These cells were plated after inverting the PerFlexMEA in the 60 mm petri dish and dropping the cells suspension solution in the cell culture zone.

Cell staining and imaging. All cell culture, staining and fixation experiments were conducted at the Connexin Lab, CVRTI. Confocal imaging was performed using a LSM 5 Duo confocal microscope (Carl Zeiss, Jena, Germany).

DiI and Calcein AM staining. Staining media was prepared by diluting and dissolving the respective dye in DMEM-CM (DiI – 1 : 375 000; Calcein AM – 1 : 60 000). The cells to be stained were washed with PBS and the staining media was applied. The cell culture with staining media was incubated (37 °C, 6% CO_2, moisture) for 55 minutes. After incubation, the staining media was removed, the culture washed with PBS and replaced with regular media.

Immunocytochemistry. Cell cultures were fixed in 4% paraformaldehyde and permeabilized with 0.04% Triton-X. Myocytes were identified by immunofluorescence using Troponin I rabbit polyclonal (Santa Cruz Biotechnology Inc., Dallas, TX) as primary antibody, combined with a secondary Alexa Fluor 488 Goat Anti-Rabbit IgG (H + L) antibody (Invitrogen, Carlsbad, CA) as a fluorescent probe. Nuclear staining was also done with DAPI nucleic acid stain (Invitrogen, Carlsbad, CA).

Electrophysiological recording

Recording experiments were conducted in the Connexin Lab at CVRTI, University of Utah. Once the cells were plated, the PerFlexMEA setup was incubated (37 °C, 6% CO_2, moisture) for 36–48 hours. This gave cells ample time to attach to the membrane and adapt to the new conditions. Culture media was changed every 48 hours. Field potential recording experiments were conducted from day 2 to day 7. The 60 mm petri dish holding the PerFlexMEA setup was positioned in a customized HCMIS micro-incubator (ALA Scientific Instruments, Inc., Farmingdale, US). The micro-incubator maintained the preparation at temperatures between 37–38 °C using a PTC-10 (Peltier Temperature Control) system (npi electronics GmbH, Tamm, Germany). Meanwhile, the connector/adaptor from the PerFlexMEA was plugged into the MEA amplifier (Multi Channel Systems (MCS), Reutligen, Germany). A 20 electrode connector was designed to utilize the existing 60 electrode MCS recording system. A chloridized silver wire immersed in the media was used as a ground electrode. The petri dish containing the PerFlexMEA setup was shielded with grounded aluminum foil to minimize noise in the recorded signal. The complete recording setup – PerFlexMEA, micro-incubator and MEA amplifiers – was placed in an enclosed box (Fig. 3B) with inner walls covered with aluminum mesh that worked as a Faraday cage to shield against stray noise from the outside environment. The amplifier was connected to a data acquisition computer *via* a single 68 pin MCS standard cable. The MCRack software (Multi Channel Systems, Reutligen, Germany) was customized to observe and save the recorded signals from all 20 electrodes. After each recording experiment, the PerFlexMEA setup was unplugged from the recording system, cleaned and prepared for incubation.

Conduction velocity calculation

All recorded field potentials stored in the MCRack "*.mcd*" files, were imported into MATLAB. MATLAB scripts were developed and used for calculating conduction velocities. Conduction velocity was computed by considering the time of maximum derivative of the recorded field potentials from each microelectrode. Each set of spikes within a segmented time were considered at a time for conduction velocity calculation. Within the segmented time the top 9 points (time points) of maximum derivative were identified. The time point of maximum derivative is considered the activation time. The final time point to be considered as activation time was selected by the user. Ideally, all the maximum derivative points would be very close to the highest derivative, but sometimes random system noise in the signal leads to multiple points of maximum derivatives. Hence, the user would select the relevant point of maxima to be considered as activation time. Furthermore, if there was no spike recorded from a particular electrode, the user could set it to be considered for averaging from activation times from neighbouring electrodes. Based on the microelectrode position and activation times, isochronal maps and velocity vectors were generated. Velocity vectors were calculated at each electrode position, based on the activation times of its immediate neighbouring electrodes. The 6 (3 × 2) central velocity vectors that were calculated using activation times of its 8 neighbouring electrodes were considered as preparation conduction velocities ($\overrightarrow{V_1}$ to $\overrightarrow{V_6}$). The velocity vectors calculated at the electrodes position on the edges (5 neighbouring points) and corner points (3 neighbouring points) of the electrode array were not considered.

Results and discussions

The PerFlexMEA was successfully fabricated, packaged and prepared for cell culture. Electrophysiological experiments were conducted with cell monolayers and bilayers. Experiments to test and verify inter-layer coupling and transmembrane migration were separately conducted on microporous parylene membranes. The device features and cell culture results are discussed separately below.

Microfabricated features

The microfabrication process was developed to achieve feature dimensions within predicted functional limits. Four PerFlexMEA devices were fabricated and exfoliated from each 4" glass wafer. The designed and developed microfabrication process involved 3 levels of lithography for patterning the key features: (1) conductive layer, (2) insulation layer and (3) micropores. The geometry and dimension of each of these features was monitored during fabrication. Fig. 3C–F shows images of these microfabricated features in the cell culture zone. Fig. 3C shows 4 round microelectrodes and their respective leads. The recording microelectrodes are just ends of the leads which are not insulated by parylene from above. This is clearer in the magnified (60×) images of single recording electrode (Fig. 3D). The average recording microelectrode impedance at 1 kHz was measured to be 7.5 ± 1.0 MΩ. Fig. 3G shows the average electrode impedances of 80 electrodes from 4 PerFlexMEAs at a frequency range of 1 Hz to 100 kHz. The variation in electrode impedance is very low at frequencies higher than 10 Hz.

A slight misalignment between the gold and top parylene layer was observed in few of the devices, but the difference in recording microelectrode area was negligible. Furthermore, the parylene layer insulated the leads everywhere with no exposed gold regions in any PerFlexMEA device. The microporous region (black dots around patterned gold in Fig. 3C) had slight misalignment too, but without any functional consequences on the recording electrodes or leads. Since the micropores had to be patterned using the RIE process, there were limitations to the aspect ratio of the pores. A 40 nm thick chrome layer was used as the mask to etch the pore patterns in parylene. Using AZ9260 photoresist would have required ~10 μm layer thickness as it has similar RIE etch rate as parylene. This would have more than doubled the feature aspect ratio and hindered RIE in etching the entire pores. Furthermore, it was observed that set pore diameter in the chrome masking layer had an influence on the final pore shape. Since the same membrane thickness was used to make 3 μm, 5 μm and 7 μm diameter pores on parylene, for the smaller pore size of 3 μm, the fabricated pores were slightly conical, whereas 5 μm and 7 μm diameter pores were more cylindrical. In the PerFlexMEAs the desirable pore diameter was 3 μm with an expectation of cylindrical through-pores. The actual pore mouth sizes varied in each side of the parylene membrane indicating through but conical pores. Pore diameters in the MEA side varied from 3.3–4.5 μm (Fig. 3E), while they varied from 2.5–3.5 μm on the nonMEA side (Fig. 3F). The size of gap junction channels are significantly smaller than our membrane pore size. Also, the size of gap junction plaques can be as large as the pore or significantly smaller than the pore size.[60] So the only effect we expect to see in coupling is the number of plaques formed. As the cells deliver cytoplasmic elongations to reach another cell through the pore, junctions are probably formed perpendicular to the pore. Therefore we do not expect the pores' conical shape to have any direct physiological consequences. Pore size on the other hand was a concern for inter-layer migration and affected nonmyocyte cell-type selection for our electrophysiological experiments. This has been discussed in the cell migration results. While microporous membranes and other biocompatible polymers are commercially available (Sterlitech Inc., Corning Inc.), a number of design and microfabrication problems arise. Polycarbonate track etched (Sterlitech Corp., Kent, WA) membranes were found to be reactive to acetone and photoresist solvent. This also posed limits to the baking temperatures during lithography. Furthermore, the track etched pores are randomly oriented, which makes them harder to clear after LPCVD where deposition is isotropic.

Separate sets of microporous parylene membranes were fabricated with desired pore diameters of 3 μm, 5 μm and 7 μm. The pore diameter variation was similar for the 3 μm set as observed in the PerFlexMEAs above. The pore shapes in the 5 μm microporous parylene membranes were cylindrical and with pore diameters varying from 5–6 μm. These membranes (3 μm, 5 μm and 7 μm) were used for inter-layer cell coupling and transmembrane migration experiments.

Myocyte culture on parylene

To ensure its capability in supporting tissue culture, in particular with myocytes, we performed experiments to determine cell attachment at different conditions. Fig. 4A, D–E presents confocal micrographs taken from immunostained myocytes plated on different substrates. Troponin I was used as the primary antibody for identifying myocytes. Troponins are myofibrillar proteins that regulate actin-myocin interactions, thereby controlling contraction and relaxation in myocytes. Troponin I is one of the 3 sub-units forming the troponin complex and has high cardiac specificity. The green filaments in the confocal micrographs (Fig. 4A, D and E) are the myofilaments. Myocytes plated in fibronectin treated parylene (Fig. 4E) appear larger in area and well spread, when compared to the myocytes plated on regular glass coverslips (Fig. 4D) and parylene (Fig. 4E). This is because they are better adhered to the fibronectin treated parylene substrate. Despite parylene compatibility, it has been necessary to coat this material with fibronectin to increase cell adhesion.

Transmembrane cell migration and inter-layer coupling

Myocyte–nonmyocytes can couple in 3 structural configurations – (1) zero-sided connection: nonmyocytes inserted

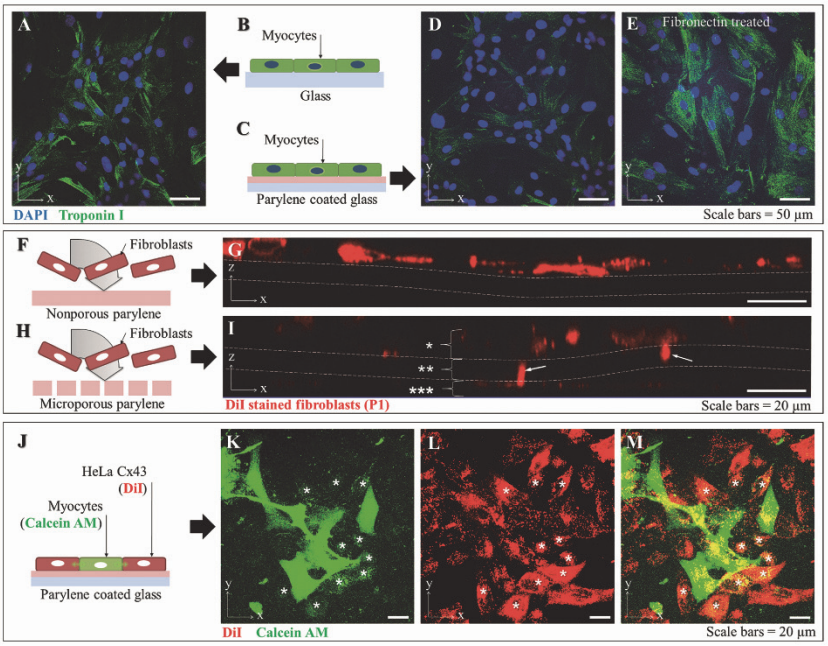

Fig. 4 Myocyte–nonmyocyte: cultures, migration and coupling. (A–E) Myocytes isolated from neonatal rat ventricles, plated on (A) glass coverslip (D) parylene and (E) parylene treated with fibronectin. Myocytes were identified by troponin I (in green) and their respective nuclei stained with DAPI (in blue). Myocytes plated on fibronectin coated parylene are much more spread out compared to those plated on untreated parylene or glass. (F–I) Fibroblast migration in Ø3–3.5 μm microporous parylene membranes. Fibroblasts were plated on one side of the microporous parylene membranes and fixed after 10 hours. Cross-sectional views are shown. (G) Monolayer of fibroblasts formed on nonporous region. (I) Migrated cells forming a fibroblast bilayer in microporous region. The cells were plated on the top layer (*). The cells seen in the bottom layer (***) migrated through the pores (arrows) of the parylene membrane (**). Dashed thin double parallel lines in G and I indicate the position of the parylene membrane. (J–M) Metabolic coupling between myocytes and HeLaCx43 cells. (J) The experimental setup for co-plating the myocytes and HeLaCx43. HeLaCx43 cells were labelled with DiI (red) and myocytes with Calcein AM (green). Note that the labelling includes many intracellular vesicular membranes. (K) Myocytes and coupled HeLaCx43 cells with Calcein. The bright green myocytes are loaded with Calcein AM, and the light green cells (indicated by an asterisk) are HeLaCx43 (compare with L) that have received Calcein by diffusion through gap junction channels. (M) Micrograph enhancing the presence of both dyes. (Note: brightness and contrast was enhanced in K–L by the same amount.)

longitudinally in between myocytes as obstacles, (2) single-sided connections: one or more nonmyocytes are laterally coupled to a single myocytes, and (3) double-sided connection: interconnected nonmyocytes connect myocytes along short or long distances.[61] There are a number of experimental cell culture models for studying myocyte–nonmyocyte coupling, but only few give importance to coupling configuration.[13,17,27–30] Structurally, nonmyocytes have been more often observed to be arranged in a lateral manner in healthy and pathological cardiac tissues *in vivo*.[62] Therefore, a laterally coupled myocyte–nonmyocyte *in vitro* model will serve as more architecturally accurate against current *in vitro* models. In our bilayer model, significant nonmyocyte migration to myocyte layer would impair the tissue architecture and coupling configuration.

To optimize the final pore size for the PerFlexMEA, inter-layer migration experiments were conducted with microporous parylene membranes of average pore diameters 3–3.5 μm, 5–6 μm and 7–7.5 μm. Bilayers were created of myocytes and fibroblasts (as nonmyocytes) isolated from neonatal rat ventricles across the microporous parylene membranes of the three different pore sizes. While myocytes remained in their layer, fibroblasts were identified on both sides of all three sets of microporous membranes. To specifically study fibroblast migration in the smallest available pore size, DiI stained fibroblasts were plated on only one side of the Ø3–3.5 μm microporous parylene membrane and fixed after 10 hour. Nonporous and porous region of the membranes were imaged. The imaging results show that a monolayer is formed (Fig. 4G) in the nonporous region (controls). This is not the case in the porous region where we can clearly identify two cell layers (Fig. 4I) indicating fibroblast migration. Nonmyocyte migration across the membrane hampers the bilayer architecture and the desired control over inter-

layer coupling is lost. While this migration can be prevented using drugs that affect the formation of cytoskeleton, instead we decided to use non-excitable HeLa cells, transfected with connexin43 (HeLaCx43).[58] Connexin 43 channels are also expressed in myocytes and when plated bordering with HeLaCx43 cells, they form hetero–cellular gap junctions, resulting in intercellular communication between these two cell types.[63] Fig. 4J–M shows such dye coupling experiment where the HeLaCx43 cells were labelled with DiI (in red) and myocytes were labelled with Calcein AM (bright green). After 10 hours co-culture, Calcein from the myocytes diffused into the adjoining HeLaCx43 cells (cells labelled * in Fig. 4K–M), indicating dye coupling between cells. The formation of gap junction channels allows for metabolic coupling where low molecular weight metabolites like nucleotides and amino acids, can be transported amongst the cells through the gap junction channels. Calcein AM in its initial form is non-fluorescent and cell membrane permeable. Once it enters a cell cytoplasm, it reacts with intracellular esterases to form a cell membrane impermeable fluorescent molecule. As per our experimental protocol the most probable way for the DiI stained HeLaCx43 cells to get the fluorescent membrane impermeable Calcein molecules is through direct inter-cellular coupling provided by gap junction channels. This type of intercellular coupling experiment using Calcein AM dye has been used previously for demonstrating myocyte–nonmyocyte coupling.[11]

To characterize the amount of coupling through the pores of the parylene membrane, a bilayer of HeLaCx43 cells with the above-discussed dual dye system was used (Calcein AM stained cells plated on one side and the DiI stained on the other). The results from one such experiment are shown in Fig. 5. Cross-sectional views of the preparations (Fig. 5B, D, F–H) clearly show distinct layers of green and red stained cells. Fig. 5A, C and E show top views of the top cell layer, the parylene membrane and the bottom cell layer, respectively. While the top cell layer is bright green, the bottom layer is mostly red with a sparser intracellular green (Fig. 5E) indicating green dye (Calcein) transfer from top. Also, the parylene membrane slice (Fig. 5C) shows almost all pores fluorescing green and red. Furthermore, cross-sectional views at different membrane pore sections (Fig. 5F–H) show green fluorescence inside pores connecting the two cell layers. This confirms fluent and controlled inter-layer cell coupling. Also, no red stained cells were observed on the Calcein AM stained side of cells confirming no or minimum transmembrane migration through the micropores.

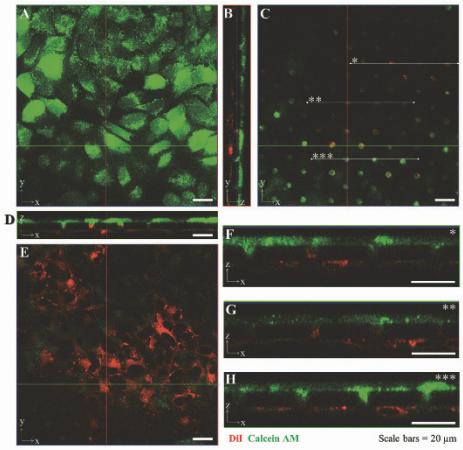

Fig. 5 Inter-layer coupling and migration studies in HeLaCx43 bilayer. Confocal images showing inter-layer coupling without transmembrane migration of HeLaCx43 cells plated on either side of Ø5–6 μm microporous parylene membrane. (A–D) Confocal images from top (A, C and E) and cross-sectional (B and D) views of different layers of the preparation. (A) Top layer: top view of Calcein AM (green) stained HeLaCx43 cells. (C) Mid layer: image slice in the microporous parylene membrane. The bright round regions (green and red) are due to inter-layer coupling through micropores. (E) Bottom layer: DiI stained (red) HeLaCx43 cells with Calcein (sparser green) received from top layer. (F, G and H) Cross-sectional views of respective sections at the white lines indicated by asterisks in panel (C).

Electrophysiological recording

The PerFlexMEAs were able to record field potentials from myocytes, though the number of electrodes showing spikes depended on the quality of the culture. Fig. 6A shows one such recording where spikes can be identified in 18 (out of 20) of the microelectrodes. For microelectrodes without spikes, the average of the activation times of its adjacent neighbours was considered for conduction velocity calculation (signal frames [5,3] and [5,4] in the bottom right corner of measured field potentials Fig. 6A). The signal quality varied with a maximum peak-to-peak voltage of 433 μV with a signal-to-noise-ratio of close to 7. The more uniform and well adhered the myocyte culture is with the parylene membrane, the better we expect the recording quality.

Conduction velocity. Conduction velocity was calculated from every set of spikes recorded from a preparation for their respective days. Local conduction velocity vectors were calculated based on the activation times (Fig. 6B). The magnitudes of the velocity vectors were averaged to get the average conduction velocity of the specific experimental condition. These values were considered for comparing the effect of nonmyocyte-coupling on conduction velocity (Fig. 7).

It has been previously shown that the interaction between excitable myocytes and non-excitable fibroblast can induce changes in current flows responsible for the spread of action potentials in the tissue. This is where the PerFlexMEA can become an essential tool in *in vitro* cardiac tissue studies, since besides metabolic interactions, we are also interested in studying the effects of hetero-cellular interactions in the excitability of cardiac cells. Studies of this kind can yield *in vitro* information that later can be traduced into drug treatment improvement for humans.[64]

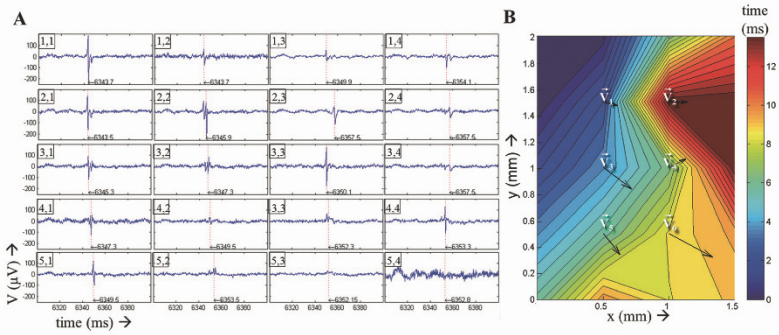

Fig. 6 Field potential measurements and conduction velocity calculation. (A) Field potential measurements from 4 × 5 electrodes, arranged in order of actual electrode array in the PerFlexMEA. The red dotted line is the time of maximum derivative of the field potential signal at its respective microelectrodes. (B) Isochronal map generated based on the times of maxima. The velocity vectors were calculated based on the neighbouring field potential times and the electrode array pitch (500 μm).

Our first set of results are presented in Fig. 6, where field potentials recorded from rat neonatal myocytes plated on the MEA side of the PerFlexMEA were used in determining the conduction velocity (CV) in control conditions, and after nonmyocytes cells are plated at the opposite side of the PerFlexMEA. Based on the identified instances of maximum signal derivative of the field potential spikes (dotted red lines in each microelectrode signal frame Fig. 6A), a local isochronal map was generated (Fig. 6B). The local conduction velocity vectors (black arrows in Fig. 6B) indicate the direction of conduction.

Effects of myocyte-HeLaCx43 inter-layer coupling on conduction velocity. Fig. 7 summarizes conduction velocity results extracted from the recording experiments done using 4 PerFlexMEAs: two were set as control devices (in blue), and the other two were plated with HeLaCx43 after day 5 (in red). Magnitude of conduction velocity vectors from the respective pair of devices were averaged together to calculate the average conduction velocity for each condition on each day. The n value represent the number of spike sets (Fig. 6A shows a spike set) considered and k represents the total number of velocity vectors (to in Fig. 6B). Since, each set of spikes gives 6 velocity vectors, k values are always less than or equal to 6 times n. The number of spikes recorded varies from preparation to preparation. Since, the preparations were self-stimulated by random pacemaker cells, the beat rates varied for each preparation. In our case, the cell preparations in the control preparations had a much lower beat rate, than the ones on which HeLaCx43 were plated.

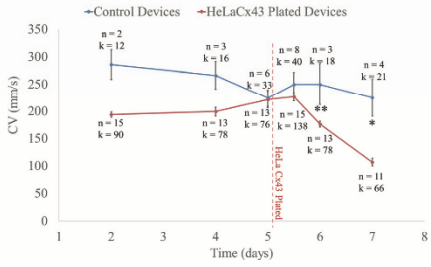

Fig. 7 Effects of transmembrane myocytes–nonmyocyte coupling. Transmembrane plating of HeLaCx43 cells reduces myocyte conduction velocity after day 5. Conduction velocities (CV) were calculated for each spike recorded during electrophysiological experiments using 4 PerFlexMEAs (2 as controls and 2 with HeLaCx43 plated after day 5). n is the number of recorded spikes for each experiment and k is the number of velocity vectors. While in control cultures, conduction velocity remains somewhat constant during the 7 days in culture, conduction velocity after HeLaCx43 cells were plated, steadily declines on day 6 and 7. The difference is significant on day 6 (**$p < 0.05$) and 7 (*$p < 0.01$).

As shown in Fig. 7, under control conditions (Myocytes plated on the MEA side), conduction velocity was calculated to be between 200 and 350 mm s^{-1} with a slight decreasing tendency during the following 7 recording days. After HeLaCx43 cells were added on day 5 (after myocyte-plating), conduction velocity in the myocyte layer a decreased on day 6 and 7. The difference in conduction velocity between the control and HeLaCx43 coupled cultures becomes significant on day 6 (**$p < 0.05$) and day 7 (*$p < 0.01$). On day 7 (2 days after HeLaCx43 plating) the conduction average velocity reduces to almost half the starting value.

Computational models of myocyte–nonmyocyte have demonstrated that conduction in myocytes reduces and ultimately fails with increased lateral myocyte–nonmyocyte coupling.[23,24] Our experimental model does parallel those results, though we have only tested a single value of pore pitch (pore-pitch being associated to myocyte–nonmyocyte coupling ratio). Variations on pore pitches corresponding to myocyte–nonmyocyte ratios will be fabricated for validating these computational model results.

Cardiac fibroblasts are known to produce and secrete signaling molecules that effect the expressions and functioning of ion channels[65] and gap junctions[66] in neonatal rat myocytes. Furthermore, fibroblasts have also been reported to reduce conduction velocity and increase action potential duration in myocytes through such paracrine interactions.[67] While we did not find similar studies involving HeLa cells, paracrine interactions with HEK-293 cells (another immortalized cell line) have been reported to have negligible effect on myocyte conduction velocity and action potential duration.[67] Hence, a major amount of reduction in conduction velocity of myocytes that was observed in our experiments was probably due to direct intercellular coupling of myocytes with HeLaCx43 cells. Membranes from directly coupled HeLaCx43 cells act as current sinks which slow down myocyte activation, resulting in slower conduction.

Conclusions

Our results confirm that functional interactions between cells layers can be achieved across a microporous membrane of Ø3–3.5 μm pores. This functional communication can be metabolic and most importantly, electrical. Our trials of creating microfeatures on different materials and methods demonstrate the potential of parylene as an alternative to the commercially available cell culture microporous membranes. We also show the need of determining pore sizes, specific for each cell type, as they do have different migration rates. Our results also indicate that the PerFlexMEA is a device expected to allow studying the effects of controlled inter-layer communication bilayer tissue constructs on electrical signal conduction and metabolic homeostasis, including direct communication through gap junctions, and/or paracrine communication through extracellular media.

Acknowledgements

This work was funded by the Nora Eccles Treadwell Foundation (APM). The authors thank Chris Hunter at the CVRTI Core Facility for his help in cell isolation and culture protocols, and the Nanofab personnel at the University of Utah for their help and support during the fabrication of all devices. The authors also thank Dr. Florian Solzbacher and Dr. Sandeep Negi for sharing their impedance measurement resources.

Notes and references

1 Center for Disease Control and Prevention, www.cdc.gov.
2 S. S. Chugh, K. Reinier, C. Teodorescu, A. Evanado, E. Kehr, M. Al Samara, R. Mariani, K. Gunson and J. Jui, *Prog. Cardiovasc. Dis.*, 2008, **51**, 213–228.
3 D. P. Zipes and H. J. Wellens, *Circulation*, 1998, **98**, 2334–2351.
4 R. J. Myerburg, A. Interian, R. M. Mitrani, K. M. Kessler and A. Castellanos, *Am. J. Cardiol.*, 1997, **80**, 10F–19F.
5 B. Burstein and S. Nattel, *J. Am. Coll. Cardiol.*, 2008, **51**, 802–809.
6 K. T. Weber, *Curr. Opin. Cardiol.*, 2000, **15**, 264–272.
7 P. Camelliti, C. R. Green, I. LeGrice and P. Kohl, *Circ. Res.*, 2004, **94**, 828–835.
8 A. M. De Mazière, A. C. Van Ginneken, R. Wilders, H. J. Jongsma and L. N. Bouman, *J. Mol. Cell. Cardiol.*, 1992, **24**, 567–578.
9 K. Goshima, *Exp. Cell Res.*, 1970, **63**, 124–130.
10 G. Gaudesius, M. Miragoli, S. P. Thomas and S. Rohr, *Circ. Res.*, 2003, **93**, 421–428.
11 L. Chilton, W. R. Giles and G. L. Smith, *J. Physiol.*, 2007, **583**, 225–236.
12 W. A. LaFramboise, D. Scalise, P. Stoodley, S. R. Graner, R. D. Guthrie, J. A. Magovern and M. J. Becich, *Am. J. Physiol.*, 2007, **292**, C1799–1808.
13 S. S. A. Thompson, C. R. Copeland, D. H. D. Reich and L. Tung, *Circulation*, 2011, **123**, 2083–2093.
14 M. B. Rook, H. J. Jongsma, B. Jonge and B. De Jonge, *Pflugers Arch. Eur. J. Physiol.*, 1989, **414**, 95–98.
15 M. B. Rook, A. C. Van Ginneken, B. De Jonge, A. El Aoumari, D. Gros and H. J. Jongsma, *Am. J. Physiol.*, 1992, **263**, 959–977.
16 M. Miragoli, G. Gaudesius and S. Rohr, *Circ. Res.*, 2006, **98**, 801–810.
17 S. Zlochiver, V. Muñoz, K. L. Vikstrom, S. M. Taffet, O. Berenfeld and J. Jalife, *Biophys. J.*, 2008, **95**, 4469–4480.
18 M. Miragoli, N. Salvarani and S. Rohr, *Circ. Res.*, 2007, **101**, 755–758.
19 J. P. Fahrenbach, R. Mejia-Alvarez and K. Banach, *J. Physiol.*, 2007, **585**, 565–578.
20 K. Goshima, *Exp. Cell Res.*, 1969, **58**, 420–426.
21 T. A. T. Baudino, A. McFadden, C. Fix, J. Hastings, R. Price and T. K. Borg, *Microsc. Microanal.*, 2008, **14**, 117–125.
22 B. R. Desroches, P. Zhang, B.-R. Choi, M. E. King, A. E. Maldonado, W. Li, A. Rago, G. Liu, N. Nath, K. M. Hartmann, B. Yang, G. Koren, J. R. Morgan and U. Mende, *Am. J. Physiol.*, 2012, **302**, H2031–2042.
23 F. B. Sachse, A. P. Moreno, G. Seemann and J. A. Abildskov, *Ann. Biomed. Eng.*, 2009, **37**, 874–889.
24 Y. Xie, A. Garfinkel, P. Camelliti, P. Kohl, J. Weiss and Z. Qu, *Heart Rhythm*, 2009, **6**, 1641–1649.
25 V. Jacquemet and C. Henriquez, *Am. J. Physiol.*, 2008, **1**, 1–26.
26 M. M. Maleckar, J. L. Greenstein, W. R. Giles and N. A. Trayanova, *Biophys. J.*, 2009, **97**, 2179–2190.
27 M. Q. Chen, J. Wong, E. Kuhl, L. Giovangrandi and G. T. A. Kovacs, *Comput. Methods Biomech. Biomed. Engin.*, 2013, **16**, 185–197.
28 S. Roy, M. Q. Chen, G. T. A. Kovacs and L. Giovangrandi, *Conf. Proc. IEEE Eng. Med. Biol. Soc.*, 2009, **2009**, 4250–4253.
29 Y. Feld, *Circulation*, 2002, **105**, 522–529.
30 C. Vasquez, P. Mohandas, K. L. Louie, N. Benamer, A. C. Bapat and G. E. Morley, *Circ. Res.*, 2010, **107**, 1011–1020.
31 P. Camelliti, A. D. McCulloch and P. Kohl, *Microsc. Microanal.*, 2005, **11**, 249–259.
32 S. M. Gopalan, C. Flaim, S. N. Bhatia, M. Hoshijima, R. Knoell, K. R. Chien, J. H. Omens and A. D. McCulloch, *Biotechnol. Bioeng.*, 2003, **81**, 578–587.

33 S. Rohr, D. Scholly and G. Kleber, *Circ. Res.*, 1991, **68**, 114–130.
34 M. A. Birch, M. Tanaka, G. Kirmizidis, S. Yamamoto and M. Shimomura, *Tissue Eng., Part A*, 2013, **19**, 2087–2096.
35 R. Booth and H. Kim, *Lab Chip*, 2012, **12**, 1784–1792.
36 H. Kaji, T. Ishibashi, K. Nagamine, M. Kanzaki and M. Nishizawa, *Biomaterials*, 2010, **31**, 6981–6986.
37 B. D. Lawrence, J. K. Marchant, M. A. Pindrus, F. G. Omenetto and D. L. Kaplan, *Biomaterials*, 2009, **30**, 1299–1308.
38 J. Shao, L. Wu, J. Wu, Y. Zheng, H. Zhao, X. Lou, Q. Jin and J. Zhao, *Biomed. Microdevices*, 2010, **12**, 81–88.
39 G. Shayan, N. Felix, Y. Cho, M. Chatzichristidi, M. L. Shuler, C. K. Ober and K. H. Lee, *Tissue Eng., Part C*, 2012, **18**, 667–676.
40 Corning Inc., www.corning.com/lifesciences.
41 B. E. Isakson and B. R. Duling, *Circ. Res.*, 2005, **97**, 44–51.
42 G. S. Goldberg, A. P. Moreno and P. D. Lampe, *J. Biol. Chem.*, 2002, **277**, 36725–36730.
43 A. Mohr, W. Finger, K. J. Fohr, W. Gopel, H. Hammerle and W. Nisch, *Sens. Actuators, B*, 1996, **34**, 265–269.
44 L. Berdondini, P. D. van der Wal, O. Guenat, N. F. de Rooij, M. Koudelka-Hep, P. Seitz, R. Kaufmann, P. Metzler, N. Blanc and S. Rohr, *Biosens. Bioelectron.*, 2005, **21**, 167–174.
45 M. Reppel, F. Pillekamp, Z. J. Lu, M. Halbach, K. Brockmeier, B. K. Fleischmann and J. Hescheler, *J. Electrocardiol.*, 2004, **37**, 104–109.
46 L. Giovangrandi, K. H. Gilchrist, R. H. Whittington and G. T. A. Kovacs, *Sens. Actuators, B*, 2006, **113**, 545–554.
47 P. Thiébaud, N. F. de Rooij, M. Koudelka-Hep and L. Stoppini, *IEEE Trans. Biomed. Eng.*, 1997, **44**, 1159–1163.
48 P. Thiébaud, C. Beuret, M. Koudelka-Hep, M. Bove, S. Martinoia, M. Grattarola, H. Jahnsen, R. Rebaudo, M. Balestrino, J. Zimmer and Y. Dupont, *Biosens. Bioelectron.*, 1999, **14**, 61–65.
49 U. Egert, S. Okujeni and W. Nisch, in *Mikrosystemtechnik Kongress*, VDE VERLAG GMBH, Freiburg, 2005, pp. 431–434.
50 S. A. Boppart, B. C. Wheeler and C. S. Wallace, *IEEE Trans. Biomed. Eng.*, 1992, **39**, 37–42.
51 C. González and M. Rodríguez, *J. Neurosci. Methods*, 1997, **72**, 189–195.
52 B. A. Hollenberg, C. D. Richards, R. Richards, D. F. Bahr and D. M. Rector, *J. Neurosci. Methods*, 2006, **153**, 147–153.
53 D. P. O'Brien, T. R. Nichols and M. G. Allen, in *14th IEEE International Conference on Micro Electro Mechanical Systems*, IEEE, Interlaken, 2001, pp. 216–219.
54 P. J. Rousche, D. S. Pellinen, D. P. Pivin, J. C. Williams, R. J. Vetter and D. R. Kipke, *IEEE Trans. Biomed. Eng.*, 2001, **48**, 361–371.
55 J.-M. Hsu, L. Rieth, R. A. Normann, P. Tathireddy and F. Solzbacher, *IEEE Trans. Biomed. Eng.*, 2009, **56**, 23–29.
56 G. E. Loeb, M. J. Bak, M. Salcman and E. M. Schmidt, *IEEE Trans. Biomed. Eng.*, 1977, **24**, 121–128.
57 D. Rodger, A. Fong, W. Li, H. Ameri, A. Ahuja, C. Gutierrez, I. Lavrov, H. Zhong, P. Menon and E. Meng, *Sens. Actuators, B*, 2008, **132**, 449–460.
58 S. Elenes, A. D. Martinez, M. Delmar, E. C. Beyer and A. P. Moreno, *Biophys. J.*, 2001, **81**, 1406–1418.
59 C. Metallo, R. D. White and B. A. Trimmer, *J. Neurosci. Methods*, 2011, **195**, 176–184.
60 M. M. Falk, *J. Cell Sci.*, 2000, **113**, 4109–4120.
61 P. Kohl and P. Camelliti, *Heart Rhythm*, 2007, **4**, 233–235.
62 P. Camelliti, T. K. Borg and P. Kohl, *Cardiovasc. Res.*, 2005, **65**, 40–51.
63 T. C. Clarke, D. Thomas, J. S. Petersen, W. H. Evans and P. E. M. Martin, *Br. J. Pharmacol.*, 2006, **147**, 486–495.
64 M. Riedel, C. J. Jou, S. Lai, R. L. Lux, A. P. Moreno, K. W. Spitzer, E. Christians, M. Tristani-Firouzi and I. J. Benjamin, *Stem Cell Rep.*, 2014, **3**, 131–141.
65 P.-L. Merle, J.-J. Feige and J. Verdetti, *J. Biol. Chem.*, 1995, **270**, 17361–17367.
66 B. W. Doble, Y. Chen, D. G. Bosc, D. W. Litchfield and E. Kardami, *Circ. Res.*, 1996, **79**, 647–658.
67 D. M. Pedrotty, R. Y. Klinger, R. D. Kirkton and N. Bursac, *Cardiovasc. Res.*, 2009, **83**, 688–697.

CHAPTER 3

COMPUTATIONAL SIMULATIONS OF ASYMMTERIC FLUXES OF LARGE MOLECULES THROUGH GAP JUNCTION CHANNEL PORES

Reprinted from Computational simulations of asymmetric fluxes of large molecules through gap junction channel pores. *J. Theor. Biol.* 2017, 412, 61–73. Mondal A, Appadurai DA, Akoum NW, Sachse FB, Moreno AP, with permission from Elsevier.

Journal of Theoretical Biology 412 (2017) 61–73

Contents lists available at ScienceDirect

Journal of Theoretical Biology

journal homepage: www.elsevier.com/locate/yjtbi

Computational simulations of asymmetric fluxes of large molecules through gap junction channel pores

Abhijit Mondal[a,b,*], Daniel A. Appadurai[c], Nazem W. Akoum[d], Frank B. Sachse[a,b], Alonso P. Moreno[a,b,*]

[a] Department of Bioengineering, University of Utah, USA
[b] Nora Eccles Harrison Cardiovascular Research and Training Institute, University of Utah, USA
[c] Department of Biology, University of Utah, USA
[d] Department of Cardiology, University of Washington, USA

ARTICLE INFO

Keywords:
Gap junctions
Connexins
Heterotypic
Asymmetric flux
Computational model
Brownian dynamics simulation

ABSTRACT

Gap junction channels are formed out of connexin isoforms, which enable molecule and ion selective diffusion amongst neighboring cells. HeLa cells expressing distinct connexins (Cx) allow the formation of heterotypic channels, where we observed a molecular charge-independent preferential flux of large fluorescent molecules in the Cx45 to Cx43 direction. We hypothesize that the pore's shape is a significant factor along-side charge and transjunctional voltages for this asymmetric flux. To test this hypothesis, we developed a 3D computational model simulating Brownian diffusion of large molecules in a gap junction channel pore. The basic pore contour was derived from x-ray crystallographic structures of Cx43 and Cx26 and approximated using basic geometric shapes. Lucifer yellow dye molecules and cesium counter-ions were modeled as spheres using their respective Stokes radii. Our simulation results from simple diffusion and constant concentration gradient experiments showed that only charged particles yield asymmetric fluxes in heterotypic pores. While increasing the inner mouth size resulted in a near-quadratic rise in flux, the rise was asymptotic for outer mouth radii increase. Probability maps and average force per particle per pore section explain the asymmetric flux with variation in pore shape. Furthermore, the simulation results are in agreement with our *in vitro* experimental results with HeLa cells in Cx43-Cx45 heterotypic configurations. The presence of asymmetric fluxes can help us to understand effects of the molecular structure of the pore and predict potential differences *in vivo*.

1. Introduction

Gap junction channels play an important role in intercellular communication as they allow for passage of ions and small molecules, permitting metabolic coupling in several tissues. The physiological relevance of metabolic coupling comes mainly from the discovery of mammalian diseases associated with connexin mutations affecting gap junction channel permeability (Harris, 2007). Studies from multiple laboratories have provided convincing evidence that the expression of distinct connexins in a gap junction induces difference of permeation rates for ions and large fluorescent molecules (Beyer et al., 2001; Bukauskas et al., 2006; Eckert, 2006; Goldberg et al., 2002; Harris, 2007; Martínez et al., 2002; Rackauskas et al., 2007b; Veenstra et al., 1994). Permeability to large molecules is generally linked to highly conductive channels, although charge selectivity leads to a variety of permselectivity associated properties currently under study (Eckert, 2006; Harris, 2008, 2007; Heyman and Burt, 2008; Kanaporis et al., 2013; Rackauskas et al., 2007b; Veenstra, 2001; Weber et al., 2004). These properties are thought to be based on the connexin isoform delineating the pore either in its homomeric or heteromeric configuration.

Our previous experimental studies strongly suggest that molecular fluxes through hetero-multimeric channels formed out of connexin 43 (Cx43) and connexin 45 (Cx45) are smaller than in their homomeric counterparts (Martínez et al., 2002; Moreno et al., 2004) and depend on the direction of concentration gradients established across the gap junction. In additional studies presented here, we show that flux asymmetry also exists with heterotypic channels formed out of Cx43 and Cx45. We obtained these asymmetric flux data from iontophoretic injections and dual whole cell voltage clamp experiments. Since these findings were similar when we injected particles of similar size but different charge, we inferred that the asymmetric flux direction was related more to the shape of the pore and not to the particle electric polarity (Mondal et al., 2009; Mondal and Moreno, 2010).

* Corresponding authors at: Nora Eccles Cardiovascular and Research Training Institute (CVRTI), University of Utah, 95 South 2000 East, Room 143, Salt Lake City, UT 84112, USA.
E-mail addresses: abhijit.mondal@utah.edu (A. Mondal), alonso.moreno@utah.edu (A.P. Moreno).

http://dx.doi.org/10.1016/j.jtbi.2016.08.040
Received 7 August 2015; Received in revised form 30 June 2016; Accepted 30 August 2016
Available online 31 August 2016

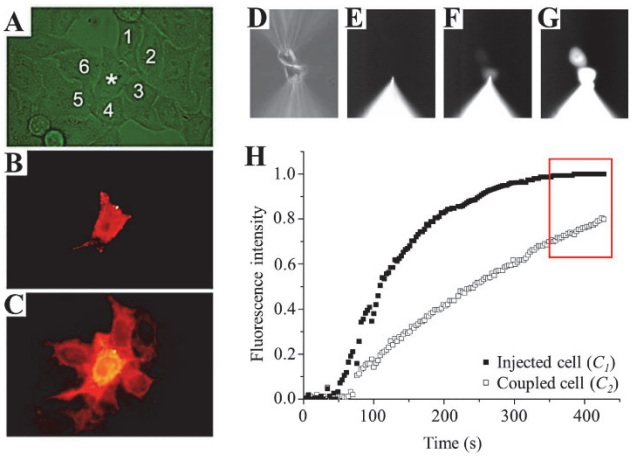

Fig. 1. *In vitro* experiments with large dye molecules through gap junction channels expressed in HeLa cells. (A-C) Dye coupling through micropipette iontophoretic injection. (A) Phase contrast micrograph showing the cell to be injected (*) in physical contact with 6 other cells. (B) Fluorescent DiI marks the cell to be injected. (C) After 3 min, injected Rhodamine123 diffuses into five of the surrounding cells. (D-H) Double whole cell voltage clamp experiment. (D-G) Series of micrographs during the diffusion of LY across two cells under double whole cell voltage clamp. (H) Fluorescence intensities recorded from each cell during the recording of junctional conductance. As the LY intensity of the cell attached to the electrode (■) loaded with LY reaches a steady state (red box), the change in brightness during a few seconds is recorded in the coupled cell (□). The flux is calculated using the slope of this line in the red box region. (For interpretation of the references to color in this figure legend, the reader is referred to the web version of this article.)

This asymmetry in flux directionality appears to occur only when large charged molecules like Lucifer Yellow (LY) are involved. We have previously demonstrated that Cx43 and Cx45 heterotypic channels do not rectify to electrical current (Elenes et al., 2001), indicating that the asymmetric flux for small ions is hardly detectable, if present. These data-findings lead us to hypothesize that for large molecules the shape of the channel pore could represent the structural basis of the mechanisms involved. Robinson et al. (1993) had already observed these asymmetric fluxes and labeled them preferred directional fluxes while studying LY and Biotin diffusion between astrocytes and oligodendrocytes in the central nervous system. They revealed a preferential flux of LY and Biotin from astrocytes to oligodendrocytes. At that time, they postulated the gap junction channel to be conical in shape as the basis for the mechanism to explain their data. Their explanation on how this phenomenon occurred was based on the assumption that steady state could be reached maintaining a difference in concentration between the injected cell and the recipient cell. This explanation was criticized since their argument required an active mechanism to maintain a difference in concentration, regardless of pore shape (Finkelstein, 1994). Moreover, at the lower limit in concentration no preferential flux should be expected. Although at high concentrations a flux asymmetry may be occurring, according to our model and our more recent experiments, this only happens when particles are charged and/or when an electrical voltage is present across the junction. Since we observed similar asymmetric fluxes in cells expressing different connexins, we considered the possibility of the preferred flux direction being dependent on heterotypic channel pore's shape differences.

To test our hypothesis, we developed a computational model based on a simplified version of existing Brownian dynamics model (Ermak and McCammon, 1978) and studied differences in the gap junction channel's pore shapes. Brownian dynamics enables creating models with long time intervals by considering water as a continuum, ions or particles of interest as point particles and the protein channel walls as smooth surfaces (Cooper et al., 1985). It is suitable at membrane channel scale (~nanometer) where continuum dynamics tend to fail (Corry et al., 2000). Brownian dynamics have been widely used for the modeling of various biological channels like potassium channels (Allen et al., 1999; Chung et al., 2002), sodium channel (Vora et al., 2008), calcium channels (Corry et al., 2001), porins (Im and Roux, 2002; Schirmer and Phale, 1999) and mitochondrial porin (Lee et al., 2011). Significant work has been done addressing issues associated with calculating effective forces (Allen et al., 2004) and inhomogeneity of diffusion constant (Mamonov et al., 2006) and dielectric medium (Corry et al., 2000; Graf et al., 2004) in ions channel models. Since gap junction channel pores (radii ranging from ~6 Å to 25 Å) are larger than ion channels (radii ranging from ~1 Å to ~10 Å) and limited gap junction structural details are available, we assumed the diffusivity and dielectric of the medium in the pore to be homogeneous. In our simulations we modeled only LY particles and cesium ions (Cs) as counter-ions. Since very limited or no information was available about the structures of Cx43 and Cx45, we modeled the pore surface to be uncharged. The initial pore-shape was based on the molecular structure obtained by x-ray crystallography of Cx26 and Cx43 (Maeda et al., 2009; Unger et al., 1999). The crystallographic structures of both pores showed a transmembrane protein homology and had a similar central vestibule with different shaped mouths, which could be typical of gap junctions formed by other connexin types. We approximated the pore shape using geometrical shapes and at the ends we added ellipsoids representing controlled volumes (or reservoirs) in the adjacent cells. We used spheres with equivalent Stokes radius of 4.9 Å (Heyman and Burt, 2008) to represent LY particles. Cs ions were selected as counter-ions and also modeled as spheres using it's Stokes radius of 1.79 Å (Pau et al., 1990). We determined the flux by counting the particles that crossed the channel's pore during a concentration gradient clamp established across the pore.

The simulation results strongly suggest that our experimental data, and those published by Robinson et al. (Robinson et al., 1993) can be explained by a temporal asymmetric flux, only present during concentration and/or voltage gradients across the junction. The asymmetric flux in our simulations is also only maintained as long as the particles are charged. Simulations also demonstrate that removal of particle charge, abolishes the asymmetric flux in experiments with constant concentration gradient as well as simple diffusion.

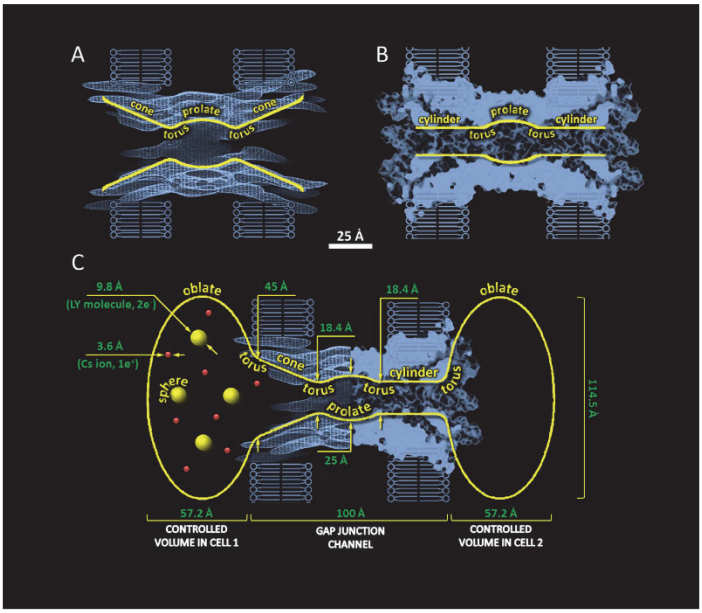

Fig. 2. Pore model contour approximation from published structures. (A) Cx43 tailless x-ray crystallography model (Unger et al., 1999) with a longitudinal section of the geometrical model superimposed. The outer and inner diameters correspond to the shape of the inner and outer mouths of the pore. (B) Cx26 molecular prediction (Maeda et al., 2009) with superimposed geometrical model. (C) Representation of a hypothesized heterotypic pore with conical and cylindrical mouths. LY molecules and Cs ions were modeled as spheres with radii of 4.9 Å and 1.79 Å, respectively.

2. Methods

2.1. In vitro *experiments*

2.1.1. *Dye coupling through micropipette iontophoretic injections*

Lucifer Yellow (LY, molecular weight (mw) 443, particle charge (z) = 2e ; 5 mM; Sigma Aldrich, cat #67769-47-5), Rhodamine123 (R123, mw 380.83, z = $2e^+$; 2.5 mM; Sigma Aldrich, cat #62669-70-9) and Neurobiotin (NB, mw 367, z = $1e^+$; 5 mM; Vector Laboratories, cat#SP-1120) were injected iontophoretically into a single DiI (Molecular Probes, cat #D282) pre-stained cell (Fig. 1B) on a cell monolayer for 5-10 s after diluting them in 150 mM lithium chloride solution. Dye injections were performed using a 50 MΩ glass micropipette connected to a MPI amplifier (Model MPI 707) and driven by a Grass S9 stimulator at 3 Hz. LY and R123 were detected under UV fluorescence using an inverted microscope (Nikon Eclipse TE 2000-U). NB was detected by fixing the culture with alcohol 3 minutes after injection and using an HR-linked antibody (Elite PK 6100 Vectastain ABC kit; Vector Laboratories).

The coupling coefficient for each injection was calculated as the ratio of the number of surrounding cells (cells labelled 1 to 6 in Fig. 1A) that received the dye (Fig. 1C) over the total number of cells in contact with the injected cell (cell labelled '*' in Fig. 1A).

2.1.2. *Double whole cell voltage clamp*

The double whole cell voltage clamp technique has been previously described (del Corsso et al., 2006). In short, micropipettes loaded with a Cs based salt (Patch Cesium (Pcs): 120 mM CsCl, 0.5 mM CaCl, 5 mM EGTA, 10 mM Hepes, pH 7.1) were used in each cell of a pair of HeLa cells expressing either Cx43 or Cx45. In heterotypic experiments, cells were pre-stained with either Green Cell Tracker CMFDA (Molecular Probes cat #C7025) or DiI (Molecular Probes, cat #D282) for quick identification. One of the micropipettes was loaded with 5 mM LY (Sigma Aldrich, cat #67769-47-5) and this pipette was always inserted in a cell stained with DiI (Fig. 1D). LY fluorescence was detected through a SnapCool CCD Camera (Photometrics, Tucson AZ), digitized and captured through an acquisition board and Imaging Workbench software (INDEC Biosystems, Santa Clara CA). Linearity was determined by imaging glass micro-slides (200 μm×20 μm) filled with different concentrations of LY (0.1 to 5 mM) in Pcs solution.

Junctional conductance was measured using 10 mV depolarizing pulses applied to the injected cell of a pair every second. In experiments without transjunctional voltage, junctional conductance was calculated every 3–5 min using only 3 hyperpolarizing pulses. Junctional flow was calculated from fluorescence images of the cells (Fig. 1E-G). Regions of interests where established around each cell of a pair, and the change in fluorescence was recorded simultaneously in each cell pair every 5 s. This fluorescent intensity was transformed to dye concentration (in mM) based on the linear calibration curve. In experiments where no transjunctional voltage was applied, the pipette not containing the dye was inserted into the opposing cell at the end of the dye injection part of the experiments for measuring the junctional conductance. This prevented further dilutions of the small amount of dye crossing into the opposing cell through dialysis generated by the second pipette along the whole experiment.

All fluxes into the second cell were obtained by calculating the change in concentration during 1 min as the first cell fluorescence approached the 70–80% of its maximum value (red boxed region in Fig. 1H). The change in concentration was divided by the estimated cell volume (0.75 pL) and the number of channels active in the junction at that time. The number of channels was estimated from the transjunctional current observed by the application of 10 mV/200 ms hyperpo-

larizing pulses.

2.2. Computational model design

The 3D computational model of a gap junction pore comprises four essential elements: the gap junction pore, dye and counter-ion particles, particle dynamics and intracellular environment and particle forces.

2.2.1. Gap junction pore

The spatial model of a heterotypic gap junction pore (Fig. 2C) was derived from reported structures of homotypic gap junction pores obtained from x-ray diffraction experiments (Maeda et al., 2009; Unger et al., 1999). Based on these structural data, we approximated the different pore sections with basic geometric shapes. Fig. 2A and B shows two such homotypic models, where both models consist of a central prolate ellipsoid as the pore's vestibule. While one model has two opposed cones as pore mouths (Fig. 2A), the other has two cylinders as pore mouths (Fig. 2B). At each end of the pore we placed oblate ellipsoids representing controlled intracellular volumes in the connected cells. The sizes of these intracellular volumes were calculated such that the system volume on either side of the pore center (center of the pore vestibule) was equal. We joined all the adjacent sections with curved surfaces, i.e. tori sections. We used the general 3D equations in Cartesian coordinates of an ellipsoid, torus and cone to create a mathematical model of the pore and restrict particles movement within the volume of the defined pore. The equations used for modeling the different pore section are presented in Table 1 (Rows 1–3). While the dimensions for the cone, cylinder and prolate ellipsoid were used from the x-ray diffraction results (Unger et al., 1999), the intermediate tori dimensions were computed to smoothly join the adjacent sections.

2.2.2. Particles: Dye and counter-ions

We modeled the permeant LY dye molecules and Cs counter-ions as spheres using the Stokes radius (4.9 Å and 1.79 Å, respectively), molecular weight (443 g-mol^{-1} and 132.9 g-mol^{-1}, respectively) and net charge (2e$^-$ and 1e$^+$, respectively) of the selected molecule (Heyman and Burt, 2008; Pau et al., 1990). Amongst all present counter-ions in the *in vitro* double voltage clamp experimental setup, Cs was one of the most prevalent ions and hence chosen as the counter-ion. Modeling the molecules as spheres simplified particle dynamics calculation as particle orientation was not required for collision detection.

2.2.3. Particle dynamics

Particle dynamics defines the equation governing particles' motion taking into consideration the environmental conditions. The Brownian dynamics model describes the particle movement using the following equation for particle position calculation (Ermak and McCammon, 1978; IIuber and Kim, 1996):

$$\mathbf{x}_{n+1} = \mathbf{x}_n - \frac{1}{kT}\mathrm{D}\mathbf{F}_{n+1}\Delta t + \sqrt{2\mathrm{D}}\,\Delta\mathbf{w}_{n+1} + \frac{\partial}{\partial x}\mathrm{D}\Delta t \tag{1}$$

where $\mathbf{x}$ is the particle position, n is the time index, k is the Boltzmann's constant, T is the temperature (in Kelvin), D is the diffusion constant, $\mathbf{F}$ is the net force acting on the particle, Δt is the time step, and $\Delta\mathbf{w}$ is a random vector from a 3D Gaussian distribution with zero mean and variance of Δt . Δt was selected such that $\Delta t >> m\mathrm{D}/kT$, where m is the molecular mass of the particle. Since we assumed diffusion coefficient to be constant throughout the cell-pore-cell system, the last term in Eq. (1) becomes zero.

In our model while particles were treated as spheres, particle-charges were treated as point charges placed at the center of the sphere. Inter-particle and particle-pore collisions were reflective, where at a given time particle-positions were recalculated if the particle was found in collision with another particle or the pore.

2.2.4. Intracellular environment and particle forces

The intracellular environmental parameters comprise the temperature T and the diffusion coefficient D accounting for the cytoplasm viscosity (η) and the particle size (r):

$$\mathrm{D} = \frac{kT}{6\pi r\eta} \tag{2}$$

Using Eq. 2 for LY and Cs ions, $\mathrm{D_{LY}}$ was calculated to be 4.6×10^{-10} m^2 s^{-1} and $\mathrm{D_{Cs}}$ was calculated to be 1.26×10^{-9} m^2 s^{-1}.

Sources of force on particles include the inter-particle electrostatic forces due to particle charge and in pore electric field produced by applied transjunctional voltage (Harris et al., 1981). These external sources contribute to the net force acting on each particle. Physical constraints to particle movement were introduced by modeling obstructions, changing pore shape or cell volume. In our simulations, forces due to particles' electrostatic charge were calculated using Coulomb's law:

$$\mathrm{F_Q} = \frac{q_1 q_2}{4\pi\varepsilon_r\varepsilon_0 r^2}\hat{r}_{12} \tag{3}$$

where ε_0 is the dielectric constant of vacuum, ε_r is the relative permittivity of the medium, r is the distance between the centers of two particles, $\hat{r}_{12}$ unit vector in the direction of force (parallel with the line from 1st particle to 2nd particle), and q_1 and q_2 are the charges on the 1st and 2nd particle, respectively.

In simulations with applied transjunctional voltage, the electrical field within cylindrical elements of the pore E was calculated at position x_i by:

$$E(x_i) = \frac{V R_{dx}(x_i)}{R_{gj}\,dx} \tag{4}$$

where V is the applied transjunctional voltage. $R_{dx}(x_i)$ is the resistance of the pore cylindrical element of radius $r(x_i)$ and constant width dx, calculated using the equation:

$$R_{dx}(x_i) = \rho_{cyto}\frac{dx}{\pi r(x_i)^2} \tag{5}$$

where ρ_{cyto} is the cytoplasmic resistivity (3.3 Ω m). R_{gj} is the total pore resistance calculated by summing up the resistances of all the cylindrical elements of the pore:

$$R_{gj} = \sum_{x_i} R_{dx}(x_i) \tag{6}$$

$\mathbf{F}$ on each particle at a given instant was calculated by summing the all electrostatic forces and the force due to E:

$$\mathbf{F} = \mathrm{F_Q} + \mathrm{F_E} \tag{7}$$

where $\mathrm{F_E} = E(x)q$ and q is the particle charge.

Table 1
Governing equations for pore and particle geometry.

Geometry	Equation in Cartesian coordinates	Variables and conditions
Ellipsoid	$\frac{x^2}{a^2}+\frac{y^2}{b^2}+\frac{z^2}{c^2}=1$ $a=b>c$: Oblate $a=b<c$: Prolate	a, b: equatorial radii along x and y axis, respectively c: polar radius along z axis.
Cone	$\frac{x^2+y^2}{c^2}=(z-z_0)^2$ where $c=\frac{r}{h}$	r: radius h: height z_0: height of apex above $z=0$ plane
Torus	$(R-\sqrt{x^2+y^2})^2+z^2=r^2$	R: distance from center of tube and center of torus r: radius of tube
Sphere	$x^2+y^2+z^2=r^2$	r: radius of sphere

2.3. Simulation experiment design

The model and simulation environment was implemented using MATLAB R2015b (Mathworks Inc., Natick, MA). Simulation experiments were batched and distributed to run in parallel on 48 computation cores involving 3 Apple Mac Pro computers and 2 Supermicro compute servers (model: X9DRW) running CentOS 7.2. Physical and geometrical parameters of the pore model were varied to study the differences in flux of pores with conical and cylindrical mouths. Two types of experimental conditions were designed to study the effect of pore shape. The first one involved maintaining a constant concentration gradient across the pore, while the other involved studying simple diffusion in the isolated cell-pore-cell system.

2.3.1. Particle flux studies with constant concentration gradient and applied transjunctional voltage

These studies were primarily designed to study the role of pore mouth size and shape on particle flux. A constant concentration gradient was artificially maintained after initially placing the particles in the entire closed volume, and replacing any particle to its respective initial cell as soon as the particles crossed the pore and reached the center of the opposing cell (Fig. 3A and B). Although this gradient was artificial in our system, it was similarly established in *in vitro* experiments during dye injection or double whole cell voltage clamp experiments (Rackauskas et al., 2007a; Valiunas et al., 2002). Since homotypic pores are symmetric across the vestibule, we created only a forward concentration gradient of LY and Cs particles. On the other hand, in heterotypic pores the direction of concentration gradient was selected based on the mouth shape's (conical or cylindrical) effect on LY flux we wanted to study. The forward and reversed concentration gradient was maintained by initially placing the particles in C_1 – facing the conical mouth, or in C_2 – facing the cylindrical mouth, and replacing the particle in the respective initial cell as soon as the particles crossed the pore (Fig. 3A and B). While running the simulations of the model we reversed the concentration gradient to C_2 to C_1, the presented figures involving heterotypic pores have been flipped horizontally so concentration gradient is always in C_1 to C_2 direction (Fig. 3B). This was done to improve visual clarity for readers while comparing shape dependent parameters. Based on the applied transjunctional voltage the pore profile depended E was calculated using Eq. 4 and set (Fig. 3C and D).

A time step of 10 ps was set and LY flux was calculated every 10 μs, considering the total number of particles that had crossed the pore till then and the total time. The simulation was let to run till the net flux value stabilized such that the standard deviation of the last 5 computed values of net flux was less than 5%. At this point the simulation program stopped and saved the particle path and flux data for further analysis. The flux studies maintained a concentration gradient of 4 to 0 LY particles (16 mM) across C_1–C_2. Four particles placed in the fixed volume of cells had an equivalent concentration of 16 mM, which was higher than the experimental values for computational reasons. The high concentration reduced the variability in the model simulations and decreased the number of simulations needed for statistical significance. Simulations were also run for concentration gradients of 2 to 0 (8 mM) and 1 to 0 (4 mM) LY particles to evaluate concentration dependence of results.

2.3.2. Influence of pore's inner and outer mouth size

Based on our observation of the available x-ray crystallographic structures we identified the inner and outer mouth's size to be the geometric variants of possible significance. In our first set of simulations using homotypic pores, we fixed the internal mouth radius at 9.2 Å and varied the outer mouth radius from 9.2 to 36 Å. In the second set of simulations, we fixed the outer diameter at 22.5 Å and changed the inner diameter from 6.2 to 12.5 Å. We approximated all tori and ellipsoids accordingly to the model equations. To reduce the number of simulation runs, fluxes were obtained from applied 2 mV transjunctional voltage. Flux calculated from simulations with 2 mV applied transjunctional voltage would be equivalent to the flux calculated from separate 10 mV and 0 mV simulations as in the *in vitro* experimental condition of 10 mV voltage steps applied for 200 ms at 1 Hz.

2.3.3. Simple diffusion studies

We designed these experimental conditions to approximate steady state in a closed isolated system. We placed equal concentration of LY and Cs (1, 2, 3 LY with 2, 4, 6 Cs particles, respectively) on each side of the pore and allowed simple diffusion to occur for 1 ms. Separate simulations were run with charged and uncharged particles in homotypic and heterotypic pores. Ideally, during simple diffusion we would expect concentration to be the same in all regions (steady state). But, if pore shape and particle charge have any influence, the particle distribution at steady state will shift from ideal. The particle distribution was monitored by counting the number of particles in each side of the center of the pore every 1 μs. To study the overall particle distribution in the pore, we created particle probability maps. The inter-particle electrostatic force per LY particle in different pore sections was also calculated.

2.4. In-pore activity visualization from simulation results

Apart from particle flux and in cell concentration, our simulation also generated data to visualize the particle paths throughout the set

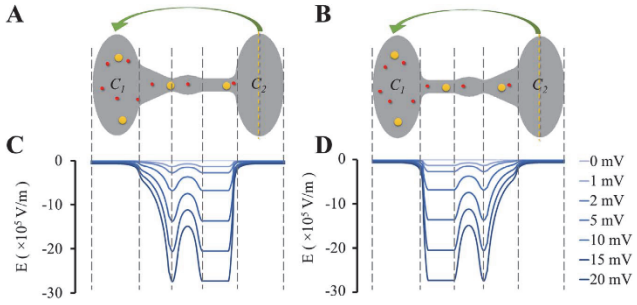

Fig. 3. Simulation experiment design for particle flux studies with constant concentration gradient. (A, B) Experiment design where LY (yellow) and Cs (red) particles are randomly placed in the heterotypic pore. Concentration gradient was maintained from the (A) conical mouth or (B) cylindrical mouth side, by replacing any particle that crosses the central plane of C_2 (yellow line). (C, D) Electric field E in the pore for applied transjunctional voltages of 0–20 mV for the pores shown in (A) and (B), respectively. (For interpretation of the references to color in this figure legend, the reader is referred to the web version of this article.)

simulation time. These data were utilized to predict and identify regions of interest and correlate observed results to changes in particle-interaction in identified region of the pore.

2.4.1. Particle trajectory maps

During a simulation run, each particle's 10^{th} calculated position was recorded and stored. Individual particle paths were plotted to study its movement and identify pore regions where it spends the most or least time. Though these trajectories vary from particle to particle, they provided us with an initial preview of how a particle interacts with and within the pore.

2.4.2. Particle probability maps (2D)

Particle probability maps present particles movement distribution within the pore. In our case, they represent probability of the presence of one or more LY (or Cs) particles in different pore sections. The pore was divided into small cylindrical sections of width dX along its length. In probability maps, based on the selected section length, the corresponding element in y-direction was set. The spatial elements dA ($dA = dX \times dY$ at a point X, Y) in the probability map were incremented by the time stepΔt, if the projected i^{th} particle position $\mathbf{x}$ (at the n^{th} time step) was present within the corresponding element dA. Therefore, as the sum of an element was larger, the particle probability was higher. The final sum of each element was divided by the total simulation time t_{total} to get the actual probability of particle presence $\mathbf{P}_{dA}$.

$$\mathbf{P}_{dA}=\frac{\Delta t}{t_{total}}\sum_{i=1}^{N_p}\sum_{n=1}^{N_t}p_{dA}(i,\ n) \tag{8}$$

where $p_{dA}(i,\ n)=\begin{cases}1, & \mathbf{x}(i,\ n) \text{lies within } dA\\ 0, & \text{otherwise}\end{cases}$

N_p is the number of particles, N_t is the number of time steps. The indices i and n are for particles and time steps, respectively. In the probability maps, blue represents zero probability and red represents maximal probability in that particular simulation.

2.4.3. Average electrical force per particle per pore section

The cell-pore-cell system was divided into 5 major geometric sections from left to right: as (1) cell 1, (2) left mouth, (3) vestibule, (4) right mouth and (5) cell 2 (see Fig. 3A and B). The average force $\mathbf{F}$ acting per LY particle in each of the geometric sections was calculated. The x-component of the average force, F_X was considered significant for comparison, since the gap junction pore's central axis is aligned to the x-axis and flux was being measured in the x-direction.

3. Results

3.1. In vitro *results*

3.1.1. Coupling coefficients in Cx43-Cx45 heterotypic channels

A generally used assessment of coupling levels between cells is obtained by estimating the coupling coefficient from dye iontophoretic injection. Fig. 4A summarizes the results from dye coupling through micropipette injection experiments in coupled HeLa cells in heterotypic configuration (Cx43-Cx45) with LY, R123 and NB as the injected dyes. In Cx45-Cx43 heterotypic channels, injections of similar sized dyes with opposite charges like LY ($2e^-$) and R123 ($2e^+$), yielded results that indicated a favorable movement of dye in the Cx45 to Cx43 direction that was independent of dye particle's electric polarity (2^{nd} and 3^{rd} pair of columns in Fig. 4A). NB, which was positively charged, smaller and elongated in shape did not show this asymmetry (1^{st} pair of columns in Fig. 4A).

3.1.2. LY flux under double whole cell voltage clamp: In vitro *vs* in silico

Double whole cell voltage clamp experiments were performed at 0 mV and 10 mV (200 μs/1 Hz pulses) with pre-labeled HeLa cells expressing Cx43 or Cx45 paired to form homotypic and heterotypic gap junctions. Results for these *in vitro* experiments are shown in Fig. 4B and C. In the experiments using 5 mM LY and applied transjunctional voltage of 10 mV (200 μs/1 Hz pulses) with homotypic gap junction pores (Fig. 4B), the LY flux across Cx45 pores was almost 4 times smaller than that of Cx43 pores. Fig. 4C presents the differences between fluxes expressed in heterotypic pores in the two transjunctional voltage conditions. The flux in the direction Cx43 to Cx45 is smaller than the one in direction Cx45 to Cx43 in both transjunctional voltage cases (Fig. 4C), with a preferential flux in the Cx45 to Cx43 direction at 10 mV pulses with a flux ratio close to 3 (2^{nd} pair of columns in Fig. 4C). Fluxes across heterotypic junctions calculated without continued voltage clamp pulses (0 mV) were significantly smaller (1^{st} pair of columns in Fig. 4C), though the mean values maintain the preference observed in the 10 mV case.

Simulation results (Fig. 4D-F) with our hypothesized model of the Cx43 hemichannel having a conical and Cx45 having a cylindrical mouth shape maintain the asymmetries in homotypic (Fig. 4D) and heterotypic pores (Fig. 4E and F) observed in the *in vitro* experiments was reproduced at different concentration gradients.

3.2. In silico *results*

3.2.1. Overview

Brownian dynamics is considered a realistic representation of particle motion in fluid medium as the trajectories are non-linear and random in direction, taking collisions with water molecules into consideration. The trajectory maps provided insights into the particles' path pattern in the pore model. Since the superimposed trajectories for all particles were difficult to distinguish, we plotted single LY (Fig. 5A) and Cs (Fig. 5B) particle trajectories.

1.8 terabytes (TB) of data were generated in the presented work which involved a total computational runtime of ~21 days per computational core. In general, the simulation time depended on the number of particles in the simulation. The runtime for a 10 μs simulation with 18 (6LY+12Cs) charged particles was ~75 min and 12 (4LY+8Cs) charged particles was ~34 min. Each condition for flux measurement in constant concentration gradient was repeated 20 times (n = 20). Simulation times ranged from 60–350 μs in reaching our set criteria (Section 2.3.1). Fig. 5C shows the total fluxes calculated every 10 μs in 5 (out of 20) running simulations. The variation in total flux values stabilized with time and the final flux value was used. The simple diffusion in isolated system simulations were set to run for 1 ms and repeated 10 times (n = 10).

3.2.2. Simple diffusion and preservation of system steady state with uncharged particles

To evaluate steady state conditions in the simulation model, a computational experiment was set up where initially 3 LY and 6 Cs particles with no charge were placed in each controlled volume of the coupled cells (C_1 and C_2) as shown in the schematic on top of Fig. 6A. At steady state, both sides of the pore should maintain equal concentration (3LY particles/cell). The experiment started at equal distributions and tends to remain in equal distributions as expected in an isolated system. We present the average number of LY particles (n = 10) in L (yellow box in schematic above) after every 1 μs in the heterotypic pore (Fig. 6A). This result was repeated for two types of homotypic pores with the average number of LY particles in L ranged from 2.99–3.03 particles (Fig. 6B). LY particle probability plots in the homotypic (Fig. 6C and D) and heterotypic (Fig. 6E) pores give a picture of the concentration distribution in the pores. As expected the highest particle probability of LY particles was observed in the sections with the largest diameter. In the homotypic cases the distribution was symmetric about the central vestibule. In the heterotypic pore the distribution was asymmetric, with the conical section of the pore

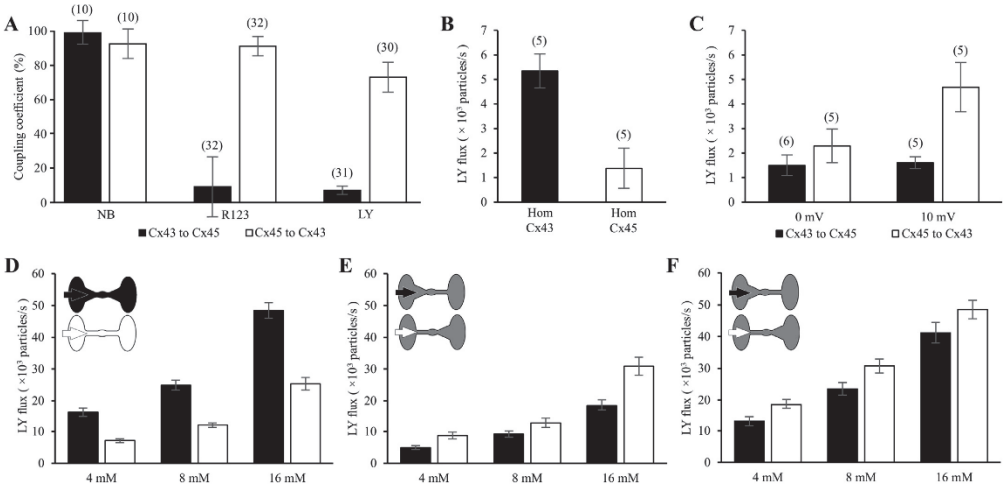

Fig. 4. Comparison of LY fluxes in (A-C) *in vitro* and (D-F) *in silico* experiments. (A) Results from dye iontophoretic injection experiments. Normalized coupling coefficient equals the normalized data from all injections performed. (B) LY fluxes in homotypic Cx43 and Cx45 pores formed in coupled HeLa cells with applied 10 mV transjunctional voltage pulses (200 ms/1 Hz). Homotypic Cx43 pores show ~3 times higher LY flux than in homotypic Cx45. (C) LY fluxes in heterotypic Cx43-Cx45 channels with no and 10 mV applied transjunctional voltage pulses. The LY fluxes are higher in Cx45 to Cx43 direction. The difference is more pronounced for 10 mV pulses. (D) LY fluxes from simulation results with homotypic pores with conical and cylindrical mouths at 4, 8 and 16 mM to 0 concentration gradient and 10 mV applied transjunctional voltage pulses (200 ms/1 Hz). The graphic in the bottom provides the pore profiles and corresponding legends. (E-F) LY fluxes from simulations with heterotypic pores with (E) no or 0 mV and (F) 10 mV applied transjunctional voltage pulses and concentration gradients of 4, 8 and 16 mM to 0 maintained facing either mouths. .

recording a higher probability than the cylindrical section. This imbalance was compensated in C_2 (not shown in probability maps of Fig. 5C-E) which was slightly larger in size than C_1 to keep the system volume equal on either side of the pore center.

3.2.3. *Shift in system steady state in heterotypic pore with charged particles*

The same steady state computational experiment conditions in Section 3.2.2 were repeated using charged LY and Cs particles (simulation results presented in Fig. 7). Fig. 7A presents the variation in number of LY particles in region L with time in the heterotypic pore. Compared to the uncharged particle case (Fig. 6A), the concentration variation was smaller. Also, the LY particles clearly tended to stay in the conical side. There were a significantly larger number of LY particles in the left side of the system in the heterotypic case (3.37 particles in L) compared to the homotypic cases (Fig. 7B). The values were 3.01 and 3.02 for the conical and cylindrical mouthed homotypic pores, respectively. The particle distributions in the heterotypic pore

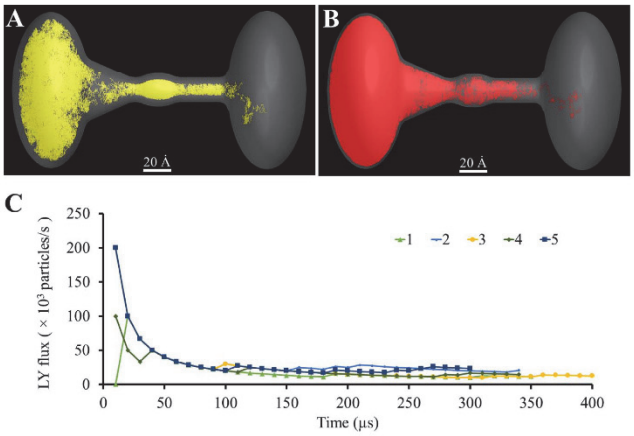

Fig. 5. Simulation of constant concentration gradient. (A-B) Particle trajectories of single (A) LY (in yellow) and (B) Cs (in red) particle that crossed the pore. (C) Calculated total fluxes vs simulation time for 5 different flux simulations of an experimental condition. Simulations were stopped and the final total flux value was determined when the standard deviation of last 5 flux values was less than 5 %. (For interpretation of the references to color in this figure legend, the reader is referred to the web version of this article.)

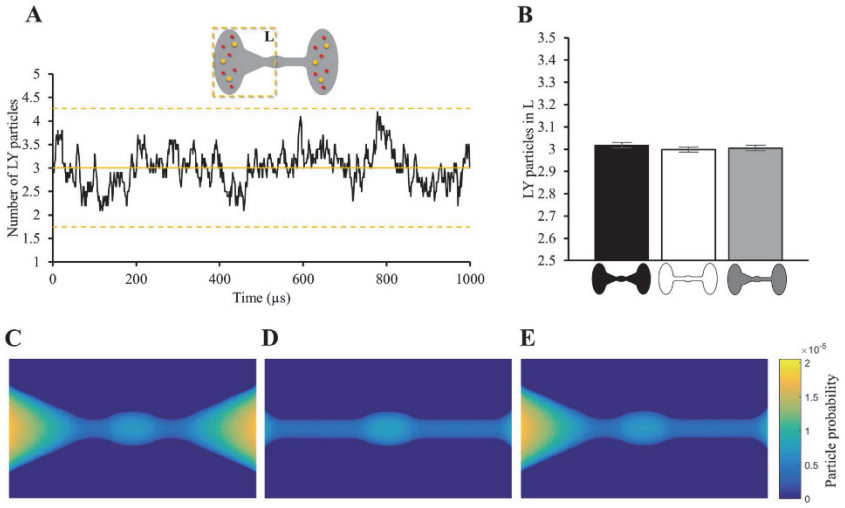

Fig. 6. Steady state simulation results with uncharged particles in homotypic and heterotypic pores. (A) Number of LY particles in left side of pore (region L) vs time in heterotypic pore (n = 10). (B) Average LY particles in L for homotypic and heterotypic pores ranges from 2.99–3.03. The expected ideal mean LY particles was 3. (C-E) Particle probability maps for homotypic pore with (C) conical mouths, (D) cylindrical mouths and (E) heterotypic pore of cone-cylinder combination. The particle probability distributions observed in the mouths of the homotypic pores was maintained in the corresponding mouths of the heterotypic pore.

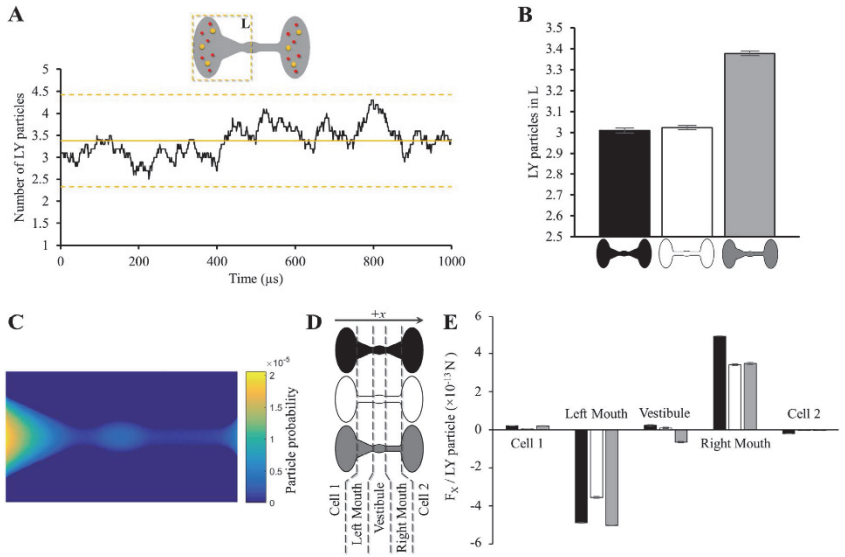

Fig. 7. Steady state simulation results with charged particles in homotypic and heterotypic pores. (A) Number of LY particles in left side of pore (in region L) vs time (n = 10) in heterotypic pore. (B) Average LY particles in L for homotypic and heterotypic pores. While the mean LY particles in homotypic pores is 3, it is 3.37 for the heterotypic pore. (C) Particle probability map for heterotypic pore of cone-cylinder combination. The particle probability distributions has minor differences to that of neutral particles. (D) Pore sections considered for calculating average electrostatic force per LY particle per section. (E) Average electrostatic force in x-direction per LY particle calculated for the divided sections in the pore shown in D. While F_X values are symmetrically balanced in the homotypic pores, there is a significant imbalance in forces between the left and right mouth of the heterotypic pore.

with charged and uncharged particles showed minor differences (particle probability maps in Figs. 6E and 7C). With charged particles, the particle distribution was slightly higher in the vestibule and considerably lower in the narrower regions of the pore, i.e. the toroidal regions adjacent to the vestibule and the cylindrical section. Since, particle charge was the only altered parameter leading to the introduc-

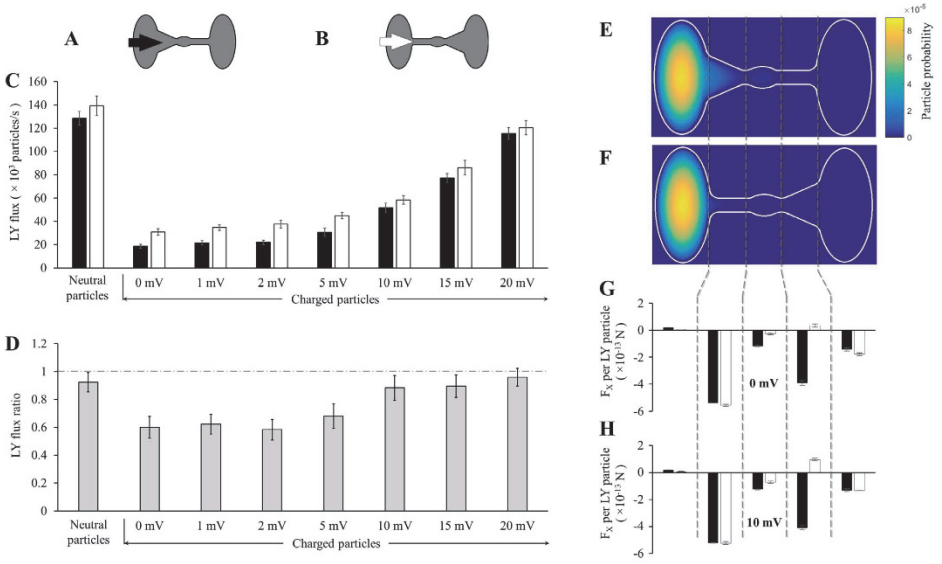

Fig. 8. Effect of applied transjunctional voltage in particle flux studies with constant concentration gradient in a heterotypic pore. (A-B) Heterotypic pore configurations for flux studies and legend for C, G and H. They represent the direction of fluxes in the cone-to-cylinder (black) and cylinder-to-cone (white) directions. (C) Particle fluxes for two configurations (n = 20) with uncharged and charged particles. The flux increases with higher applied transjunctional voltages. The difference in fluxes from each side reduces with rise in applied transjunctional voltage. (D) LY flux ratio (conical mouth: cylindrical mouth) vs applied transjunctional voltage. With increasing applied voltage, flux ratio also increases getting closer to 1, thus reducing flux asymmetry. (E-F) Particle probability maps for LY particles in heterotypic pore with no applied transjunctional voltage with concentration gradient of 4 to 0 in (E) cone-to-cylinder and (F) cylinder-to-cone direction. (G-H) F_X per LY particle in corresponding pore sections for the two pore cases (black and white columns) with applied transjunctional voltages of (G) 0 mV and (H) 10 mV.

tion of electrostatic forces in the system, the forces experienced by particles along the pore section was studied. This was accomplished by calculating the average electrostatic force per LY particle per pore section. Fig. 7D presents the different sections considered for each of the pores. Fig. 7E shows the average force per LY particle in x-direction (F_X) for homotypic pores with conical (black) and cylindrical (white) mouths and their combined heterotypic (grey) pore. F_X in the left and right mouths were most significant amongst all the sections. F_X in the conical mouth was higher than in the cylindrical mouth in homotypic pores and this difference was maintained in the heterotypic pore. In the homotypic pores, F_X magnitudes per section were symmetric about the vestibule with mouth and cell components complementing each other. F_X in the heterotypic pore maintained a significant difference between the left and right mouths. Furthermore, F_X in the vestibule of heterotypic pore had a significant component in the x-direction.

3.2.4. Flux simulations with uncharged and charged particles

Fig. 8C summarizes average fluxes calculated in simulations with a 4 to 0 LY concentration gradient with different applied transjunctional voltage conditions. The first pair of columns represent the fluxes from uncharged particles crossing the heterotypic pore. The other pairs of columns represent fluxes of charged particles crossing the pore with 0–20 mV applied transjunctional voltage. Fig. 8D shows the corresponding LY flux ratios (conical mouth: cylindrical mouth). A flux ratio of ~1 represents no asymmetry and any deviation from 1 indicates asymmetry.

Simulations with uncharged particles, yielded the highest LY flux in either direction and close to no flux asymmetry. When we introduced charged LY and Cs particles into the pore, the fluxes were ~4 times smaller in magnitude compared to those uncharged particles (comparing 1st and 2nd pair of columns in Fig. 8C). Particle probability maps of simulations with charged particles indicated that LY particles spent more time in the left mouth and vestibule in the cone-to-cylinder direction simulations (Fig. 8E and F). Furthermore, at no applied transjunctional voltage or 0 mV, the flux in the direction from cylinder-to-cone (2nd column pair in Fig. 8C) was higher than from cone-to-cylinder with a flux ratio of 0.6. F_X in the different sections of the pore were computed and compared for the two heterotypic cases (Fig. 8G). While F_X in the starting cell (leftmost column pair in Fig. 8G) were insignificant compared to those in the other sections. The most consequential differences in F_X were present in the right mouth and vestibule between the two heterotypic cases (4th and 3rd columns in Fig. 8G).

LY flux increased with increase in applied transjunctional voltage (Fig. 8C). Flux asymmetry decreased with increase in voltage with flux ratio reaching ~1 at 20 mV (Fig. 8D). Application of higher voltage had small changes in sectional F_X values. Fig. 8H shows the sectional F_X values for an applied transjunctional voltage of 10 mV. The major sections with difference between the two heterotypic pores was also seen at the vestibule and right mouth (comparing the 3rd and 4th columns in Fig. 8G and H).

3.2.5. Pore's outer and inner mouth sizes modify particle flux

Crystallographic studies have shown differences in pore shape ((Unger et al., 1999) versus (Maeda et al., 2009)). Furthermore, it is believed that these structures might be different in non-crystallized form in its native state. Since we identified the inner and outer pore mouth as important geometric features of the pore, we ran simulation to study their influence on LY flux. In general, we can infer from Fig. 9 that enlarging pore diameter yields higher flux. Keeping the outer mouth radius constant at 22.5 Å, enlargement of the inner pore (or the vestibule mouth) had a stronger effect on LY flux than enlargement of

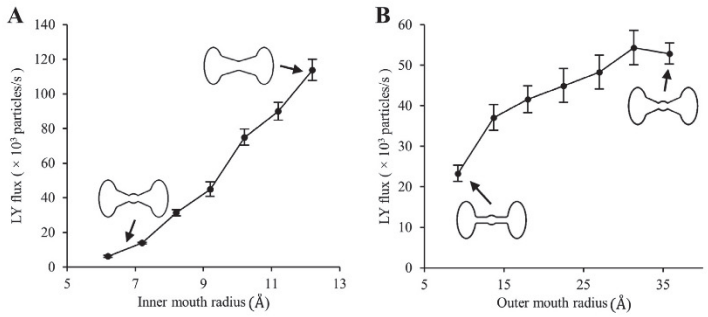

Fig. 9. Fluxes across homotypic pores for varying (A) inner and (B) outer mouth radii. A 4 to 0 LY particles gradient (with Cs counter-ions) was maintained with an applied transjunctional voltage of 2 mV. (A) LY flux increased with inner mouth radius. (B) The relationship between outer mouth radius and LY flux curve was non-linear.

the outer pore mouth keeping the inner pore radius constant at 9.2 Å. LY flux increased with the inner mouth radius (Fig. 9A). The relationship appeared to be quadratic in nature (Fig. 9A). The LY flux-outer mouth radius relationship was non-linear. The relationship appeared to be asymptotic (Fig. 9B).

4. Discussion

Our studies shed light on the effects of gap junction pore shape on asymmetric fluxes by mathematically modeling the flux of large molecules through a non-uniform pore formed by connexins in homotypic and heterotypic configurations. There were three main reasons for the development of this model: first, the biological implications of flux asymmetry are vast as metabolic coupling between cells represents a way to control tissue homeostasis and probably differentiation (Valiunas et al., 2005); second, to help identify and understand the mechanisms associated with pore shape in influencing the asymmetric flux data observed *in vitro*; and third, to set a framework for studies towards determining the functional pore structure through mutagenesis, electrophysiological analysis and permselectivity measurements.

While the primary objective of our simulation design was to study the effects of pore size and shape through flux measurements, simulation studies for simple diffusion were also performed and effect of pore-shape asymmetry on system steady state was demonstrated.

4.1. Importance of particle charge, electric field and pore shape in producing flux asymmetry and deviated steady state

Our simulation results strongly suggested that asymmetric pore shapes could produce asymmetric fluxes (Fig. 8) as well as imbalanced steady states (Fig. 7) in presence of an electric field, generated through particle charges and/or applied transjunctional voltage. The presence of charged particles was crucial to this asymmetry, which disappeared when particle charge was removed in flux (1st pair of columns in Fig. 8C and D) and steady state simulations (3rd column in Fig. 6B).

In simple diffusion simulations, the pore shape effected the configuration of charged particles distribution, which in turn created changes in effective electric field in the pore. Since in homotypic cases, particle distribution was symmetric about the center of the pore, the effective electrostatic force each particle experienced along the axis was symmetric about the center and balanced each other out (black and white columns in Fig. 7E). In the heterotypic case the particle distribution was not symmetric about the center, and a force imbalance existed between the left (conical) and right (cylindrical) pore mouths (grey columns in Fig. 7E). This imbalance in force caused particles to spend more time in the conical side (box L in Fig. 7A) of the pore. Any influence of volume imbalance due to pore asymmetry was eliminated by equalizing the system volume about the center of the pore. This was accomplished by increasing the volume of C_2 (cylindrical side) to compensate for the difference between the conical and cylindrical mouths in the heterotypic pore.

The conditions of our flux simulations were similar to those during dye iontophoresis injections where a strong constant molecular and electrical gradient was generated for 5-10 s when a large amount of dye was injected into one cell (Martínez et al., 2002; Moreno et al., 2004). After the injection, dye flows to other cells through gap junctions and the concentration gradient becomes gradually smaller. In our flux simulation results with charged particles, the heterotypic pore favored flux in the cylinder-to-cone direction at no or small applied transjunctional voltage (< 20 mV). This preference gradually decreased with increase in applied voltage (Fig. 8D). While in the simple diffusion simulations the particles had both cells with high particle probabilities, in flux simulation with constant concentration gradient, only C_1 (leftmost section) had high particle probability (Fig. 8E and F), while C_2 had lowest or negligible particle probability creating a flux from C_1 to C_2. This created an entirely different particle configuration distribution than the simple diffusion experiments. Thus, the effective electrostatic force each particle experienced along the axis depended on the particle configuration distribution in and close to C_1 and the distance of the particle from C_1. In the cylindrical mouth case as in the simple diffusion experiments, the particles tended to stay in C_1 creating an elliptical region of high particle probability (Fig. 8F), while in the conical mouth case the particle tended to additionally spend significant time in the conical mouth (or left mouth in Fig. 8E). This additional charged region not only created a different particle configuration distribution, but also reduced the distance between the charged region to any particle in the pore. This difference caused an increase in the force applied to a particle in the vestibule and right mouth sections of the conical mouth facing heterotypic pore (3rd and 4th column pairs in Fig. 8G and H).

F_X was observed to be low in the vestibule (3rd pair of columns in Fig. 8G and II), which was unexpected. Considering the high probability charged particle region to the major source of the electrostatic force each particle felt and the distance from this source being the significant factor, we expected F_X at the vestibule to be between those in the left mouth and right mouth. We speculate that this was caused by the small vestibular region with narrow mouths in either side, where particles got trapped with counter-ions that diminished the effect of the high probability charge particle region in the left (C_1).

4.2. Influence of inner and outer mouth sizes on flux

We expected a quadratic rise in flux with increase in mouth size as

flux and pore conductance (pore resistance is inversely proportional) are directly proportional to the cross-sectional area. On the contrary, our simulation results with increasing outer pore size presented an asymptotic rise in LY flux (Fig. 9B). This can be explained by considering the pore structure as three series resistors based on the pore sections: (1) left mouth, (2) vestibule and (3) right mouth (sections described before in Fig. 7D). Comparing their relative widths, the vestibule section has the highest resistance considering its narrow mouths (except for the cylindrical mouth cases). Hence, we found a near quadratic rise in LY flux with increase in inner mouth size. On the other hand when we increased the outer mouth size, at smaller sizes the increase in LY flux was much steeper, but reduced as we approached larger mouth sizes. At smaller outer mouth sizes, the resistance of the conical sections (left and right mouth) were closer to the resistance of the vestibule and hence their contribution to the net pore resistance was significant. As the size of the outer mouth was increased, their sectional resistances decreased, until their contribution to the net resistance became insignificant compared to the inner mouth resistance. Hence, at larger outer mouth sizes, increasing mouth size did not impact the LY flux as much as an increase in the inner mouth size did.

4.3. Comparing fluxes from experimental data, Brownian models and theoretical equations

Flux data for several fluorescent dyes in distinct exogenous cell systems have been previously reported (Harris, 2001). The range of fluxes reported for LY in systems under double whole cell voltage clamp ranges from 4000 (Ek-Vitorín et al., 2006; Ek-Vitorín and Burt, 2005; Heyman and Burt, 2008; Kanaporis et al., 2013; Rackauskas et al., 2007a; Valiunas et al., 2002) to 300,000 molecules/channel/s (m/c/s) in Xenopus oocytes pairs (Weber et al., 2004). This discrepancy of close to two orders of magnitude may be due to differences in the cellular approximations and imaging systems used. We recorded fluxes of 5345 ± 687 m/c/s (n = 5) in Cx43 channels and 1380 ± 823 m/c/s (n = 5) in Cx45 channels expressed in HeLa cells using a 5 mM LY concentration (Fig. 4B). Heterotypic pores presented a significant preferential flux direction with fluxes of 4681 ± 1000 m/c/s (n = 5) from Cx45 to Cx43 and 1603 ± 241 m/c/s (n = 5) from Cx43 to Cx45. Assuming the hypothesized shapes, our Brownian diffusion model predicted corresponding flux values of ~15460 m/c/s and ~7894 m/c/s in homotypic pores and ~3263 m/c/s and ~2679 m/c/s in heterotypic pores (interpolating LY flux values to 5 mM). The assumed pore shape in our model produced fluxes ~2 to 8.5 times higher than the experimental data; nonetheless the asymmetric flux direction was clearly established. We suggest that differences in net flux are mostly determined by microscopic effects at the smallest regions of the pore where molecular hindrance, binding and other interactions occur. Another possibility is that the measurements obtained from crystallographic studies do not reflect the physical or functional dimensions of the pore in its natural state, although those pore sizes have been calculated through permeability ratios between large molecules and K^+ ions indicating that for Cx43 the pore radii is 5-6 Å (Kanaporis et al., 2008). Therefore, based on the presented simulation model and experimental data, pore's shape will be a relevant parameter among the other parameters necessary for accurate flux quantification.

4.4. Double whole cell voltage clamp vs dye spread experiments

In vitro experiments designed to determine dye spread across junctions using injecting micropipettes are complicated when several cells are involved since multiple factors can affect the accurate evaluation of this dye spread: 1) dye leaking from the cell membranes; 2) slow dye permeance across junctions and cytoplasm; 3) large number of cells forming primary and secondary junctions with the injected cell; and 4) lack of an effective continuous injection to keep the initially injected cell at maximal concentration. During dye injections, the amount of dye injected is limited and occurs during a short time; hence, dye spread evaluation has to be calculated by determining the number of cells loaded with dye after a predetermined time after injection (Mills and Massey, 1998). Flux evaluation is more accurate during dual whole cell voltage clamp experiments where one pipette is filled with dye and electrical gradient pulses are constantly applied to measure junction communication (Kanaporis et al., 2013). In this closed two-cell system, cell shape is no longer a restriction and there is an infinite source of dye from one pipette. Other parameters like dye leakage and dye binding into the cells are still present, but overall this system is much more effective in estimating fluorescent molecules' fluxes across gap junction channels regardless cell size (Kanaporis et al., 2013; Valiunas, 2002). Therefore, to evaluate flux, we followed these experiments that were based on loading one cell with dye, creating thus a steady, strong and temporary dye gradient across the junction.

In our experiments, when cells expressing Cx43 or Cx45 were paired, LY fluxes were calculated during 10-15 min experiments. To determine the relevance of an electric potential gradient, we performed double blind experiments where the transjunctional current was evaluated every second, or only 3 times during the course of the experiments. The results presented here, suggest that a voltage gradient, even as small as 10 mV was capable of inducing the generation of asymmetric fluxes. This can be observed comparing the fluxes in heterotypic cell pairs with and without applied transjunctional voltage (Fig. 4C).

4.5. Model limitations

Further refinement of the model could also include the molecular surface of the pore through molecular dynamic (Kwon et al., 2011) as well as an approach to diffusion in nano-scale pore regions (Deen, 1987; Mamonov et al., 2006). Besides limitations associated with surface approximations, some non-trivial inaccuracies also exist in our model. The diffusion coefficients of LY and Cs were calculated based on their respective Stokes radii and assumed to be constant throughout the pore, neglecting the possible effects of nearby solute particles and reduced pore section radii. Although Cs was used as the counter-ion to LY, which provided some shielding, shielding effect and obstruction by other ionic particles and/or the pore structure were not considered for particle's net electrostatic force calculation. This perhaps could be one of the factors contributing to the higher calculated values of LY flux. Moreover, we did not consider the charge distribution on the pore surface. At present our study was focused on the effect of only pore shape. In the absence of structural information, pore surface charge distribution could not be implemented. Studies on the effects of positioning single or multiple charged rings in different pore sections can be envisioned. The current literature models represent the pore structure obtained from protein crystals. Since the carboxyl terminus (CT), cytoplasmic loop (CL) and amino terminus (NT) domains have not been all involved in these structures we do not know if the structures reported correspond to open or closed states of the gap junction channels although possibly the structure of Cx26 corresponds to a closed pore (Maeda et al., 2009).

Despite these limitations, we believe that our model represents a step towards describing how fluxes can be regulated across gap junction pores just through their inherent shape. Our study provides insights into how pore structure is related to the channel permeability and selectivity, and how this structure, together with binding, molecular hindrance and gating could determine communication between cells in physiological or pathophysiological states. We suggest that mathematical models will help us understanding the effects of connexin mutations on the pore structure that are related to changes in permeability associated with multiple human diseases.

5. Conclusions

Asymmetric fluxes of metabolites have been detected across heterotypic gap junction channels but the mechanism has not yet been elucidated. In tissues under normal physiological conditions, voltage gating of connexin channels can hardly be responsible for any asymmetric fluxes. Within this manuscript, the use of a conventional Brownian dynamics model has moved forward the field in understanding this phenomenon. Our simulation results point to the distribution pattern of charged particles near the pore's mouth to be a major cause of this observed asymmetric flux with higher fluxes from the cylindrical mouth side and it is based in part on the shape of the pore. It is important to note that our results have also demonstrated the ability of an inactive nano-pore to create active-pore-like behavior to charged molecules and ions entirely based on its shape and length. We can speculate that such behavior can regulate charged metabolites concentration in tissues with heterologous coupling and maintain a higher concentration in cell types that require them through heterotypic channels.

In future studies, other channel properties like pore surface charge distribution and binding sites will have to be considered as the ultrafine details of Cx45 and Cx43 pores become available. So for now, computational studies like the one presented, constitutes an important steps towards understanding the mechanisms involved in diffusion of particles and metabolites across different tissues where heterogeneous cells, expressing distinct connexins are present.

Authorship

Abhijit Mondal, MS, is a PhD candidate in charge of materializing his own ideas and those of the other PI's to accomplish all modeling and simulations results through computer algorithms. He also wrote the first drafts of the manuscript. Daniel Appadurai, MS recorded dye flux from cells during iontophoretic injections or double whole cell voltage clamp. Nazem W. Akoum, MD, participated in the recording of LY fluxes in hetero-multimeric channels. Frank B. Sachse, PhD, participated in developing the mathematical approach of the manuscript. He has contributed substantially with ideas on the model properties and its verification. Alonso P. Moreno, PhD, promoted and encouraged the follow up of all ideas as the principal investigator of the project. His functions were mainly organizing and generating ideas for the implementation of the model and also on data representation. All authors have participated on the manuscript's reviewing and editing.

Acknowledgements

We acknowledge funding for this work from the Nora Eccles Treadwell Foundation and NIH R01 R01-63969 (APM). We would like to thank Ted Dustman, Haonan Yang, Nancy Allen and Dr. Phil Ershler for their computer support at CVRTI. We also thank Zane Zakraisek and Stewart Brock for their assistance towards utilizing the computational servers at the Computer Aided Design and Engineering (CADE) lab, College of Engineering.

References

Allen, T.W., Andersen, O.S., Roux, B., 2004. Energetics of ion conduction through the gramicidin channel. Proc. Natl. Acad. Sci. USA 101, 117–122. http://dx.doi.org/10.1073/pnas.2635314100.

Allen, T.W., Hoyles, M., Kuyucak, S., Chung, S.H., 1999. Molecular and Brownian dynamics study of ion selectivity and conductivity in the potassium channel. Chem. Phys. Lett. 313, 358–365. http://dx.doi.org/10.1016/S0009-2614(99)01004-0.

Beyer, E.C., Gemel, J., Martínez, A.D., Berthoud, V.M., Valiunas, V., Moreno, A.P., Brink, P.R., 2001. Heteromeric mixing of connexins: compatibility of partners and functional consequences. Cell Commun. Adhes. 8, 199–204. http://dx.doi.org/10.3109/15419060109080723.

Bukauskas, F.F., Kreuzberg, M.M., Rackauskas, M., Bukauskiene, A., Bennett, M.V.L., Verselis, V.K., Willecke, K., 2006. Properties of mouse connexin 30.2 and human connexin 31.9 hemichannels: implications for atrioventricular conduction in the heart. Proc. Natl. Acad. Sci. USA 103, 9726–9731. http://dx.doi.org/10.1073/pnas.0603372103.

Chung, S.H., Allen, T.W., Kuyucak, S., 2002. Modeling diverse range of potassium channels with Brownian dynamics. Biophys. J. 83, 263–277. http://dx.doi.org/10.1016/S0006-3495(02)75167-9.

Cooper, K., Jakobsson, E., Wolynes, P., 1985. The theory of ion transport through membrane channels. Prog. Biophys. Mol. Biol. 46, 51–96. http://dx.doi.org/10.1016/0079-6107(85)90012-4.

Corry, B., Allen, T.W., Kuyucak, S., Chung, S.H., 2001. Mechanisms of permeation and selectivity in calcium channels. Biophys. J. 80, 195–214. http://dx.doi.org/10.1016/S0006-3495(01)76007-9.

Corry, B., Kuyucak, S., Chung, S.H., 2000. Invalidity of continuum theories of electrolytes in nanopores. Chem. Phys. Lett. 320, 35–41. http://dx.doi.org/10.1016/S0009-2614(00)00206-2.

Deen, W.M., 1987. Hindered transport of large molecules in liquid-filled pores. AIChE J. 33, 1409–1425. http://dx.doi.org/10.1002/aic.690330902.

del Corsso, C., Srinivas, M., Urban-Maldonado, M., Moreno, A.P., Fort, A.G., Fishman, G.I., Spray, D.C., 2006. Transfection of mammalian cells with connexins and measurement of voltage sensitivity of their gap junctions. Nat. Protoc. 1, 1799–1809. http://dx.doi.org/10.1038/nprot.2006.266.

Eckert, R., 2006. Gap-junctional single-channel permeability for fluorescent tracers in mammalian cell cultures. Biophys. J. 91, 565–579. http://dx.doi.org/10.1529/biophysj.105.072306.

Ek-Vitorin, J.F., Burt, J.M., 2005. Quantification of gap junction selectivity. Am. J. Physiol. Cell Physiol. 289, C1535–C1546. http://dx.doi.org/10.1152/ajpcell.00182.2005.

Ek-Vitorin, J.F., King, T.J., Heyman, N.S., Lampe, P.D., Burt, J.M., 2006. Selectivity of connexin 43 channels is regulated through protein kinase C – dependent phosphorylation. Circ. Res. 98, 1498–1505. http://dx.doi.org/10.1161/01.RES.0000227572.45891.2c.

Elenes, S., Martinez, A.D., Delmar, M., Beyer, E.C., Moreno, A.P., 2001. Heterotypic docking of Cx43 and Cx45 connexons blocks fast voltage gating of Cx43. Biophys. J. 81, 1406–1418. http://dx.doi.org/10.1016/S0006-3495(01)75796-7.

Ermak, D.L., McCammon, J.A., 1978. Brownian dynamics with hydrodynamic interactions. J. Chem. Phys. 69, 1352–1360. http://dx.doi.org/10.1063/1.436761.

Finkelstein, A., 1994. Gap junctions and intercellular communications. Science 265, 1017–1018. http://dx.doi.org/10.1126/science.265.5175.1017-b.

Goldberg, G.S., Moreno, A.P., Lampe, P.D., 2002. Gap junctions between cells expressing connexin 43 or 32 show inverse permselectivity to adenosine and ATP. J. Biol. Chem. 277, 36725–36730. http://dx.doi.org/10.1074/jbc.M109797200.

Graf, P., Kurnikova, M.G., Coalson, R.D., Nitzan, A., 2004. Comparison of dynamic lattice monte carlo simulations and the dielectric self-energy poisson-nerst-planck continuum theory for model ion channels. J. Phys. Chem. B 108, 2006–2015. http://dx.doi.org/10.1021/jp0355307.

Harris, A.L., 2008. Connexin specificity of second messenger permeation: real numbers at last. J. Gen. Physiol. 131, 287–292. http://dx.doi.org/10.1085/jgp.200809998.

Harris, A.L., 2007. Connexin channel permeability to cytoplasmic molecules. Prog. Biophys. Mol. Biol. 94, 120–143. http://dx.doi.org/10.1016/j.pbiomolbio.2007.03.011.

Harris, A.L., 2001. Emerging issues of connexin channels: biophysics fills the gap. Q. Rev. Biophys. 34, 325–472. http://dx.doi.org/10.1017/S0033583501003705.

Harris, A.L., Spray, D.C., Bennett, M.V.L., 1981. Kinetic properties of a voltage-dependent junctional conductance. J. Gen. Physiol. 77, 95–117. http://dx.doi.org/10.1085/jgp.77.1.95.

Heyman, N.S., Burt, J.M., 2008. Hindered diffusion through an aqueous pore describes invariant dye selectivity of Cx43 junctions. Biophys. J. 94, 840–854. http://dx.doi.org/10.1529/biophysj.107.115634.

Huber, G.A., Kim, S., 1996. Weighted-ensemble Brownian dynamics simulations for protein association reactions. Biophys. J. 70, 97–110. http://dx.doi.org/10.1016/S0006-3495(96)79552-8.

Im, W., Roux, B., 2002. Ion permeation and selectivity of OmpF porin: a theoretical study based on molecular dynamics, Brownian dynamics, and continuum electrodiffusion theory. J. Mol. Biol. 322, 851–869. http://dx.doi.org/10.1016/S0022-2836(02)00778-7.

Kanaporis, G., Brink, P.R., Valiunas, V., 2013. Gap junction permeability : selectivity for anionic and cationic probes. Am. J. Physiol. Cell Physiol. 300, C600–C609. http://dx.doi.org/10.1152/ajpcell.00316.2010.

Kanaporis, G., Mese, G., Valiuniene, L., White, T.W., Brink, P.R., Valiunas, V., 2008. Gap junction channels exhibit connexin-specific permeability to cyclic nucleotides. J. Gen. Physiol 131, 293–305. http://dx.doi.org/10.1085/jgp.200709934.

Kwon, T., Harris, A.L., Rossi, A., Bargiello, T.A., 2011. Molecular dynamics simulations of the Cx26 hemichannel: evaluation of structural models with Brownian dynamics. J. Gen. Physiol. 138, 475–493. http://dx.doi.org/10.1085/jgp.201110679.

Lee, K. Il, Rui, H., Pastor, R.W., Im, W., 2011. Brownian dynamics simulations of ion transport through the VDAC. Biophys. J. 100, 611–619. http://dx.doi.org/10.1016/j.bpj.2010.12.3708.

Maeda, S., Nakagawa, S., Suga, M., Yamashita, E., Oshima, A., Fujiyoshi, Y., Tsukihara, T., 2009. Structure of the connexin 26 gap junction channel at 3.5 A resolution. Nature 458, 597–602. http://dx.doi.org/10.1038/nature07869.

Mamonov, A.B., Kurnikova, M.G., Coalson, R.D., 2006. Diffusion constant of K+ inside Gramicidin A: a comparative study of four computational methods. Biophys. Chem. 124, 268–278. http://dx.doi.org/10.1016/j.bpc.2006.03.019.

Martínez, A.D., Hayrapetyan, V., Moreno, A.P., Beyer, E.C., 2002. Connexin43 and connexin45 form heteromeric gap junction channels in which individual components determine permeability and regulation. Circ. Res. 90, 1100–1107. http://dx.doi.org/

10.1161/01.RES.0000019580.64013.31.
Mills, S.L., Massey, S.C., 1998. The kinetics of tracer movement through homologous gap junctions in the rabbit retina. Vis. Neurosci. 15, 765–777. http://dx.doi.org/10.1017/S0952523898154159.
Mondal, A., Appadurai, D.A., Amhed, O., Moreno, A.P., 2009. Simulation of particle diffusion across gap junction channels based on their pore geometry explains unidirectional fluxes. Biophys. J. 96, 284a. http://dx.doi.org/10.1016/j.bpj.2008.12.1406.
Mondal, A., Moreno, A.P., 2010. Heteromultimeric gap-junction channel permeance: directional fluxes simulated using a Brownian dynamics model. Biophys. J. 98, 94a–95a. http://dx.doi.org/10.1016/j.bpj.2009.12.532.
Moreno, A.P., Hayrapetyan, V., Zhong, G., Martinez, A.D., Beyer, E.C., 2004. Homomeric and heteromeric gap junctions Fourth Ed. 126. Cardiac Electrophysiology: From Cell to Bedside, 120–126. http://dx.doi.org/10.1016/B0-7216-0323-8/50017-8.
Pau, P.C.F., Berg, J.O., McMillan, W.G., 1990. Application of Stokes' law to ions in aqueous solution. J. Phys. Chem. 94, 2671–2679. http://dx.doi.org/10.1021/j100369a080.
Rackauskas, M., Kreuzberg, M.M., Pranevicius, M., Willecke, K., Verselis, V.K., Bukauskas, F.F., 2007a. Gating properties of heterotypic gap junction channels formed of connexins 40, 43, and 45. Biophys. J. 92, 1952–1965. http://dx.doi.org/10.1529/biophysj.106.099358.
Rackauskas, M., Verselis, V.K., Bukauskas, F.F., 2007b. Permeability of homotypic and heterotypic gap junction channels formed of cardiac connexins mCx30.2, Cx40, Cx43, and Cx45. Am. J. Physiol. Heart Circ. Physiol. 293, H1729–H1736. http://dx.doi.org/10.1152/ajpheart.00234.2007.
Robinson, S.R., Hampson, E.C., Munro, M.N., Vaney, D.I., 1993. Unidirectional coupling of gap junctions between neuroglia. Science 262, 1072–1074. http://dx.doi.org/10.1126/science.8093125.
Schirmer, T., Phale, P.S., 1999. Brownian dynamics simulation of ion flow through porin channels. J. Mol. Biol. 294, 1159–1167. http://dx.doi.org/10.1006/jmbi.1999.3326.
Unger, V.M., Kumar, N.M., Gilula, N.B., Yeager, M., 1999. Three-dimensional structure of a recombinant gap junction membrane channel. Science 283, 1176–1180. http://dx.doi.org/10.1126/science.283.5405.1176.
Valiunas, V., 2002. Biophysical properties of connexin-45 gap junction hemichannels studied in vertebrate cells. J. Gen. Physiol. 119, 147–164. http://dx.doi.org/10.1085/jgp.119.2.147.
Valiunas, V., Beyer, E.C., Brink, P.R., 2002. Cardiac gap junction channels show quantitative differences in selectivity. Circ. Res. 91, 104–111. http://dx.doi.org/10.1161/01.RES.0000025638.24255.AA.
Valiunas, V., Polosina, Y.Y., Miller, H., Potapova, I.A., Valiuniene, L., Doronin, S., Mathias, R.T., Robinson, R.B., Rosen, M.R., Cohen, I.S., Brink, P.R., 2005. Connexin-specific cell-to-cell transfer of short interfering RNA by gap junctions. J. Physiol. 568, 459–468. http://dx.doi.org/10.1113/jphysiol.2005.090985.
Veenstra, R.D., 2001. Determining ionic permeabilities of gap junction channels. In: Connexin Methods and Protocols: Methods in Molecular Biology. Springer, 293–311.
Veenstra, R.D., Wang, H.Z., Beyer, E.C., Brink, P.R., 1994. Selective dye and ionic permeability of gap junction channels formed by connexin45. Circ. Res. 75, 483–490. http://dx.doi.org/10.1161/01.RES.75.3.483.
Vora, T., Corry, B., Chung, S.H., 2008. Brownian dynamics study of flux ratios in sodium channels. Eur. Biophys. J. 38, 45–52. http://dx.doi.org/10.1007/s00249-008-0353-5.
Weber, P.A., Chang, H.C., Spaeth, K.E., Nitsche, J.M., Nicholson, B.J., 2004. The permeability of gap junction channels to probes of different size is dependent on connexin composition and permeant-pore affinities. Biophys. J. 87, 958–973. http://dx.doi.org/10.1529/biophysj.103.036350.

CHAPTER 4

MODULATION OF ASYMMETRIC FLUX IN HETEROTYPIC GAP JUNCTIONS BY PORE SHAPE, PARTICLE SIZE AND CHARGE

(Submitted to Frontiers in Physiology, January 2017)

4.1 Abstract

Gap junction channels play a vital role in intercellular communication between cells by connecting cytoplasm of adjoined cells through arrays of channel-pores formed at the common membrane junction. Their structure and properties vary depending on the connexin isoform(s) involved in forming the full gap junction channel. Lack of information on the molecular structure of gap junction channels has limited the development through computational tools for single channel studies. Currently, we rely on cumbersome experimental techniques that have limited capabilities. We have earlier reported a simplified Brownian dynamics gap junction pore model and demonstrated that variations in pore shape at the single channel level can explain some of the differences in permeability of heterotypic channels observed in *in vitro* experiments. Based on this computational model, we designed simulations to study the influence of pore shape, particle size and charge in homotypic and heterotypic pores. We simulated dye diffusion under whole cell voltage clamping. Our simulation studies with pore shape variations revealed a pore shape

with maximal flux asymmetry in a heterotypic pore. We identified pore shape profiles that match the *in silico* flux asymmetry results to the *in vitro* results of homotypic and heterotypic gap junction formed out of Cx43 and Cx45. Our simulation results indicate that the channel's pore-shape established flux asymmetry and that flux asymmetry is primarily regulated by the sizes of the conical and/or cylindrical mouths at each end of the pore. Within the set range of particle size and charge, flux asymmetry was found to be independent of particle size and directly proportional to charge magnitude. While particle charge was vital to creating flux asymmetry, charge magnitude only scaled the observed flux asymmetry. Our studies identified the key factors in our results that help predict asymmetry. Finally, we suggest the role of such flux asymmetry in creating concentration imbalances of messenger molecules in cardiomyocytes. We also assess the potency of fibroblasts in aggravating such imbalances through Cx43-Cx45 heterotypic channels in fibrotic heart tissue.

4.2 Introduction

Gap junction channels provide pores through cell membranes between two adjoined cells, allowing transport of cytoplasmic molecules amongst them. Each gap junction channel is formed of two coaxially placed connexons (or hemichannels) with one in each cell membrane. Each of these connexons are made of 6 circumferentially arranged connexins (Cx). To date, 21 different Cx types have been identified in humans [1]. Gap junction channels are called homotypic when Cx in both hemichannels are made of the same type, and heterotypic if the Cx in each hemichannel is different. They can also be heteromeric or hetero-multimeric where multiple Cx types constitute a hemichannel. Gap

junctions play key roles in intercellular communication between cells in different tissues like the skin, nervous system, respiratory epithelium, bones, lens and retina of the eye, inner ear, heart, vasculature and reproductive systems. Density and regulation of gap junctions are essential for cellular and tissue physiology. How these channels are relevant in the development of several diseases has become clearer as more regulatory mechanisms that involve channel expression, localization and cellular modifications are known [2]–[6].

Currently, x-ray crystallographic structures of only Cx26 and Cx43 are available [7], [8], with data on molecular structure and in-pore charge distribution available only for Cx26. Structural details are a requisite for using existing computational approaches for studying membrane channels like ion channels [9]–[12] and porins [13]–[15]. Molecular modeling of Cx26 hemichannels [16], [17] was performed for studying their structure/function relations. Limitations and difficulties in deriving such structures pose a barrier to studying the structure and permeability functions of the whole range of gap junction channel types. Thus, most studies rely heavily on *in vitro* experimental methods like dye diffusion, double whole cell voltage and patch clamping. Fluorescent dyes were a vital tool in such studies with Lucifer yellow (LY) being the most commonly used for dye diffusion studies [18]–[26]. Gap junctions serve as conduits for intercellular diffusion and transport studies of physiologically relevant molecules and ions were also conducted [22], [26]–[39]. Our research focused on homotypic and heterotypic gap junction channels involving Cx43 and Cx45, which are abundantly present in the heart [40]–[42]. In previous works, we found that Cx43 and Cx45 heterotypic channels do not rectify electrical current [43]. Calculations of dye diffusion using cell pairs under double whole cell voltage clamp experiments indicate that homotypic Cx43 channels allow higher LY flux than Cx45

channels, while heterotypic Cx43-Cx45 channels show asymmetric fluxes in either direction [22], [44], [45]. Interestingly, the recorded fluxes were higher in Cx45 to Cx43 direction than Cx43 to Cx45. Based solely on their respective unitary conductance, it was theorized that Cx43 would be a wider hemichannel than Cx45, which explained the difference in homotypic fluxes, but failed to explain the flux difference in the heterotypic Cx43-Cx45 junctions. We speculated on a structural basis for this asymmetry, which had been proposed before to explain similar findings [46]. The proposed hypothesis was criticized at the time as it implied the presence of an active mechanism [47]. Subsequently, we suggested using a simplified Brownian dynamics computational model that a heterotypic pore can generate such an active mechanism by creating electrical fields across the pore through motion and redistribution of charged particles [45].

Here we use the simplified Brownian dynamics model of a gap junction pore presented in our previous work to mimic LY diffusion experiments under whole cell voltage clamp. We designed our studies to elucidate the roles of pore shape, particle size and charge on flux and flux asymmetry of large molecules. Simulation studies were conducted for both homotypic and heterotypic pores. Our studies revealed a heterotypic pore profile with maximum flux asymmetry and also pore-shapes that matched our previously reported *in vitro* results with Cx43 and Cx45 pores. We also found that within the set limits, flux asymmetry was almost independent of particle size and scaled by particle charge. While it was not possible to establish a direct relationship between pore-shape, particle charge and size, we identified factors for predicting flux asymmetry. We also speculated on a possible role of such asymmetric fluxes in heart disease.

4.3 Methods

4.3.1 Simulation model

Our simplified Brownian dynamic gap junction simulation model [45] was developed using MATLAB (Mathworks Inc., Natik, MA). In short, particles were modeled as spheres with point charges at their center. Stoke's radius values were adjusted for different particles size. The system was charge balanced by adding appropriate counter-ions. The simulation parameters were set to mimick *in vitro* dye diffusion under double whole cell voltage clamp experiments with coupled cells (Fig. 4.1A-D). We modeled all our pore shape studies with Lucifer yellow (yellow arrows in Fig. 4.1A-D) particles and Cesium (Cs) counter-ions with a 2 mV transjunctional voltage. A 2 mV transjunctional voltage would give a flux equivalent to one from 10 mV/200 ms/1 Hz pulses. A constant concentration gradient of 2 LY and 4 Cs (8 mM LY) was maintained across the pore by replacing any particle that crossed over to cell 2 (central plane of cell 2) back to cell 1. A time step of 1 ps was set. The program saved particles' positions every 10^{th} time step (10 ps). Data files containing particle positions were saved every 10 μs. The LY particle flux was calculated every 10 μs considering the total number of particles and simulation time. The simulation was terminated when the last 5 calculated LY flux values had a standard deviation < 5% or simulation total time was 500 μs.

4.3.2 Simulation experiment design

The simulations were run on 4 Apple Mac Pro computers involving a total of 44 (12 × 3 + 8) processing cores. Our simulation studies were designed to assess the role of pore shape, particle size and particle charge on flux asymmetry in heterotypic pores.

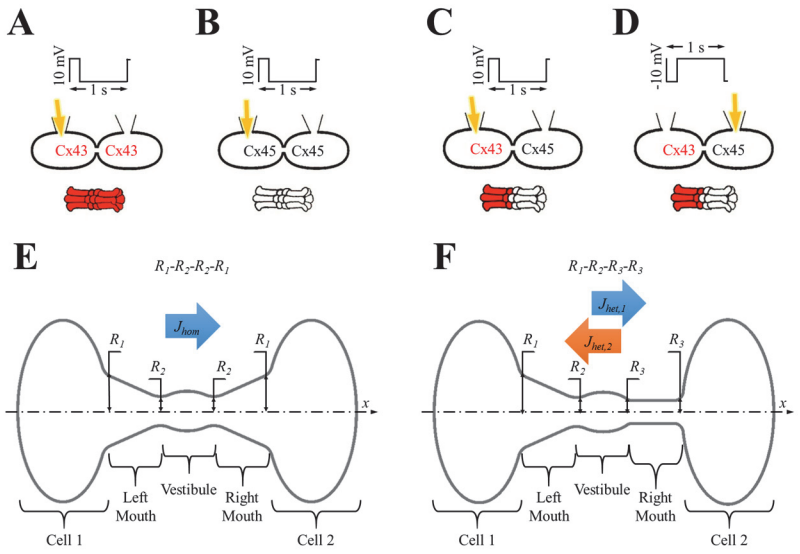

Figure 4.1 – *In vitro* and *in silico* experiment designs with homotypic and heterotypic gap junction pores. (A-D) Basic setup for *in vitro* dye diffusion experiments under double whole cell voltage clamp with homotypic (A) Cx43 and (B) Cx45 gap junction pores and heterotypic Cx43-Cx45 gap junction pores with LY (yellow arrow) injected from (C) Cx43 side and (D) Cx45 side. Voltage pulses of 10 mV/200 ms/1 s were applied and LY dye diffusion was recorded across the gap junction. (E-F) Simulation experiment design for single (E) homotypic and (F) heterotypic gap junction pore. The cell-pore-cell system was divided in 5 sections: (1) cell 1, (2) left mouth, (3) vestibule (4), right mouth and (5) cell 2.

Simulation conditions were defined accordingly as described below.

The averaged gap junction pore was divided into 3 sections defined by 4 radii (R_1, R_2, R_3 and R_4) at the section ends placed in series. A pore was identified by listing these pore-section radii (in Å) in order from left to right as R_1-R_2-R_3-R_4. Homotypic pores were symmetric about the vestibule, $R_1 = R_4$ and $R_2 = R_3$ (Fig. 4.1E) and were denoted as R_1-R_2-R_2-R_1. Heterotypic pores studied in this work were always in a cone-cylinder combination of hemichannels, which means $R_3 = R_4$. So, in all our simulations, heterotypic pores will be of the form R_1-R_2-R_3-R_3. A range of values were set for the outer (R_1) and inner pore (R_2) radii taking into consideration the particle size and computation time. In our studies,

inner mouth radii ranged from 6.2 Å to 12.2 Å and outer mouth radii ranged from 6.2 Å to 25.9 Å. In all our pore radii combination, outer mouth radii were never smaller than the inner mouth radii to avoid inverted conical pore sections.

4.3.2.1 Flux simulations in homotypic pores (R_1-R_2-R_2-R_1)

Table 4.1 lists the inner (R_1) and outer (R_2) mouth radii considered for forming homotypic pores. Fig. 4.1E shows the homotypic pore simulation setup. Based on our set criteria for selecting combinations, 56 homotypic pores were considered. Flux simulations were run for each pore 30 times (n = 30).

4.3.2.2 Flux simulations in heterotypic pores

Our previous work [45] was focused around the hypothesis that flux asymmetry in heterotypic pores can be produced if one of the pore mouths was cylindrical and the other was conical. Simulation were designed to study the effects of R_1, R_2 and R_3 in different simulation sets (rows 1-3 in Table 4.2). Each simulation case was repeated 50 times (n = 50) on either direction (cone to cylinder and cylinder to cone) of the heterotypic pore. In the 1st set of simulations (row 1 in Table 4.2), R_1 was varied while R_2 and R_3 were fixed to 9.2 Å. This basically simulates the effect of varying cone angle of the conical mouth of the

Table 4.1: Sectional radii of homotypic pores.

R_1 (Å)	6.2, 7.2, 8.2, 9.2, 10.2, 11.2, 12.2, 15.8, 20.2, 22.5, 25.9
R_2 (Å)	6.2, 7.2, 8.2, 9.2, 10.2, 11.2, 12.2

Table 4.2: Sectional radii combinations for heterotypic pores.

S#	Shape combination (Å)	Radius (Å)
1	R_1-9.2-9.2-9.2	R_1 = {9.2, 10.2, 11.2, 12.2, 15.8, 20.2, 22.5, 25.9}
2	22.5-R_2-9.2-9.2	R_2 = {6.2, 7.2, 8.2, 9.2, 10.2, 11.2, 12.2}
3	22.5-9.2-R_3-R_3	R_3 = {6.2, 7.2, 8.2, 9.2, 10.2, 11.2, 12.2}
4	25.9-12.2-R_3-R_3	R_3 = {6.2, 7.2, 8.2, 9.2, 10.2, 11.2, 12.2}

pore. In the 2nd set of simulations, R_2 was varied, with R_1 = 22.5 Å and R_3 = 9.2 Å. Here, the influence of inner mouth size was studied. In the 3rd set, the cylinder mouth size was varied while the left conical mouth was kept constant, with R_1 = 22.5 Å and R_2 = 9.2 Å. Finally, in our 4th simulation set, the conical mouth was set to the maximal R_1 and R_2, with R_1 = 25.9 Å and R_2 = 12.2 Å and the effects of varying the cylinder mouth were investigated.

4.3.2.3 Flux simulations with varying particle size

In this set of simulations, the particle size was varied from 0.8 Å to 6.6 Å. Row 1 in Table 4.3 lists the heterotypic pore and the particle radii values used. While the particle size was varied, the counter-ion size was kept constant. Particle charge was set to $2e^-$.

Table 4.3: Particle sizes and charges for heterotypic pore simulations.

S#	Pore profile (Å)	Parameter	Values
1	25.9-12.2-8.2-8.2	Particle radius, r_p (Å)	r_p = {0.8, 1.79, 2.7, 3.8, 4.9, 6, 6.6}
2	25.9-12.2-8.2-8.2	Particle charge, q_p (e^-)	q_p = {0, 0.5, 1, 2, 2.5}

4.3.2.4 Flux simulations with varying particle charge

In our previous work, particle charge was an important factor in creating the observed flux asymmetry of large ionic particles. In this set of simulations, we varied the particle charge (Row 2 in Table 4.3) to study the influence of charge on flux asymmetry. The number of counter-ions was accordingly changed to maintain charge balance. Particle radii of LY and Cs were not changed.

4.3.3 Simulation output and analysis

Simulation data were collected and processed for analysis on an 8 core Apple Mac Pro computer using MATLAB R2016a. This included data verification, tabulating particle fluxes, calculating particle probabilities and sectional forces and data organization. The final result tables and plots were created with Excel 2013 (Microsoft Inc., Redmond, WA).

4.3.3.1 Particle flux and flux asymmetry

Particle flux J was calculated by counting the total number of particles that crossed the pore n_p divided by the total simulation time t.

$$J = \frac{n_p}{t} \quad (4.1)$$

In homotypic pores, flux was only measured in the *x* direction where the concentration gradient of 2LY + 4Cs to 0 particles was maintained between cell 1 and cell 2 and denoted by J_{hom} (Fig. 4.1E). In heterotypic pores, flux was measured in the *x* direction with 2LY + 4Cs to 0 particles in cell 1 to cell 2 (or cone to cylinder direction), and the -*x* direction with 2LY+4Cs to 0 particles in cell 2 to cell 1 (or cylinder to cone direction) and denoted by $J_{het,1}$ and $J_{het,2}$, respectively (Fig. 4.1F).

Flux ratio was the measure of flux asymmetry α_{het} in a heterotypic pore and defined as the ratio of the LY (or particle) fluxes in cone to cylinder ($J_{het,1}$) and cylinder to cone ($J_{het,2}$) directions.

$$\alpha_{het} = \frac{J_{het,1}}{J_{het,2}} \quad (4.2)$$

Heterotypic flux ratios were plotted in log scale (base 2) to accurately scale the magnitude of flux asymmetry in reversed cases (e.g., α_{het} of 0.5 and 2 are equal in magnitude but in opposite directions).

Ratio of the homotypic fluxes of the corresponding hemichannels in a heterotypic pore, α_{hom}, was also calculated to identify reversal of flux asymmetry.

$$\alpha_{hom} = \frac{J_{hom,1}}{J_{hom,2}} \quad (4.3)$$

where $J_{hom,1}$ and $J_{hom,2}$ are the fluxes in corresponding homotypic pores formed of the left and right hemichannels, respectively.

4.3.3.2 Particle probability

Particle probability profiles along the pore's axial profile (along *x*-axis) were calculated from the simulation data and plotted. Axial particle probability P_{dX} was the

probability of particle presence within a cylindrical section of width *dX* at **x** of the pore:

$$P_{dX} = \frac{\Delta t}{t_{total}} \sum_{i=1}^{N_p} \sum_{n=1}^{N_t} p_{dX}(i,n) \quad (4.4)$$

$$where\ p_{dX}(i,n) = \begin{cases} 1, & \mathbf{x}(i,n)\ lies \text{ within } dX \\ 0, & \text{otherwise} \end{cases}$$

Here, Δt is the time step, t_{total} is the total simulation time, N_p is the number of particles, N_t is the number of time steps, **x** is the particle position, and *i* and *n* are the particle and time indexes, respectively.

4.3.3.3 Average electrical force per particle per pore section

The average electrical force per particle per pore section was calculated as in our previous work [45]. In short, the pore was divided into 5 sections in series: (1) cell 1 (C1), (2) left mouth (LM), (3) vestibule (VT), (4) right mouth (RM) and (5) cell 2 (C2) as shown in Fig 1(E-F). The average interparticle electrostatic and electric field forces per particle type **F** was calculated. The x-component of **F** F_X was plotted and compared amongst the different simulation conditions.

While the actual simulations were done in +*x* and -*x* directions, the -*x* data for P_{dX} and F_X data presented here were flipped horizontally so all flux direction are in the +*x* direction. This simplified it for the reader to compare the presented data in the different cases.

4.4 Results

The results presented in the next sections were derived from ~2.2 TB simulation data resulting from ~28.3 days of computation time per processing core (44 processors).

This excludes data handling and postprocessing done on the central workstation (8 processing cores).

4.4.1 Flux simulations in homotypic pores

Fluxes across homotypic pores do not present asymmetry. Table 4.S1 list the fluxes for all 56 homotypic pores considered. Figures 4.S1 to 4.S4 present fluxes, particle probability profiles and average electrical force data arranged to study variations in outer (R_1) and inner (R_2) mouth radii. LY flux values in our simulation with 8 to 0 mM LY gradient ranged from 3551 molecules per pore per s (m/c/s) to 64,588 m/c/s in homotypic pores (Table 4.S1) and 2919 m/c/s to 51409 m/c/s in heterotypic pores (Table 4.S2). Physiological reported values of LY flux range from 4000 m/c/s (m/c/s) [25], [48]–[51] to 300,000 m/c/s [52].

4.4.1.1 Outer mouth variation in conical mouthed pores: R_1-6.2-6.2-R_1 and R_1-12.2-12.2-R_1

Results for fixed inner mouth radii (R_2) of 6.2 Å (narrow mouth) and 12.2 Å (wide mouth) with varying outer mouth radius are presented in Figures 4.S1 and 4.S2, respectively. In pores with narrow inner mouth (R_2 = 6.2 Å), an increasing outer mouth marginally changed the LY flux (Fig. 4.S1A). When the inner mouth radius was widened (R_2 = 12.2 Å), increasing the outer mouth radius increased the LY flux which tended to saturate at higher values of R_1 (Fig. 4.S2A).

The P_{dX} profile in cell 1 was of the same order in all cases (Fig. 4.S1B and 4.S2B) indicating a constant LY concentration in cell 1. As the outer mouth was varied, the P_{dX}

profile varied across the pore. The vestibule size was kept constant and for wide inner pore mouth (R_2 = 12.2 Å), the P_{dX} profiles in the vestibule were of the same order. The P_{dX} profiles tended to be noisier with increasing distance along x from cell 1, and were noisiest at the rightmost region (cell 2). In general, the particle probability profiles were reminiscent of their expected concentration profiles based on the pore's radius profile in simple diffusion, but in the logarithmic scale (base 10). R_2 = 6.2 Å created probability profiles with the most variations along the pore sections, while R_2 =12.2 Å presented a more gentle probability variation.

Homotypic pores with R_2 = 6.2 Å had the highest F_X magnitudes (Fig. 4.S1C and 4.S3C). These were mostly observed in the left and right mouth of the pore. F_X also varied the most in those sections with varying outer mouth sizes. In the left mouth though, the trend was nonlinear. F_X rose in magnitude up to 8.2 Å and then dropped as outer mouth size was further increased to 25.9 Å.

The case $R_1 = R_2$ = 6.2 Å showed highest F_X magnitudes in the right mouth (Fig. 4.S1C). F_X decreased as the outer mouth size was increased. In pores with R_2 = 12.2 Å (Fig. 4.S2C), F_X showed less variation than that in R_2 = 6.2 Å. A narrow inner mouth caused more variations in F_X in the left and right mouths (Fig. 4.S1C) while a wide mouth created notable F_X variations in the vestibule (Fig. 4.S2C). Furthermore, in narrow mouthed pores, F_X in the left mouth rose up to R_1 = 15.8 Å and then dropped with increasing R_1. In the wide mouthed pore, F_X in the vestibule had almost a linear rise with increasing R_1.

4.4.1.2 Inner mouth variation in conical mouthed pores (22.5-R_2-R_2-22.5)

Simulation data were selected and arranged for R_1 = 22.5 Å and varying inner mouth size of R_2 = 6.2 Å to 12.2 Å (Fig. 4.S3). LY flux exhibited a nonlinear rise with increasing inner mouth size (Fig. 4.S3A). P_{dX} remained almost the same up to the initial section of the left mouth (Fig. 4.S3B). Pronounced variation among the varying inner mouth size conditions was observed closer to the inner mouth and the right of that region. Variations were amplified at the inner mouth regions on both sides of the vestibule. F_X in the left mouth and vestibule were negative and most distinct. While F_X magnitude dropped with increased R_2, it rose in the vestibule. Increasing R_2 did not generate noticeable variations in F_X in cell 2.

4.4.1.3 Cylindrical mouthed pores (R_1-R_2-R_2-R_1)

Figure 4.S4 summarizes results from flux simulations with cylindrical pores (R_1 = R_2) where the cylinder size was increased from 6.2 Å to 12.2 Å. The complete pore with $R_1 = R_2$ value of 12.2 Å was almost a cylinder as the elliptical vestibule almost disappears (bottom right corner of Fig. 4.S4A). LY flux rose nonlinearly with increasing pore mouth size (Fig. 4.S4A). P_{dX} profiles of the different pore sizes ran parallel in the left and right mouth sections (Fig. 4.S4B). Vestibular sections of the P_{dX} profile straightened with increase in cylinder radius. As before, the probability profile followed the pore-section in the logarithmic scale. At 12.2 Å, the particle probability was almost a straight line with no elliptical bump at the vestibule region. The left mouth and right mouth had the most pronounced F_X magnitudes (Fig. 4.S4C). F_X was negative in all cases, except in the right

mouth for cylinder radius of 6.2 Å. In the left mouth, F_X linearly decreased with increasing cylinder radius. F_X magnitudes in cell 1 were marginal. In cell 2, the differences in F_X for different cylinder radii were marginal.

4.4.2 Flux simulations in heterotypic pores

4.4.2.1 Varying outer mouth size of conical section (R_1-9.2-9.2-9.2)

Increasing the outer mouth side of the conical section marginally changed LY flux in the cone to cylinder direction (blue bars in Fig. 4.2A). However, LY flux in the cylinder to cone direction rose (orange bars in Fig. 4.2A). This caused an increase in the difference between the fluxes in the two direction as R_1 was increased. This contributed to an increase in flux ratio, which shows a gentle rise with increasing R_1 (grey bars in Fig. 4.2A). The cone with the widest mouth showed the highest asymmetry (R_1 = 25.9 Å).

As in homotypic pores, the P_{dX} profiles varied primarily due to the differences in pore shapes and the differences were most prominent in the section where size was varied. The differences were most prominent in the conical mouth in either direction (Fig. 4.2B and C). In the cone to cylindrical mouth simulations, P_{dX} levels in the left mouth were seen to drop in the left mouth as R_1 was reduced (Fig. 4.2B). In the remaining pore (vestibule and right mouth), the P_{dX} profiles were of the same shape and in the same order of magnitude. In the cylinder to conical direction simulations (Fig. 4.2C), the P_{dX} levels began to notably vary from the end of the left mouth (end of conical mouth) itself. Particle probabilities were higher in the vestibule for smaller values of R_1 and declined as R_1 was increased. This trend was reversed in the center region of the right mouth (right mouth section in Fig. 4.2C).

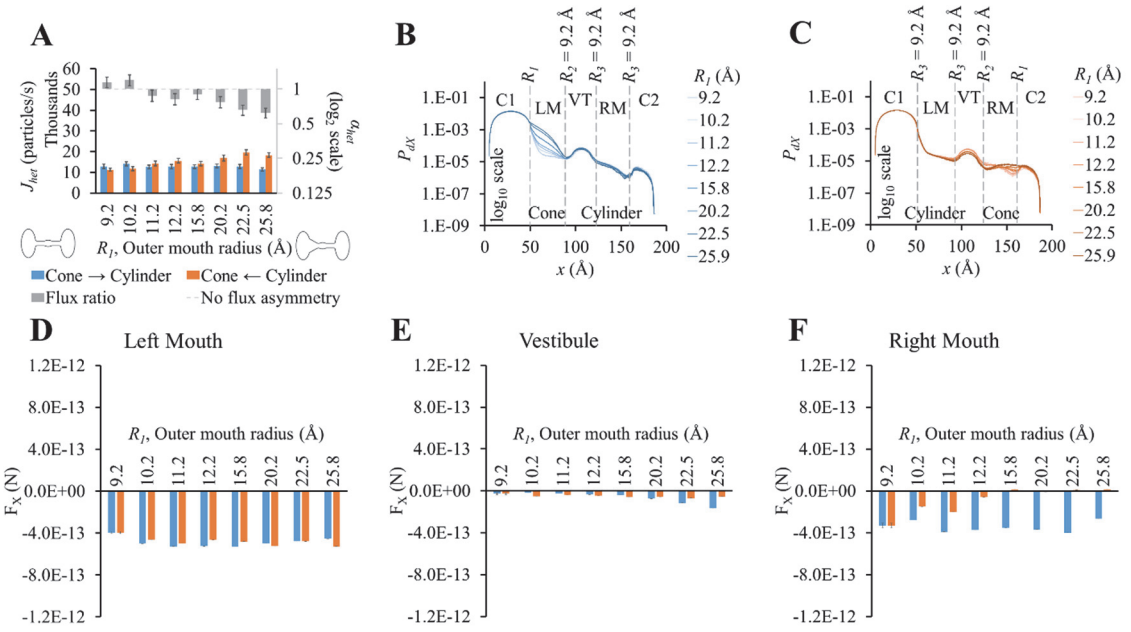

Figure 4.2 – Properties of heterotypic pores with varying outer mouth size of conical section (R_1-9.2-9.2-9.2). (A) LY fluxes and flux ratios simulated with constant concentration gradient of 2LY + 4Cs in cone to cylinder (blue bars) and cylinder to cone (orange bars) directions. The difference between $J_{het,1}$ and $J_{het,2}$ increased with larger conical mouth size. LY flux asymmetry increased with increasing outer mouth size of the conical section. (B-C) P_{dX} profiles in simulation (B) cone to cylinder direction and (C) cylinder to cone direction. (D-F) Average force per LY particle in (D) the left mouth, (E) the vestibule and (F) the right mouth. F_X was in the -x direction in all sections of the pore. (D) F_X magnitudes in the left mouth in either direction were almost equal for different pore mouth sizes. (E) F_X magnitudes in the vestibule rose in the cone to cylinder direction with increase in R_1. (F) The right mouth had high differences in F_X magnitudes between the two directions with F_X magnitude dropping with increasing R_1 in the cylinder to cone direction.

As in homotypic pores, F_X in cell 1 was marginal compared to F_X in other pore sections (Fig. 4.S1A-E). The left (Fig. 4.2D) and right (Fig. 4.2F) mouth had high F_X values. F_X values were negative throughout the pore in simulations of both direction. The left mouth F_X differences between either directions were marginal for all cases. F_X in the vestibule (Fig. 4.2D), though small in magnitude, showed a widening difference between the 2 directional fluxes as R_1 was increased with F_X in the cone to cylinder direction being larger (Fig. 4.2E). Differences in F_X magnitudes were high in the right mouth (Fig. 4.2F).

4.4.2.2 Varying inner mouth size of conical section (22.5-R_2-9.2-9.2)

Flux values rose with increasing inner mouth size in both directions (blue and orange bars in Fig. 4.3A). Difference in flux in either direction seemed to fluctuate as R_2 was increased. This random variation was clear in the flux ratios which varied from ~0.7 to 1 (grey bars in Fig. 4.3A). A clear dependence of R_2 on flux asymmetry was absent with

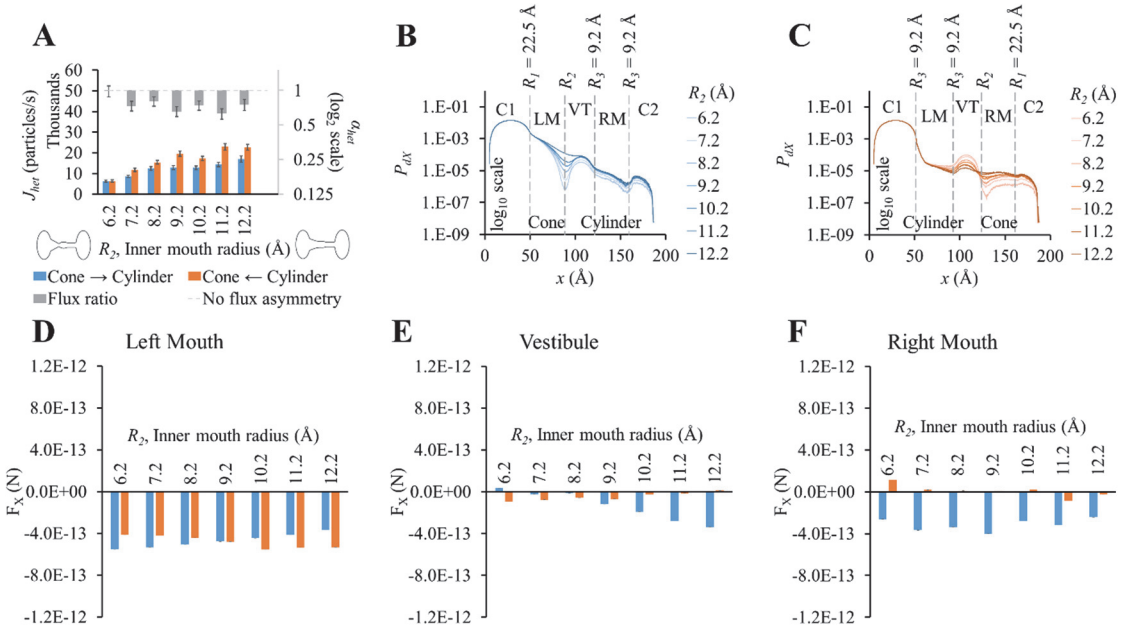

Figure 4.3 – Properties of heterotypic pores with varying inner mouth size of conical section (22.5-R_2-9.2-9.2). (A) LY fluxes rose in both directions with increasing inner mouth size (only R_2). Differences between $J_{het,1}$ and $J_{het,2}$ vary amongst the different cases. LY flux ratio variations were random with increasing R_2 with maximum flux asymmetry at R_2 = 9.2 Å and 11.2 Å. (B) P_{dX} in cone to cylinder direction dropped near R_2 and maintained almost a uniform difference amongst the different inner pore mouth sizes. (C) P_{dX} in the cylinder to cone direction decreased in the left mouth and vestibule with increasing R_2. This tendency flipped by the end of the vestibule with P_{dX} levels increased with increase in R_2 in the right mouth. (D-F) Average force per LY particle in (D) the left mouth, (E) the vestibule and (F) the right mouth. (D) Increase in R_2 caused F_X magnitudes (-x direction) in the left mouth to gently decrease in the cone to cylinder direction, while gently rise in the cylinder to cone direction. (E) In the vestibule, F_X increased in the cone to cylinder direction, and decreasing in the cylinder to cone direction with increasing in R_2. (F) F_X magnitudes in the cone to cylinder direction were negative and varied randomly in the right mouth.

maximum flux asymmetry at R_2 = 9.2 Å and 11.2 Å and no flux asymmetry seen at R_2 = 6.2 Å.

Particle probability profiles pointed to the vestibular mouth (at R_2 or end of conical mouth) as the main source of P_{dX} variation in the cone to cylinder direction (Fig. 4.3B). This order of difference in magnitude due to varying R_2 was maintained in the remaining pore profile. The P_{dX} profiles in the cylinder to cone direction exhibited different variations (Fig. 4.3C). While P_{dX} remained in the same order up to the vestibule mouth (or end of the cylinder mouth), it was highest for R_2 = 6.2 Å and lowest for R_2 = 12.2 Å in the vestibule region. By the end of the vestibule (smaller end of the conical mouth), this trend was inversed and P_{dX} dropped along x with lowest levels at R_2 = 6.2 Å and highest at R_2 = 12.2 Å in the region and the remaining right mouth (conical section).

F_X differences between the two directions were pronounced in the vestibule (Fig. 4.3E) and right mouth (Fig. 4.3F) with higher F_X against the flux (negative) in the cone to cylinder direction. This rose in the cone to cylinder direction with increasing R_2 in the vestibule (blue bars in Fig. 4.3E). The variation in F_X in the right mouth was random. In the left mouth, F_X magnitude (in -x direction) in the cone to cylinder direction fell, while rising in the cylinder to cone direction as R_2 is increased (Fig. 4.3D). In general, the net electrical force acting against the direction of flux was more in the cone to cylinder direction than in the cylinder to cone direction.

4.4.2.3 Varying cylindrical mouth size (22.5-9.2-R_3-R_3)

Fluxes rose with increased cylinder mouth size in both directions (blue and orange bars in Fig. 4.4A). Flux ratio, on the other hand, followed a bell curve with its maxima at

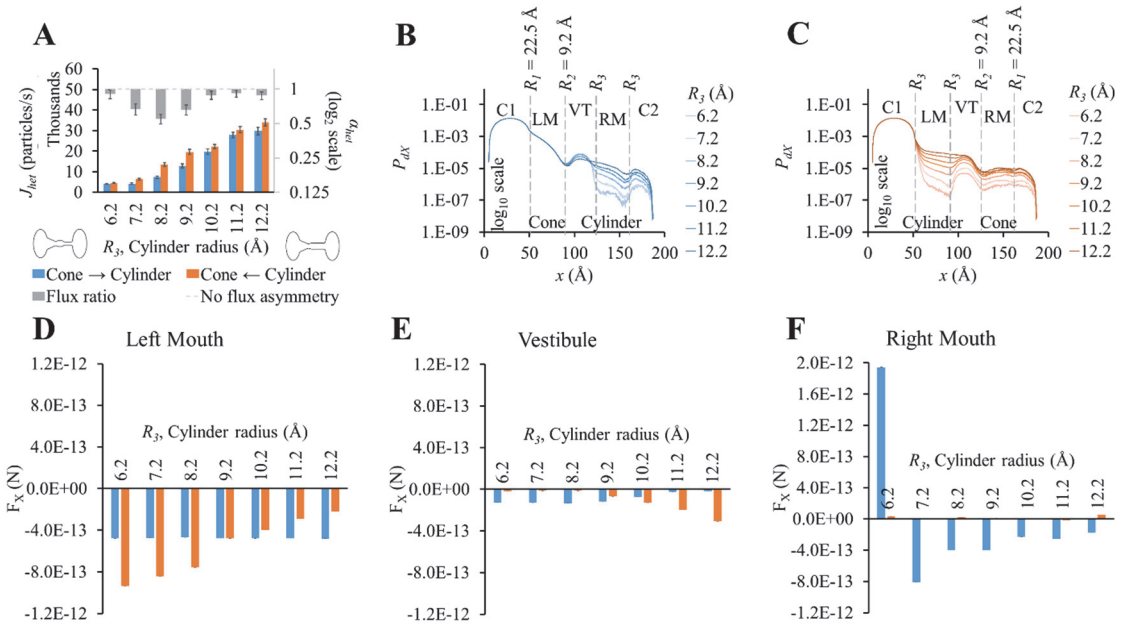

Figure 4.4 – Properties of heterotypic pores with varying cylindrical mouth size (22.5-9.2-R_3-R_3). (A) LY fluxes increased in both directions as the cylinder section was widened. LY flux ratio rose and then dropped with increasing cylinder mouth size with a maxima at R_3 = 8.2 Å. (B) P_{dX} levels remained in the same order up to the mouth of the vestibule in cone to cylinder direction for the different cylinder mouth sizes. Probability profiles almost ran parallel from there on for all cases with probability levels proportional to R_3. (C) P_{dX} levels dropped at the beginning of the cylindrical mouth (left mouth) and mimicked the pore profile up to the vestibule, after which they gently rose. Profiles for different cylinder sizes ran almost parallel. (D-F) Average force per LY particle in (D) the left mouth, (E) the vestibule and (F) the right mouth. (E) In the cone to cylinder direction, F_X in the left mouth was marginally affected by an increase in the cylinder mouth size. In the cylinder to cone direction though, F_X dropped as the cylindrical mouth was widened. (F) In the vestibule, F_X gently dropped in the cone to cylinder direction while rising in the cylinder to cone direction with widening cylindrical mouth.

~7.2 Å and 9.2 Å.

There were no noticeable differences in P_{dX} along x up to the vestibule (or end of the conical mouth) with varying cylinder size in the cone to cylinder direction (Fig. 4.4B). In the vestibule, P_{dX} was inversely proportional to the cylinder radius with smaller cylinders having P_{dX} profiles an order of magnitude higher than the widest cylinder. In the right mouth, P_{dX} levels dropped gently and were proportional to the cylinder radius with P_{dX}

profiles parallel to each other. On the other hand, in cylinder to cone direction simulations, P_{dX} profiles (Fig. 4.4C) varied from the beginning of the cylindrical mouth to the end of the pore with P_{dX} values almost maintaining contoured profiles to each other with P_{dX} levels proportional to the cylinder mouth size.

F_X was negative or marginal in all cases and sections except for R_3 = 6.2 Å in the cylinder mouth (right mouth, Fig. 4.4F) in the cone to cylinder direction. As R_3 was increased, F_X dropped in the cylinder to cone direction while remaining almost constant in the cone to cylinder direction. In the vestibule, F_X remained constant up to R_3 = 8.2 Å and then decreased with widening cylinder mouth in the cone to cylinder direction (blue bars in Fig. 4.4E). A similar trend was seen in the cylinder to cone direction where F_X remained almost the same up to R_3 = 8.2 Å, but then rose with widening of the cylindrical mouth (orange bars in Fig. 4.4E). In the right mouth, while F_X remained marginal in the cylinder to cone direction, it dropped with increasing R_3 from 7.2 Å to 12.2 Å (Fig. 4.4F). We looked at differences in F_X amongst the two flux directions and found that the F_X difference reversed in the left mouth and vestibule after R_3 = 9.2 Å.

4.4.2.4 Varying cylindrical mouth size in pore with wide conical mouth (25.9-12.2-R_3-R_3)

Results were similar to those with pore profile of 22.5-9.2-R_3-R_3 (Fig. 4.5A). Fluxes rose with wider cylinder mouth and flux ratio was seen to maximize at R_3 = 8.2 Å. Maximum LY flux asymmetry (0.49) was slightly higher than observed in 22.5-9.2-R_3-R_3 simulations (0.55).

P_{dX} profiles (Fig. 4.5B and C) and variations amongst different cylinder sizes were

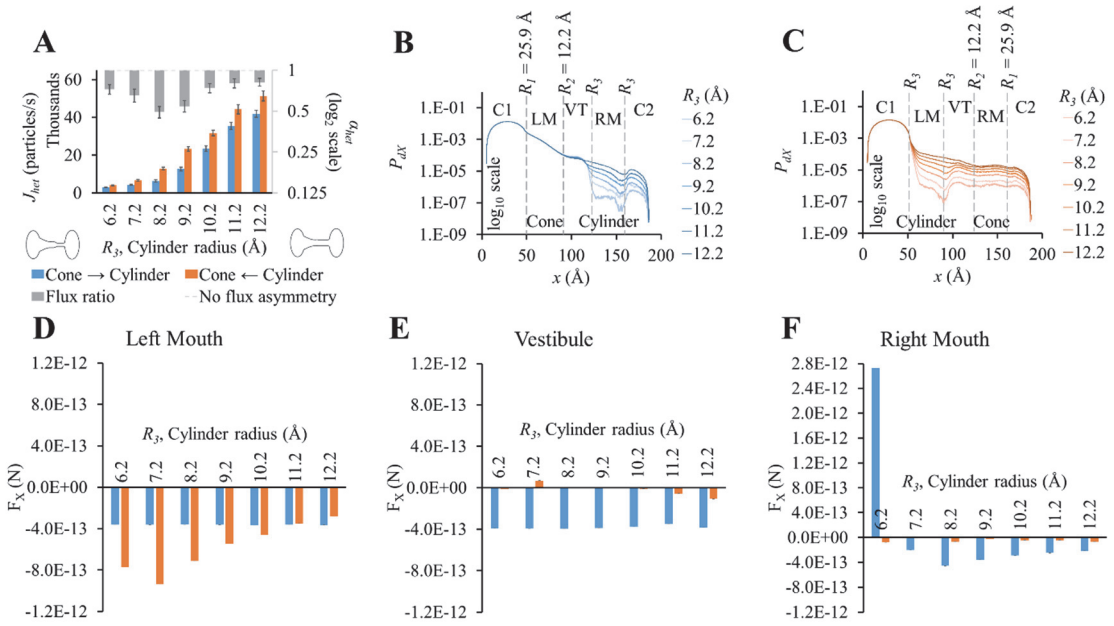

Figure 4.5 – Properties of heterotypic pores with wide conical mouth and varying cylindrical mouth size (25.9-12.2-R_3-R_3). (A) LY fluxes rose in both directions with increasing cylinder size. Fluxes in cone to cylinder were always smaller than in cylinder to cone direction for all cylindrical section sizes. LY flux ratios vary nonlinearly with cylinder mouth size with maximum flux asymmetry at R_3 = 8.2 Å. (B-C) P_{dX} profiles in simulations with concentration gradient in (B) cone to cylinder and (C) cylinder to cone direction. P_{dX} profile variations were similar to those seen in the 22.5-9.2-R_3-R_3 simulations. (D-F) Average force per LY particle in (D) the left mouth, (E) the vestibule and (F) the right mouth. F_X in the left mouth and vestibule in the cone to cylinder simulations remained constant with increasing cylinder size. In the left mouth (D), F_X magnitude in cylinder to cone direction varied nonlinearly with a maxima at R_3 = 7.2 Å.

also similar to those for 22.5-9.2-R_3-R_3, with the profiles showing pronounced differences starting from the end of the vestibule in the cone to cylinder direction and beginning of the cylinder mouth in the cylinder to cone direction. Since a wider conical mouth was used, the drop in P_{dX} along x at the beginning and end of the conical mouth was smaller than seen in 22.5-9.2-R_3-R_3 (Fig. 4.5C versus Fig. 4.4C).

While P_{dX} variations were similar to those in the previous pore-shape case (22.5-9.2-R_3-R_3), F_X variations were notably different. F_X in the cone to cylinder direction remained almost constant in the left mouth (Fig. 4.5D) and vestibule (Fig. 4.5E) with

increasing cylinder mouth size. In the right mouth, F_X was positive at R_3 = 6.2 Å and then dropped and became negative at R_3 = 7.2 Å, reaching minima at R_3 = 8.2 Å and then rising again up to R_3 = 12.2 Å (Fig. 4.5F). On the other hand, F_X magnitudes in the cylinder to cone direction were marginal in the vestibule and right mouth. In the left mouth, it increased up to R_3 = 7.2 Å and then dropped, while being greater in magnitude to its corresponding cone to cylinder direction up to R_3 = 11.2 Å (Fig. 4.5D). While in the left mouth, the force against the flux (negative F_X) was higher in the cylinder to cone direction (R_3 = 6.2 Å to 10.2 Å), it was higher in the cone to cylinder direction in the vestibule and right mouth (R_3 = 7.2 Å to 12.2 Å).

From all different heterotypic shapes studied, a pore-profile of 25.9-12.2-8.2-8.2 yielded maximum LY flux asymmetry with flux ratio of ~0.49. Flux ratio of the homotypic pores of the left and right hemichannels was ~9.18.

4.4.3 Influence of particle size on flux asymmetry in heterotypic pores

We studied a heterotypic pore profile of 25.9-12.2-8.2-8.2. As expected, fluxes dropped as particle size was increased (Fig. 4.6A). Fluxes were higher in the cylinder to cone direction (orange bars in Fig. 4.6A). Flux ratio was maximal for r_p = 4.9 Å, which is the Stokes radius of LY. Even though the flux ratio dropped on either side of r_p = 4.9 Å, the flux asymmetry was still pronounced (~0.7).

The general P_{dX} profile remained the same for all particle sizes in their respective direction of flux simulations (Fig. 4.6B-C). The net drop in P_{dX} across the pore was directly

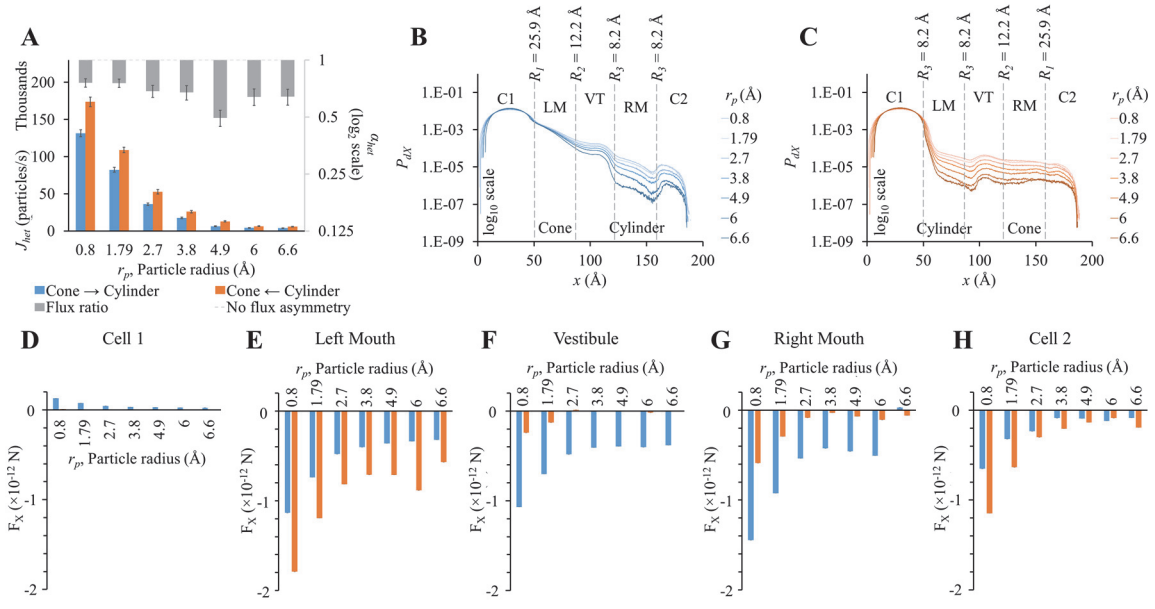

Figure 4.6 – Role of particle size on flux asymmetry in heterotypic pores. Simulation results in heterotypic pore with profile 25.9-12.2-8.2-8.2 with constant concentration gradient, 2mV transjunctional voltage and $2e^-$ particle charge. (A) Particle fluxes dropped nonlinearly as particle radius was increased from 0.8 Å to 6.6 Å. Flux ratio values (grey bars) ranged from ~0.5 to 0.8. Maximum asymmetry of 0.51 was for particle size of 4.9 Å. (B-C) P_{dX} levels remain in the same order in cell 1. P_{dX} profiles were similar to the pore profiles (log 10 scale). (D-H) F_X in the different sections of the cell-pore-cell system. (D) F_X values in cell 1 were marginal compared to other sections. In general, F_X magnitudes dropped in all sections of the pore with increasing particle size. (E) In the left mouth, F_X dropped with increasing particle sizes with F_X in cylinder to cone direction were higher than the cone to cylinder direction for all cases. F_X for r_p = 6 Å in the cylinder to cone direction was unexpectedly high. (F-G) In the vestibule and right mouth, F_X was negative and distinctly higher in the cone to cylinder direction than in the cylinder to cone direction. (H) F_X magnitudes in cell 2 were larger in the cylinder to cone direction in all cases.

proportional to the particle size in both directions. In cell 1, P_{dX} remained in the same order of magnitude. The maximum difference in P_{dX} among different r_p values was seen at the narrowest section of the pore. This includes the mouths on either side of the vestibule and the cylindrical mouth.

In general, F_X magnitudes dropped nonlinearly with increasing particle size (Fig. 4.6D-H). Cell 1 magnitudes in the cone to cylinder direction became more distinct at

smaller particle size of r_p = 0.8 Å to 2.7 Å, with a trend of F_X magnitudes dropping with increasing particle size (Fig. 4.6D). F_X magnitudes in the cone to cylinder direction reduced with increasing particle size and saturated around r_p = 4.9 Å to 6 Å in the left mouth (Fig. 4.6E) and vestibule (Fig. 4.6F). In the left and right mouth, r_p = 6 Å showed small rise in F_X (Fig. 4.6E and Fig. 4.6G). In the left mouth, F_X magnitude was always higher in the cylinder to cone direction (Fig. 4.6E). On the other hand, F_X magnitudes were always higher in the cone to cylinder direction in the vestibule (Fig. 4.6F) and right mouth (Fig. 4.6G).

4.4.4 Influence of particle charge on flux asymmetry in heterotypic pores

Particle flux reduced with increased particle charge in either direction (Fig. 4.7A). Flux ratio, on the other hand, increases and seems to reach a maxima at $q_p = 2e^-$ (grey bars in Fig. 4.7A).

P_{dX} profiles (Fig. 4.7B-C) were similar to the general ones seen before in the previous cases. The higher the particle charge, the lower was the P_{dX} level.

Since at zero charge there were no electrical forces as interparticle electrostatic forces and applied transjunctional voltage were absent, F_X for $0e^-$ have not been present in sectional F_X figures (Fig. 4.7D-H). F_X differences between the two directions rose with increasing negative charge. F_X in cell 1 was marginal in magnitude compared to F_X in other sections. In the left mouth, F_X was negative and distinctly higher in the cylinder to cone direction than cone to cylinder direction for $q_p > 1e^-$ (Fig. 4.7E). In the vestibule (Fig. 4.7F) and right mouth (Fig. 4.7G), it was the other way round with F_X larger in the cone to

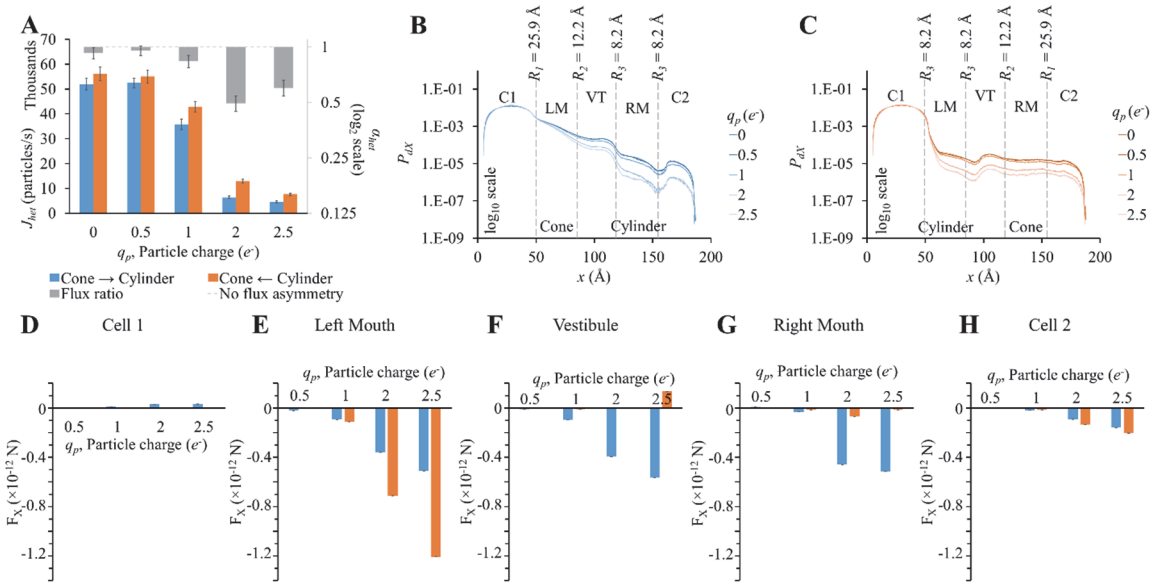

Figure 4.7 – Role of particle charge on flux asymmetry in heterotypic pores. (A) Particle fluxes decreased with increasing particle charge. Flux ratio (grey bars) also rose up to $q_p = 2e^-$. (B-C) The P_{dX} profiles were similar in shape but scaled down for high particle charge. (D-H) F_X variation patterns for different q_p were similar in the different sections, but the differences between the 2 directions were magnified with increasing q_p. (D) F_X magnitudes in cell 1 were marginal compared to F_X in other sections. (E) In the left mouth, F_X was negative in the cylinder to cone direction and larger in magnitude. (F-G) In the vestibule and right mouth, F_X were larger in the cone to cylinder direction. (H) F_X in cell 2 were small and differences between the two directions were marginal.

cylinder direction.

4.5 Discussions

4.5.1 Flux asymmetry and heterotypic pores that best fit Cx43-Cx45 *in vitro* data

Our simulations with heterotypic pores revealed the maximal possible flux asymmetry due to pore shape. We found that flux asymmetry was directly proportional to the width of the conical section from our R_1-9.2-9.2-9.2 results in Fig. 4.2A. Also we found that a constant cylindrical mouth section of $R_3 = 8.2$ Å yielded the highest flux asymmetry,

as shown in our flux simulation on heterotypic pores for 2 different cone mouth sizes of 22.5-9.2-R_3-R_3 (Fig. 4.4A) and 25.9-12.2-R_3-R_3 (Fig. 4.5A). Our previously published *in vitro* data with Cx43-Cx45 reported α_{het} = 0.34 and corresponding α_{hom} = 3.88 with Cx43 as the left hemichannel (red in Fig. 4.1C-D) and Cx45 as the right hemichannel (white in Fig. 4.1C-D) in the heterotypic junctions. The *in silico* flux data for heterotypic pore profile of 22.5-9.2-8.2-8.2 (S# 18 in Table 4.S2) was identified to best fit these data points with α_{het} = 0.55 and α_{hom} = 3.38. This certainly makes a strong case where *in vitro* data could be explained by pore shape variation to a very significant degree. Perhaps a finer optimization might yield exactly matching data. Another close candidate from our simulations was 25.9-12.2-9.2-9.2 (S# 26 in Table 4.S2) with α_{het} = 0.54 and α_{hom} = 4.98.

Heterotypic pore profile of 25.9-12.2-8.2-8.2 gave maximal flux asymmetry with α_{het} = 0.49, but the corresponding α_{hom} = 9.18. This was one of the highest magnitudes of preferential flux reversals (i.e., $\alpha_{het} < 1$ and $\alpha_{hom} > 1$ or vice versa) between the heterotypic pore and the homotypic pores of the hemichannels. Considering α_{het} to 0.75 to be a threshold for significant flux asymmetry, from the 28 heterotypic pores, 14 exhibited flux asymmetry (Table 4.S2). Out of those 14, 13 had preferential flux reversal between the heterotypic and their homotypic counterparts (comparing α_{het} and α_{hom} columns in Table 4.S2).

4.5.2 Flux asymmetry was established by pore shape while scaled by particle charge and size

We conducted separate simulations for studying the effect of pore sectional radius in heterotypic pores, particle size and charge on flux asymmetry. We first identified the

radii combination that yielded the maximum flux asymmetry (25.9-12.2-8.2-8.2) and performed the particle size and charge studies using this heterotypic pore to maximize sensitivity. In our previous work, we established that particle charge was a vital element toward creating asymmetric fluxes and this asymmetry disappeared when charge was removed. Our results in this work indicate that while charge is vital, it acts as a scaling factor to flux asymmetry, where it increases with rising charge magnitude to about $q_p = 2e^-$ (Fig. 4.7A). Particle size seems to play a similar role, though there was no clear relationship between particle size and flux asymmetry. In fact, flux asymmetry was present for all particle sizes considered with maximal asymmetry at r_p = 4.9 Å (Fig. 4.6A). We note that even though charge was a vital factor, the flux asymmetry was purely regulated by the pore shape. Variation of different aspects of the pore-shape in heterotypic pores had strong effects on flux asymmetry. The pore shape features governed the direction and magnitude of asymmetry. Flux asymmetry was directly proportional to the outer mouth size of conical section R_1 (Fig. 4.2A), nonlinearly dependent on the cylinder mouth size R_3 (Fig. 4.4A and 4.5A) and varied randomly with inner pore mouth size R_2 (Fig. 4.3A). As noted earlier, only half the heterotypic pores exhibited flux asymmetry with charged particles (Table 4.S2). From our results, we conclude that flux asymmetry was primarily regulated by the heterotypic pore's conical and cylinder mouth sizes. Particle charge and size were secondary factors.

4.5.3 Predicting flux and flux asymmetry in heterotypic pores from sectional particle probabilities and electrical forces

In our previous work, we suggested a mechanism in which the pore shape controlled the distance between particles in a pore and the charge cloud at the end of the pore (cell 1 in our simulations). A wider or conical mouth pore section allowed this charge cloud to invade into the conical section of the pore, reducing the distance between the charged cloud and any particle that got into the pore, thus increasing the pull-out (in -*x* direction) electrical force. When the charge cloud was placed on the narrower mouth side, it maintained a higher distance and thus a lower pull-out electrical force. While the underlying mechanism remains the same, particle probability distribution also plays a key role and flux regulation cannot be solely explained based on sectional force differences. Particle probability profiles across the pore were analogous to concentration gradient. P_{dX} profiles in all cases tend to resemble concentration gradients we would expect in simple diffusion through those pore shapes, but in exponential scale. The narrowness of the pore amplified the drop in probability (or concentration) along *x*. The smaller the pore section size, the higher was the drop in P_{dX} across the section and vice versa. This trend in P_{dX} was particularly consequential in the narrowest sectional pore radii (R_1, R_2 and R_3 = 6.2 Å) in homotypic (Fig. 4.S1B, R_2 = 6.2 Å in Fig. 4.S3B and $R_1 = R_2$ = 6.2 Å in Fig. 4.S4B) and heterotypic (R_2 = 6.2 Å in Fig. 4.3B-C, R_3 = 6.2 Å in Fig. 4.4B-C and Fig. 4.5B-C) pores. Such drops caused major variations in net charge distribution, leading to the electrical force distribution across the pore. An extreme example of this can be seen in right mouth F_X data for R_3 = 6.2 Å in 22.5-9.2-R_3-R_3 (Fig. 4.4F) and 25.9-12.2-R_3-R_3 (Fig. 4.5F) where F_X were positive with very high magnitudes in the cone to cylinder direction (negative for all other

cases in the same direction). This implied large flux as LY particles were pushed out of the pore in the direction of flux. But, because the right mouth has the lowest P_{dX} level (R_3 = 6.2 Å in the right mouth section in Fig. 4.4B and Fig. 4.5B), there were few particles to push out. So if any particles ended up in the right mouth, they moved out from the pore to cell 2 quicker than in other pore shapes. This eluded a simple relationship to explain or predict accurately why maximum flux asymmetry occurs at 25.9-12.2-8.2-8.2. Even heterotypic pores with no flux asymmetry showed pronounced F_X differences amongst each other (R_2 = 6.2 Å in Fig. 4.3A, D-F and R_3 = 10.2 Å to 11.2 Å in Fig. 4.4A, D-F). As of now, the best way to select sections for F_X values consequential to flux is to consider them in order of their distance from cell 1 where the particle probability was the highest. Following this criterion, the left mouth and vestibule F_X were most consequential. The right mouth might or might not be significant based on relative P_{dX} levels in the right mouth and sections to the right of it. We presented only the F_X values for the left mouth, vestibule and right mouth for our heterotypic pore studies here. F_X in cell 1 and cell 2 (along with others) have been presented in the supplemental section (Fig. 4.S5). F_X magnitudes in cell 1 were marginal compared to other sections. Though F_X magnitudes were pronounced in cell 2, and they had minimal effect on final flux value as they had the minimal P_{dX} levels in the pore.

4.5.4 Possible role of heterotypic Cx43-Cx45 gap junctions in cardiac disease

Molecular permeability of biological molecules in gap junction has been extensively studied for key functional cytoplasmic molecules, including secondary

messengers like IP_3, cAMP, cGMP and Ca^{2+} [35]–[39], [53], nucleotides like RNA and siRNA [34], and glucose and its metabolites like ATP, ADP and glutamate [32], [33]. These studies reported 3 to 33 fold differences in permeabilities between different molecules in different connexin types. Our *in vitro* studies focused on homotypic and heterotypic pores formed out of Cx43 and Cx45: connexin pores present in the heart. While Cx43 predominates in the ventricular myocytes, in diseased or failing human ventricles, Cx43 expression decreases while that of Cx45 increases [54], potentially leading to a rise in heterotypic Cx43-Cx45 junctions. Such heterotypic junctions not only increase impedance to conduction in the ventricles, but can also cause functional effect by creating concentration imbalances of secondary messengers like Ca^{2+} and IP_3 through asymmetric fluxes amongst neighboring myocytes. Such imbalances can create disruptions in excitation contraction coupling. Moreover, such Cx combinations can cause variations in glucose availability among neighboring cells, which can hinder ATP production. Furthermore, ventricular fibrosis [55] may cause coupling of myocytes to Cx45 expressing non-myocytes: fibroblast [56] and myofibroblasts [57]. Fibroblasts being 20 to 40 times smaller in volume than myocytes would be more easily able to create changes in the transjunctional (Cx43-Cx45) concentration gradient, leading to higher concentration of certain molecules in the myocyte (assuming Cx43 is conical and Cx45 is cylindrical as per our simulation results). This remains to be demonstrated in further studies.

4.5.5 Limitations

Our model was primarily optimized for studying LY fluxes in gap junction pores mimicking *in vitro* LY dye diffusion under double whole cell voltage clamp experiments.

Most of our simulation data reported here were for LY particles with Cs counter-ions. Our simulations on particle size and charge variation deviated from this and faced limits due to computational and statistical limits. We allowed a maximal simulation time of 500 μs or the time when the fluxes in the last 5 values had less than 5% standard deviation. These were set taking into consideration the computational resources available, computation time per simulation and the number of different simulation conditions in our studies. This provided limitations to the smallest measurable flux in our model and restricted the minimum pore mouth size to 6.2 Å, maximum particle size to 6.6 Å and maximum particle charge to $2.5e^-$. Going beyond these limits either gave us a considerable number of simulations not reaching the 5% standard deviation criteria or just 0 flux values. Therefore, for parameters leading to lower fluxes, the standard deviation limit will need to be reduced to a lower threshold or the simulation time gap between the points considered for standard deviation would have to be increased.

4.6 Conclusions

Our investigations shed light on the role of pore shape and particle charge in observed flux asymmetry of large molecules in inactive heterotypic pores. In particular, we identified pore shapes that match *in vitro* data to a considerable degree. We found the pore shape of radius profile 25.9-12.2-8.2-8.2 produced the maximal flux asymmetry of 0.49. The pore shape came out as the key regulator of flux asymmetry. Flux asymmetry existed irrespective of particle size. Though particle charge was vital, it merely scaled the asymmetry up to a certain magnitude. It is important to note that such asymmetry is possible only in this nano-scale and it will disappear on enlarging the pore. The studies did

not reveal a simple relationship for explaining flux asymmetry based on pore-shape, particle charge and size, but we identified factors that aid in predicting such events.

Our work provides a solid foundation to investigate flux symmetry of biologically relevant molecules like ATP and IP_3, which have major metabolic consequences to cell function. We envision that the conclusions from our *in silico* results will inspire future *in vitro* studies to demonstrate the role of such preferential fluxes in physiological and pathological conditions of cardiac or other tissues.

4.7 Acknowledgement

We acknowledge funding for this work from the Nora Eccles Treadwell Foundation (APM) and NIH R01 R01-63969 (APM). We would like to thank Haonan Yang, Nancy Allen and Dr. Phil Ershler for their computer support at CVRTI.

4.8 Authorship

AM developed the simulation model, managed and processed the data and prepared the results. AM prepared the initial draft of the manuscript and implemented corrections and suggestions towards the final draft of the manuscript. APM was the principal investigator and supervised in designing and executing the research. FBS and APM provided advice during data analysis and reviewed the manuscript. FBS also provided computational resources for this research.

4.9 References

[1] S. Goran and K. Willecke, “Gap junctions and the connexin protein family,” *Cardiovasc. Res.*, vol. 62, no. 2, pp. 228–232, 2004.

[2] J. H. Xia *et al.*, “Mutations in the gene encoding gap junction protein beta-3 associated with autosomal dominant hearing impairment.,” *Nat. Genet.*, vol. 20, no. 4, pp. 370–3, Dec. 1998.

[3] B. Uhlenberg *et al.*, “Mutations in the gene encoding gap junction protein alpha 12 (connexin 46.6) cause Pelizaeus-Merzbacher-like disease,” *Am. J. Hum. Genet.*, vol. 75, no. 2, pp. 251–260, 2004.

[4] H. J. Jongsma and R. Wilders, “Gap Junctions in Cardiovascular Disease,” *Circ. Res.*, vol. 86, no. 12, 2000.

[5] D. C. Spray and R. Dermietzel, “X-linked dominant Charcot—Marie—Tooth disease and other potential gap-junction diseases of the nervous system,” *Trends in Neurosciences*, vol. 18, no. 6. pp. 256–262, 1995.

[6] D. P. Kelsell *et al.*, “Connexin 26 mutations in hereditary non-syndromic sensorineural deafness,” *Nature*, vol. 387, no. 6628, pp. 80–83, May 1997.

[7] V. M. Unger, N. M. Kumar, N. B. Gilula, and M. Yeager, “Three-dimensional structure of a recombinant gap junction membrane channel,” *Science*, vol. 283, no. 5405, pp. 1176–1180, 1999.

[8] S. Maeda *et al.*, “Structure of the connexin 26 gap junction channel at 3.5 A resolution,” *Nature*, vol. 458, no. 7238, pp. 597–602, Apr. 2009.

[9] T. W. Allen, M. Hoyles, S. Kuyucak, and S. H. Chung, “Molecular and Brownian dynamics study of ion selectivity and conductivity in the potassium channel,” *Chem. Phys. Lett.*, vol. 313, no. 1–2, pp. 358–365, 1999.

[10] S. H. Chung, T. W. Allen, and S. Kuyucak, “Modeling diverse range of potassium channels with Brownian dynamics,” *Biophys. J.*, vol. 83, no. 1, pp. 263–277, 2002.

[11] T. Vora, B. Corry, and S. H. Chung, “Brownian dynamics study of flux ratios in sodium channels,” *Eur. Biophys. J.*, vol. 38, no. 1, pp. 45–52, Nov. 2008.

[12] B. Corry, T. W. Allen, S. Kuyucak, and S. H. Chung, “Mechanisms of permeation and selectivity in calcium channels,” *Biophys. J.*, vol. 80, no. 1, pp. 195–214, 2001.

[13] W. Im and B. Roux, “Ion permeation and selectivity of OmpF porin: A theoretical study based on molecular dynamics, Brownian dynamics, and continuum electrodiffusion theory,” *J. Mol. Biol.*, vol. 322, no. 4, pp. 851–869, 2002.

[14] T. Schirmer and P. S. Phale, “Brownian dynamics simulation of ion flow through porin channels,” *J. Mol. Biol.*, vol. 294, no. 5, pp. 1159–1167, 1999.

[15] K. Il Lee, H. Rui, R. W. Pastor, and W. Im, “Brownian dynamics simulations of ion transport through the VDAC,” *Biophys. J.*, vol. 100, no. 3, pp. 611–619, 2011.

[16] F. Zonta, D. Buratto, C. Cassini, M. Bortolozzi, and F. Mammano, "Molecular dynamics simulations highlight structural and functional alterations in deafness related M34T mutation of connexin 26," *Front. Physiol.*, vol. 5, p. 85, Mar. 2014.

[17] T. Kwon, A. L. Harris, A. Rossi, and T. A. Bargiello, "Molecular dynamics simulations of the Cx26 hemichannel: evaluation of structural models with Brownian dynamics," *J. Gen. Physiol.*, vol. 138, no. 5, pp. 475–93, 2011.

[18] L. Dong, X. Liu, H. Li, B. M. Vertel, and L. Ebihara, "Role of the N-terminus in permeability of chicken connexin45.6 gap junctional channels," *J. Physiol.*, vol. 576, no. 3, pp. 787–799, Nov. 2006.

[19] F. Cao *et al.*, "A quantitative analysis of connexin-specific permeability differences of gap junctions expressed in HeLa transfectants and Xenopus oocytes," *J. Cell Sci.*, vol. 111, no. 1, 1998.

[20] R. Eckert, "Gap-Junctional Single-Channel Permeability for Fluorescent Tracers in Mammalian Cell Cultures," *Biophys. J.*, vol. 91, no. 2, pp. 565–579, 2006.

[21] M. Beltramello, M. Bicego, V. Piazza, C. D. Ciubotaru, F. Mammano, and P. D'Andrea, "Permeability and gating properties of human connexins 26 and 30 expressed in HeLa cells," *Biochem. Biophys. Res. Commun.*, vol. 305, no. 4, pp. 1024–1033, 2003.

[22] A. D. Martinez, V. Hayrapetyan, A. P. Moreno, and E. C. Beyer, "Connexin43 and Connexin45 Form Heteromeric Gap Junction Channels in Which Individual Components Determine Permeability and Regulation," *Circulation*, vol. 90, no. 10, pp. 1100–1107, 2002.

[23] S. W. Yum *et al.*, "Human connexin26 and connexin30 form functional heteromeric and heterotypic channels," *Am. J. Physiol. - Cell Physiol.*, vol. 293, no. 3, 2007.

[24] M. Rackauskas, V. K. Verselis, and F. F. Bukauskas, "Permeability of homotypic and heterotypic gap junction channels formed of cardiac connexins mCx30.2, Cx40, Cx43, and Cx45," *Am. J. Physiol. Heart Circ. Physiol.*, vol. 293, no. 3, pp. H1729–H1736, 2007.

[25] V. Valiunas, E. C. Beyer, and P. R. Brink, "Cardiac gap junction channels show quantitative differences in selectivity," *Circ. Res.*, vol. 91, no. 2, pp. 104–111, 2002.

[26] V. Verselis, R. White, D. Spray, and M. Bennett, "Gap junctional conductance and permeability are linearly related," *Science (80-.).*, vol. 234, no. 4775, 1986.

[27] R. D. Veenstra, "Determining ionic permeabilities of gap junction channels," in *Methods Mol Biol*, vol. 154, Springer, 2001, pp. 293–311.

[28] R. D. Veenstra, H. Z. Wang, E. C. Beyer, and P. R. Brink, "Selective dye and ionic permeability of gap junction channels formed by connexin45," *Circ. Res.*, vol. 75,

no. 3, pp. 483–90, 1994.

[29] A. L. Harris, “Connexin channel permeability to cytoplasmic molecules,” *Prog. Biophys. Mol. Biol.*, vol. 94, no. 1–2, pp. 120–143, 2007.

[30] E. C. Beyer *et al.*, “Heteromeric mixing of connexins: compatibility of partners and functional consequences,” *Cell Commun. Adhes.*, vol. 8, no. FEBRUARY, pp. 199–204, 2001.

[31] F. F. Bukauskas *et al.*, “Properties of mouse connexin 30.2 and human connexin 31.9 hemichannels: implications for atrioventricular conduction in the heart,” *Proc. Natl. Acad. Sci. U. S. A.*, vol. 103, no. 25, pp. 9726–9731, 2006.

[32] G. S. Goldberg, A. P. Moreno, and P. D. Lampe, “Gap junctions between cells expressing connexin 43 or 32 show inverse permselectivity to adenosine and ATP.,” *J. Biol. Chem.*, vol. 277, no. 39, pp. 36725–30, Sep. 2002.

[33] G. S. Goldberg, P. D. Lampe, and B. J. Nicholson, “Selective transfer of endogenous metabolites through gap junctions composed of different connexins.,” *Nat. Cell Biol.*, vol. 1, no. 7, pp. 457–459, 1999.

[34] V. Valiunas *et al.*, “Connexin-specific cell-to-cell transfer of short interfering RNA by gap junctions,” *J. Physiol.*, vol. 568, no. 2, pp. 459–468, 2005.

[35] H. Niessen, H. Harz, P. Bedner, K. Krämer, and K. Willecke, “Selective permeability of different connexin channels to the second messenger inositol 1,4,5-trisphosphate.,” *J. Cell Sci.*, vol. 113 (Pt 8, no. 8, pp. 1365–72, Apr. 2000.

[36] D. Locke *et al.*, “Altered permeability and modulatory character of connexin channels during mammary gland development,” *Exp. Cell Res.*, vol. 298, no. 2, pp. 643–660, 2004.

[37] P. Bedner, H. Niessen, B. Odermatt, K. Willecke, and H. Harz, “A method to determine the relative cAMP permeability of connexin channels,” *Exp. Cell Res.*, vol. 291, no. 1, pp. 25–35, 2003.

[38] P. Bedner, H. Niessen, B. Odermatt, M. Kretz, K. Willecke, and H. Harz, “Selective permeability of different connexin channels to the second messenger cyclic AMP,” *J. Biol. Chem.*, vol. 281, no. 10, pp. 6673–6681, 2006.

[39] W. A. Ayad, D. Locke, I. V. Koreen, and A. L. Harris, “Heteromeric, but not homomeric, connexin channels are selectively permeable to inositol phosphates,” *J. Biol. Chem.*, vol. 281, no. 24, pp. 16727–16739, 2006.

[40] N. J. Severs *et al.*, “Immunocytochemical analysis of connexin expression in the healthy and diseased cardiovascular system.,” *Microsc. Res. Tech.*, vol. 52, no. 3, pp. 301–22, Feb. 2001.

[41] C. Vozzi, E. Dupont, S. R. Coppen, H.-I. Yeh, and N. J. Severs, “Chamber-related Differences in Connexin Expression in the Human Heart,” *J. Mol. Cell. Cardiol.*, vol. 31, no. 5, pp. 991–1003, 1999.

[42] M. J. A. van Kempen *et al.*, “Differential connexin distribution accommodates cardiac function in different species,” *Microsc. Res. Tech.*, vol. 31, no. 5, pp. 420–436, Aug. 1995.

[43] S. Elenes, A. D. Martínez, M. Delmar, E. C. Beyer, and A. P. Moreno, “Heterotypic docking of Cx43 and Cx45 connexons blocks fast voltage gating of Cx43,” *Biophys. J.*, vol. 81, no. 3, pp. 1406–1418, Sep. 2001.

[44] A. P. Moreno, V. Hayrapetyan, G. Zhong, A. D. Martínez, and E. C. Beyer, “Homomeric and Heteromeric Gap Junctions,” *Card. Electrophysiol. Fourth Ed.*, vol. 126, pp. 120–126, 2004.

[45] A. Mondal, D. A. Appadurai, N. W. Akoum, F. B. Sachse, and A. P. Moreno, “Computational simulations of asymmetric fluxes of large molecules through gap junction channel pores,” *J. Theor. Biol.*, vol. 412, no. June 2016, pp. 61–73, 2017.

[46] S. R. Robinson, E. C. Hampson, M. N. Munro, and D. I. Vaney, “Unidirectional coupling of gap junctions between neuroglia,” *Science*, vol. 262, no. 5136, pp. 1072–4, 1993.

[47] A. Finkelstein, “Gap junctions and intercellular communications,” *Science*, vol. 265, no. 5175, pp. 1017–1018, 1994.

[48] J. F. Ek-Vitorín and J. M. Burt, “Quantification of gap junction selectivity,” *Am. J. Physiol. Cell Physiol.*, vol. 289, no. 6, pp. C1535-46, 2005.

[49] J. F. Ek-Vitorín, T. J. King, N. S. Heyman, P. D. Lampe, and J. M. Burt, “Selectivity of connexin 43 channels is regulated through protein kinase C – dependent phosphorylation,” *Circ Res*, vol. 98, no. 12, pp. 1498–1505, 2006.

[50] N. S. Heyman and J. M. Burt, “Hindered diffusion through an aqueous pore describes invariant dye selectivity of Cx43 junctions,” *Biophys. J.*, vol. 94, no. 3, pp. 840–854, Feb. 2008.

[51] G. Kanaporis, P. R. Brink, and V. Valiunas, “Gap junction permeability : selectivity for anionic and cationic probes,” *Am. J. Physiol. Cell Physiol.*, vol. 300, no. 3, pp. C600-9, 2013.

[52] P. A. Weber, H. C. Chang, K. E. Spaeth, J. M. Nitsche, and B. J. Nicholson, “The permeability of gap junction channels to probes of different size is dependent on connexin composition and permeant-pore affinities,” *Biophys J*, vol. 87, no. 2, pp. 958–973, 2004.

[53] C. G. Bevans, M. Kordel, S. K. Rhee, and A. L. Harris, “Isoform composition of

connexin channels determines selectivity among second messengers and uncharged molecules," *J. Biol. Chem.*, vol. 273, no. 5, pp. 2808–2816, 1998.

[54] K. A. Yamada, J. G. Rogers, R. Sundset, T. H. Steinberg, and J. E. Saffitz, "Up-Regulation of Connexin45 in Heart Failure," *J. Cardiovasc. Electrophysiol.*, vol. 14, no. 11, pp. 1205–1212, 2003.

[55] G. Krenning, E. M. Zeisberg, and R. Kalluri, "The origin of fibroblasts and mechanism of cardiac fibrosis.," *J. Cell. Physiol.*, vol. 225, no. 3, pp. 631–7, Nov. 2010.

[56] G. Gaudesius, M. Miragoli, S. P. Thomas, and S. Rohr, "Coupling of cardiac electrical activity over extended distances by fibroblasts of cardiac origin.," *Circ. Res.*, vol. 93, no. 5, pp. 421–8, Sep. 2003.

[57] S. Rohr, "Myofibroblasts in diseased hearts: New players in cardiac arrhythmias?," *Hear. Rhythm*, vol. 6, no. 6, pp. 848–856, Jun. 2009.

4.10 Supplementary Data

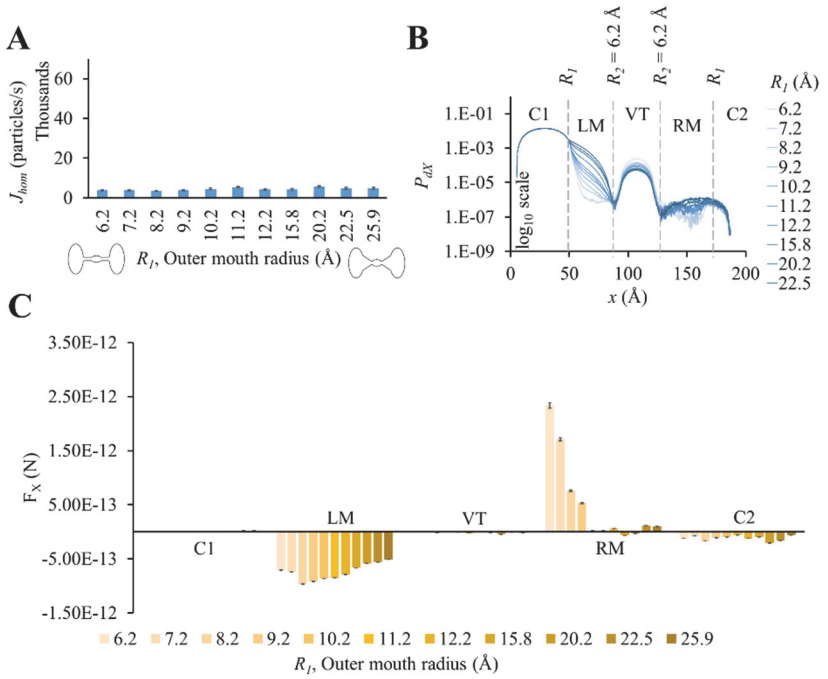

Figure 4.S1 – Properties of conical mouthed homotypic pores with narrow inner mouth (R_1-6.2-6.2- R_1). Flux simulation results (n = 30) from homotypic pores with varying outer mouth radius of R_1 = 6.2 to 25.9 Å and fixed inner mouth radius of R_2 = 6.2 Å. (A) LY fluxes varied marginally in pores with the narrow inner mouth. (B) Particle probabilities were in the same order of magnitude in cell 1 and the vestibule, but had distinct variations in the left and right mouths. (C) F_X in left and right mouths are in opposite directions and highest magnitudes in the pore. F_X magnitude rose and then declined in the left mouth. F_X dropped asymptotically in the right mouth as outer mouth size was increased.

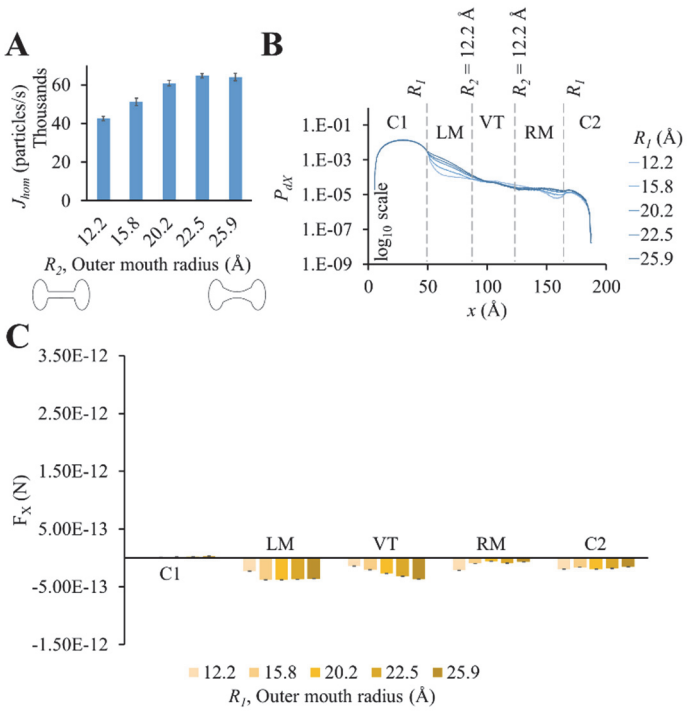

Figure 4.S2 – Properties of conical mouthed homotypic pores with wide inner mouth (R_1-12.2-12.2- R_1). Results from flux simulations (n = 30) in homotypic pores with varying outer mouth radius of R_1 = 12.2 to 25.9 Å with constant inner mouth radius of R_2 = 12.2 Å. (A) LY fluxes rose more distinctly in wide inner mouth pores and saturate after R_1 = 22.5 Å. (B) Variation in P_{dX} across the pore was low with almost linear change (log 10 scale) for R_1 = 25.9 Å. Variations were most significant in the left and right mouths. (C) F_X was in -x direction in all sections with pronounced magnitudes from left mouth to cell 2. F_X magnitude increased linearly in the vestibule with increasing outer mouth size.

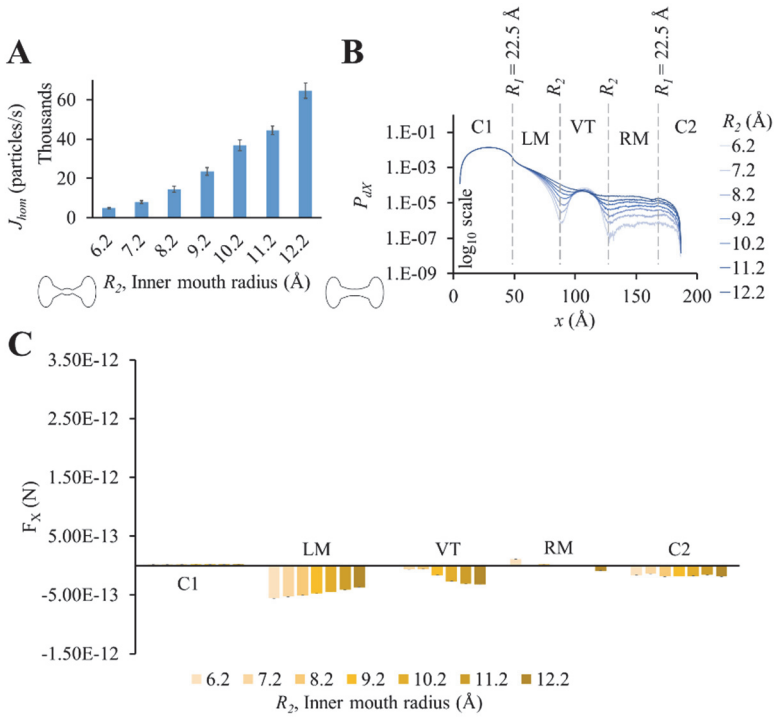

Figure 4.S3 – Properties of conical mouthed homotypic pores with fixed outer mouth and varying inner mouth size (22.5-R_2-R_2-22.5). Results from flux simulations (n = 30) in homotypic pores with fixed outer mouth radius of R_1 = 22.5 Å and varying inner mouth radius of R_2 = 6.2 Å to 12.2 Å. (A) LY flux rose nonlinearly with increase in inner mouth size. (B) P_{dX} variations began inside the left mouth (closer to the inner mouth), while remaining in the same order in the vestibule. (C) F_X was negative in the pore and magnitudes were pronounced in the left mouth and vestibule. While F_X magnitude decreased in the left mouth, it increased in the vestibule with increasing R_2.

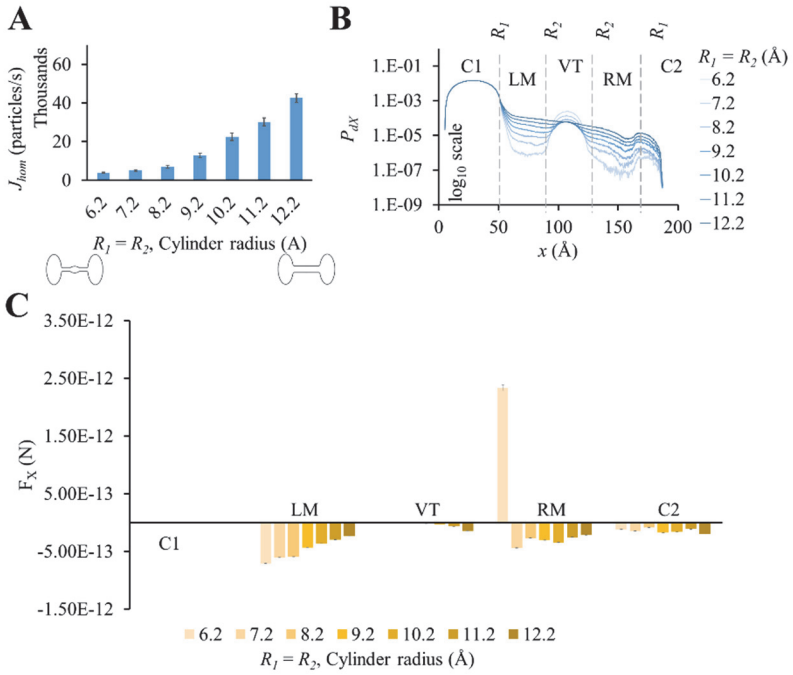

Figure 4.S4 – Properties of cylindrical mouthed homotypic pores with varying cylinder size (R_1-R_2-R_2-R_1). Results from flux simulations (n = 30) in homotypic pores with varying cylinder radius of $R_1 = R_2$ = 6.2 Å to 12.2 Å. (A) LY flux rose nonlinearly with increase in inner mouth size. (B) P_{dX} in cell 1 and vestibule were in the same order in all cases with almost parallel lines in the left and right mouths. (C) F_X magnitudes in left and right mouth were most distinct with a steady decrease in the left mouth with increasing cylinder mouth size. F_X was in the -x direction in all cases except in the right mouth for $R_1 = R_2$ = 6.2 Å.

Table 4.S1: LY fluxes in homotypic pores.

S#	Sectional radius (Å)		J_{hom} (particles/s)	S#	Sectional radius (Å)		J_{hom} (particles/s)
	R_1	R_2			R_1	R_2	
1	6.2	6.2	3804.9	29	15.8	6.2	4258.9
2	7.2	6.2	3824.3	30	15.8	7.2	7844.4
3	7.2	7.2	5057.0	31	15.8	8.2	11515.7
4	8.2	6.2	3551.7	32	15.8	9.2	21638.1
5	8.2	7.2	4687.2	33	15.8	10.2	34082.5
6	8.2	8.2	6985.9	34	15.8	11.2	40012.9
7	9.2	6.2	3849.5	35	15.8	12.2	51116.4
8	9.2	7.2	5555.1	36	20.2	6.2	5663.9
9	9.2	8.2	8856.2	37	20.2	7.2	8331.9
10	9.2	9.2	12883.2	38	20.2	8.2	16001.4
11	10.2	6.2	4504.7	39	20.2	9.2	23334.7
12	10.2	7.2	5805.3	40	20.2	10.2	32612.0
13	10.2	8.2	9901.2	41	20.2	11.2	43797.4
14	10.2	9.2	16086.6	42	20.2	12.2	60807.5
15	10.2	10.2	22533.8	43	22.5	6.2	4855.0
16	11.2	6.2	5384.2	44	22.5	7.2	7922.1
17	11.2	7.2	6278.8	45	22.5	8.2	14498.6
18	11.2	8.2	9790.2	46	22.5	9.2	23587.6
19	11.2	9.2	17205.4	47	22.5	10.2	36827.1
20	11.2	10.2	20166.8	48	22.5	11.2	44521.2
21	11.2	11.2	30187.0	49	22.5	12.2	64587.9
22	12.2	6.2	4253.1	50	25.9	6.2	4786.9
23	12.2	7.2	5639.5	51	25.9	7.2	9931.0
24	12.2	8.2	13204.9	52	25.9	8.2	14376.1
25	12.2	9.2	14817.5	53	25.9	9.2	25824.3
26	12.2	10.2	22680.4	54	25.9	10.2	39608.0
27	12.2	11.2	29211.8	55	25.9	11.2	44153.7
28	12.2	12.2	42541.6	56	25.9	12.2	64099.7

Table 4.S2: LY fluxes and flux ratios in heterotypic pores.

S#	Sectional radius (Å)				$J_{het,1}$ (particles/s)	$J_{het,2}$ (particles/s)	α_{het}	α_{hom}
	R_1	R_2	R_3	R_4				
1	9.2	9.2	9.2	9.2	12890.0	11226.0	1.15	1.00
2	10.2	9.2	9.2	9.2	14061.5	11758.5	1.20	1.25
3	11.2	9.2	9.2	9.2	12562.1	14321.9	0.88	1.34
4	12.2	9.2	9.2	9.2	12751.4	15574.8	0.82	1.15
5	15.8	9.2	9.2	9.2	12790.6	14150.4	0.90	1.68
6	20.2	9.2	9.2	9.2	13060.6	16887.7	0.77	1.81
7	22.5	9.2	9.2	9.2	12842.7	19558.6	0.66	1.83
8	25.9	9.2	9.2	9.2	11341.5	18291.3	0.62	2.00
9	22.5	6.2	9.2	9.2	6303.1	6403.4	0.98	0.38
10	22.5	7.2	9.2	9.2	8624.0	11788.3	0.73	0.61
11	22.5	8.2	9.2	9.2	12401.2	15425.2	0.80	1.13
12	22.5	9.2	9.2	9.2	12842.7	19558.6	0.66	1.83
13	22.5	10.2	9.2	9.2	12813.0	17344.1	0.74	2.86
14	22.5	11.2	9.2	9.2	14403.2	22928.2	0.63	3.46
15	22.5	12.2	9.2	9.2	16953.2	22642.5	0.75	5.01
16	22.5	9.2	6.2	6.2	4055.5	4496.8	0.90	6.20
17	22.5	9.2	7.2	7.2	4214.6	6336.0	0.67	4.66
18	22.5	9.2	8.2	8.2	7367.6	13462.8	0.55	3.38
19	22.5	9.2	9.2	9.2	12842.7	19558.6	0.66	1.83
20	22.5	9.2	10.2	10.2	19699.0	22328.9	0.88	1.05
21	22.5	9.2	11.2	11.2	27838.7	30456.4	0.91	0.78
22	22.5	9.2	12.2	12.2	29762.5	34039.7	0.87	0.55
23	25.9	12.2	6.2	6.2	2919.7	4040.3	0.72	16.85
24	25.9	12.2	7.2	7.2	4362.8	6668.5	0.65	12.68
25	25.9	12.2	8.2	8.2	6368.0	12894.2	0.49	9.18
26	25.9	12.2	9.2	9.2	12695.9	23360.8	0.54	4.98
27	25.9	12.2	10.2	10.2	23490.3	31756.7	0.74	2.84
28	25.9	12.2	11.2	11.2	35491.6	44288.8	0.80	2.12
29	25.9	12.2	12.2	12.2	41922.6	51409.3	0.82	1.51

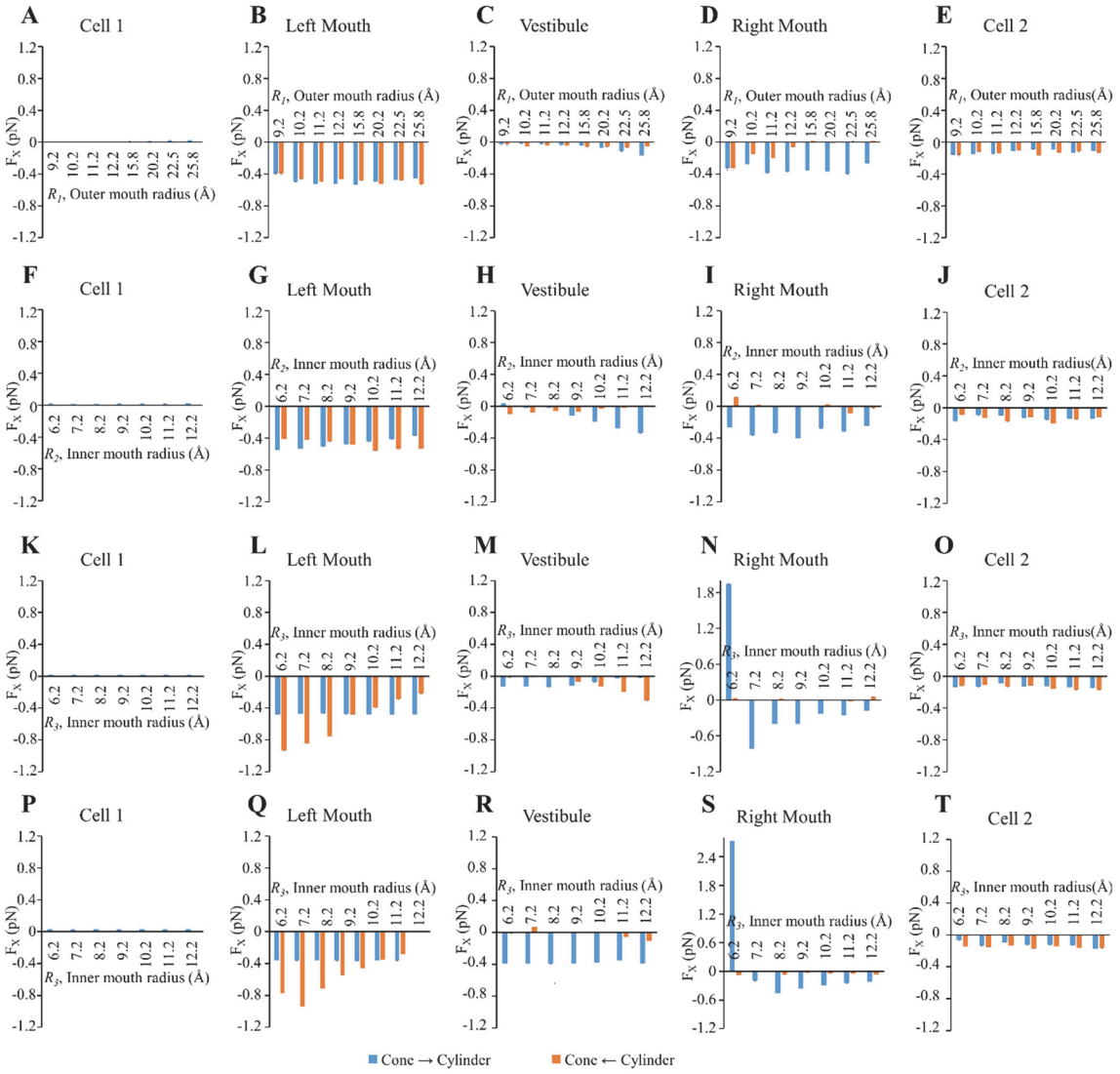

Figure 4.S5 – Average force per LY particle per section in heterotypic pores. F_X values in all pore sections in heterotypic pores of profiles (A-E) R_1-9.2-9.2-9.2 (F-J) 22.5-R_2-9.2-9.2 (K-O) 22.5-9.2-R_3-R_3 and (P-T) 25.9-12.2-R_3-R_3.

CHAPTER 5

SUMMARY, CONCLUSIONS AND FUTURE WORK

5.1 Summary and conclusions

In this research, engineering approaches were applied to develop new *in vitro* and *in silico* tools for studying heterotypic gap junction properties. The research was carried out in three parts as described in Chapters 2 to 4.

In Chapter 2, we utilized microfabrication technology to generate a new device called PerFlexMEA that enabled electrophysiological studies on neonatal myocytes as we controlled intercellular coupling between the myocyte and nonmyocyte monolayers. We confirmed controlled intercellular coupling between the two cell layers while maintaining tissue architecture through dye diffusion experiments and confocal imaging of cellular preparations. We further demonstrated the slowing of conduction velocity in the myocyte layer as lateral coupling with nonmyocytes was established. We also reported cell migration issues with fibroblasts and how we selected HeLaCx43 cells instead to demonstrate the functionality of our novel device. Our results indicate PerFlexMEA as a potential tool for creating fibrotic tissues with controlled lateral coupling and serving as a platform for testing drugs and other cellular approaches for treating fibrotic heart tissue.

In Chapter 3, we presented a simplified Brownian dynamics model of a gap junction pore. We used this model to simulate interaction of Lucifer yellow molecules during steady

state experiments and under concertation gradient experiments. Flux asymmetry results from our *in silico* and *in vitro* results matched significantly with our hypothesized heterotypic pore shape. Our simulation yielded fluxes within the order of magnitude of those recorded from *in vitro* experiments. Our simulation results have revealed that a heterotypic inactive pore is capable of creating active pore-like mechanisms through redistribution of charged particles to produce asymmetric fluxes. Such heterotypic pores can have physiological consequences in healthy and diseased tissues by maintaining different concentrations of large ionic molecules among coupled cells. This needs to be investigated further *in vivo*. Furthermore, based on the revealed mechanism, artificial porous membranes with pore size and shape mimicking the heterotypic gap junction pores can be fabricated for potential filtration and dialysis applications. Chambers separated by such membranes would allow maintaining different concentrations of selected large ions in adjacent chambers.

In Chapter 4, we utilized the model presented in Chapter 3 to identify a relationship between flux asymmetry and different pore section sizes, the particle size and charge. Key pore features that regulated flux asymmetry were identified. Flux asymmetry was found to exist independent of particle size with an upper limit that depended on the minimum size of the pore's mouth. Particle charge's role was found to primarily scale flux asymmetry, but asymmetric pore shape was found to be the key parameter governing flux asymmetry. Furthermore, an optimum pore shape was identified that closely matched the flux asymmetry data from our *in vitro* experiments from Chapter 3. We also discussed the possible role of such heterotypic pores in diseased heart tissue, where probability of heterotypic gap junction formation is higher than in healthy tissue. Our simulation results

reinforced our original hypothesis stated in Chapter 3 and indicate that asymmetry in pore-shape of heterotypic gap junction channels plays the primary role in producing asymmetric fluxes of large charged molecules.

5.2 Future work

The PerFlexMEA was the first step towards a broader goal of creating an accurate and reproducible *in vitro* fibrotic cardiac tissue model for electrophysiological studies. We have demonstrated its capability of controlling myocyte-nonmyocyte lateral coupling in heterocellular cultures. The next step would be to co-culture with cells that express Cx45 hemichannels, preferably with fibroblast/myofibroblasts cultures. The key would be to reduce the pore diameter < 1 μm in the parylene substrate. The allowable pore size will need to be optimized to stop or minimize fibroblast migration across the porous parylene membrane while still forming functional gap junction with myocytes. Reactive ion etching (RIE) and deep reactive ion etching (DRIE) process will have to be investigated to make up for the increase in aspect ratio of the pore. The other option would be to reduce membrane thickness. Tissue heterogeneity can be reduced by creating anisotropic myocyte cultures. This can be accomplished by patterning (lithography and RIE) micro-channels on the substrate [1], [2] or by printing molecular substrates through soft-lithography [3], [4]. Such anisotropic cultures will also improve controlling nonmyocyte per myocyte coupling ratio through membrane porosity. This would aid in validating conduction effects of myocyte-nonmyocyte lateral coupling predicted in *in silico* models [5], [6]. Furthermore, tissues in other coupling-configurations [7] can also be created. In particular, effects of intercalated myocyte-nonmyocyte coupling needs to be compared with those in laterally

coupled configuration. The PerFlexMEA can serve as a reliable platform for testing the effects of potential drugs in fibrotic tissues. Antiarrhythmic peptides (AAPs) [8] like Rotigaptide [9] that promote Cx expression in fibrotic tissues can be tested to investigate its possible arrhythmic role through enhanced myocyte-nonmyocyte coupling. Drugs targeting ion channels can also be tested. Since fibroblast too express ion channels [10], sodium channel targeting drugs like Lidocaine [11], [12] that are aimed at myocytes can have additional side-effects due to functional changes in fibroblasts. The PerFlexMEA is also an excellent platform for studying the effectiveness of fibroblast reprogramming approaches [13]–[16]. Comparative conduction studies between myocyte-myocyte and myocyte-reprogrammed-nonmyocyte bilayers would help quantify conduction changes in such approaches.

For the simulation experiments, updating the statistical limits of our Brownian simulation gap junction model would be the first step in expanding the range of particle charge and size of our model. This would help draw a direct correlation for molecules with large charge and size like ATP, IP_3 and other nucleotides for which *in vitro* data are present for only homotypic junctions [17]–[25]. Particle shape will play a greater role in particle-pore interaction for larger and longer molecules like mRNA. Particle orientation will need to be implemented in the model for studies with such molecules. Through our simulation results, we made a strong case for a potential mechanism explaining *in vitro* experimental results. Reproduction of our results in existing molecular dynamics software [26], [27] would further validate the identified mechanism. Further *in vitro* studies need to be designed to verify directly the mechanism predicted by our simulation results and investigate the speculated physiological implications. Our focus so far had been on pore

shape and particle size and charge. The gap junction pore's charge residues can play a very significant role in selective permeability mechanisms [28]. A lack of structural details is a major hurdle towards accurately predicting the role of such residual pore surface charges. Perhaps approaches can be taken by placing charged rings at the inner and outer mouths of the hemichannels as implemented for in molecular dynamics modeling of Cx26 channel [29]. Combinations of positive, negative and neutral charged rings placed in the two inner and two outer pore mouths could reveal new mechanisms for flux asymmetry.

The key to making breakthrough in understanding the structure-function details of gap junctions is in their channel structures. Accurate structural knowledge will enable creating models for understanding the capability of homotypic and heterotypic channels from junctional to tissue level.

5.3 References

[1] S. Rohr, D. M. Scholly, and a. G. Kleber, "Patterned growth of neonatal rat heart cells in culture. Morphological and electrophysiological characterization," *Circ. Res.*, vol. 68, no. 1, pp. 114–130, Jan. 1991.

[2] D. Motlagh, T. J. Hartman, T. a Desai, and B. Russell, "Microfabricated grooves recapitulate neonatal myocyte connexin43 and N-cadherin expression and localization.," *J. Biomed. Mater. Res. A*, vol. 67, no. 1, pp. 148–57, Oct. 2003.

[3] E. Ostuni, R. Kane, C. Chen, and D. Ingber, "Patterning mammalian cells using elastomeric membranes," *Langmuir*, vol. 16, no. 20, pp. 7811–7819, 2000.

[4] H. Kaji, G. Camci-Unal, R. Langer, and A. Khademhosseini, "Engineering systems for the generation of patterned co-cultures for controlling cell-cell interactions.," *Biochim. Biophys. Acta*, vol. 1810, no. 3, pp. 239–50, Mar. 2011.

[5] F. B. Sachse, A. P. Moreno, G. Seemann, and J. A. Abildskov, "A model of electrical conduction in cardiac tissue including fibroblasts.," *Ann. Biomed. Eng.*, vol. 37, no. 5, pp. 874–89, May 2009.

[6] Y. Xie, A. Garfinkel, P. Camelliti, P. Kohl, J. Weiss, and Z. Qu, "Effects of fibroblast-myocyte coupling on cardiac conduction and vulnerability to reentry: a

computational study," *Hear. Rhythm*, vol. 6, no. 11, pp. 1641–1649, 2009.

[7] P. Kohl and P. Camelliti, "Cardiac myocyte-nonmyocyte electrotonic coupling: implications for ventricular arrhythmogenesis.," *Heart Rhythm*, vol. 4, no. 2, pp. 233–5, Feb. 2007.

[8] S. Dhein and T. Tudyka, "Therapeutic potential of antiarrhythmic peptides. Cellular coupling as a new antiarrhythmic target.," *Drugs*, vol. 49, no. 6, pp. 851–5, Jun. 1995.

[9] T. C. Clarke, D. Thomas, J. S. Petersen, W. H. Evans, and P. E. M. Martin, "The antiarrhythmic peptide rotigaptide (ZP123) increases gap junction intercellular communication in cardiac myocytes and HeLa cells expressing connexin 43.," *Br. J. Pharmacol.*, vol. 147, no. 5, pp. 486–95, Mar. 2006.

[10] G.-R. Li, H.-Y. Sun, J.-B. Chen, Y. Zhou, H.-F. Tse, and C.-P. Lau, "Characterization of multiple ion channels in cultured human cardiac fibroblasts.," *PLoS One*, vol. 4, no. 10, p. e7307, Jan. 2009.

[11] S. Goineau, V. Castagné, P. Guillaume, and G. Froget, "The comparative sensitivity of three in vitro safety pharmacology models for the detection of lidocaine-induced cardiac effects.," *J. Pharmacol. Toxicol. Methods*, vol. 66, no. 1, pp. 52–8, Jul. 2012.

[12] J. X. Kang and a Leaf, "Effects of long-chain polyunsaturated fatty acids on the contraction of neonatal rat cardiac myocytes.," *Proc. Natl. Acad. Sci. U. S. A.*, vol. 91, no. 21, pp. 9886–90, Oct. 1994.

[13] L. Qian *et al.*, "In vivo reprogramming of murine cardiac fibroblasts into induced cardiomyocytes," *Nature*, vol. 485, no. 7400, pp. 593–598, Apr. 2012.

[14] T. M. Jayawardena *et al.*, "MicroRNA-Mediated In Vitro and In Vivo Direct Reprogramming of Cardiac Fibroblasts to Cardiomyocytes," *Circ. Res.*, vol. 110, no. 11, pp. 1465–1473, 2012.

[15] K. Song *et al.*, "Heart repair by reprogramming non-myocytes with cardiac transcription factors.," *Nature*, vol. 485, no. 7400, pp. 599–604, May 2012.

[16] T. Sadahiro, S. Yamanaka, and M. Ieda, "Direct Cardiac Reprogramming," *Circ Res*, vol. 116, no. 7, pp. 1378–1391, 2015.

[17] W. A. Ayad, D. Locke, I. V. Koreen, and A. L. Harris, "Heteromeric, but not homomeric, connexin channels are selectively permeable to inositol phosphates," *J. Biol. Chem.*, vol. 281, no. 24, pp. 16727–16739, 2006.

[18] P. Bedner, H. Niessen, B. Odermatt, M. Kretz, K. Willecke, and H. Harz, "Selective permeability of different connexin channels to the second messenger cyclic AMP," *J. Biol. Chem.*, vol. 281, no. 10, pp. 6673–6681, 2006.

[19] P. Bedner, H. Niessen, B. Odermatt, K. Willecke, and H. Harz, “A method to determine the relative cAMP permeability of connexin channels,” *Exp. Cell Res.*, vol. 291, no. 1, pp. 25–35, 2003.

[20] G. S. Goldberg, P. D. Lampe, and B. J. Nicholson, “Selective transfer of endogenous metabolites through gap junctions composed of different connexins.,” *Nat. Cell Biol.*, vol. 1, no. 7, pp. 457–459, 1999.

[21] G. S. Goldberg, A. P. Moreno, and P. D. Lampe, “Gap junctions between cells expressing connexin 43 or 32 show inverse permselectivity to adenosine and ATP.,” *J. Biol. Chem.*, vol. 277, no. 39, pp. 36725–30, Sep. 2002.

[22] A. L. Harris, “Connexin channel permeability to cytoplasmic molecules,” *Prog. Biophys. Mol. Biol.*, vol. 94, no. 1–2, pp. 120–143, 2007.

[23] D. Locke *et al.*, “Altered permeability and modulatory character of connexin channels during mammary gland development,” *Exp. Cell Res.*, vol. 298, no. 2, pp. 643–660, 2004.

[24] H. Niessen, H. Harz, P. Bedner, K. Krämer, and K. Willecke, “Selective permeability of different connexin channels to the second messenger inositol 1,4,5-trisphosphate.,” *J. Cell Sci.*, vol. 113 (Pt 8, no. 8, pp. 1365–72, Apr. 2000.

[25] V. Valiunas *et al.*, “Connexin-specific cell-to-cell transfer of short interfering RNA by gap junctions,” *J. Physiol.*, vol. 568, no. 2, pp. 459–468, 2005.

[26] J. C. Phillips *et al.*, “Scalable molecular dynamics with NAMD,” *J. Comput. Chem.*, vol. 26, no. 16, pp. 1781–1802, 2005.

[27] W. Humphrey, A. Dalke, and K. Schulten, “VMD: Visual Molecular Dynamics,” *J. Mol. Graph.*, vol. 14, no. 1, pp. 33–38, 1996.

[28] X. Lin, Q. Xu, and R. D. Veenstra, “Functional formation of heterotypic gap junction channels by connexins-40 and -43,” *Channels*, vol. 8, no. 5, pp. 433–443, 2014.

[29] Y. Escalona, J. A. Garate, R. Araya-Secchi, T. Huynh, R. Zhou, and T. Perez-Acle, “Exploring the Membrane Potential of Simple Dual-Membrane Systems as Models for Gap-Junction Channels,” *Biophys. J.*, vol. 110, no. 12, pp. 2678–2688, 2016.